Current-induced Magnetization Switching by a generated Spin-Orbit Torque in the 3D Topological Insulator Material HgTe

Dissertation zur Erlangung des naturwissenschaftlichen Doktorgrades der Julius-Maximilians-Universität Würzburg

vorgelegt von

Konstantin Martin

aus Koktschetaw/Kasachstan

Würzburg, 2021

Eingereicht am: 25.11.2020
bei der Fakultät für Physik und Astronomie

1. Gutachter: Prof. Dr. Charles Gould
2. Gutachter: Prof. Dr. Friedrich Reinert
3. Gutachter: .....
der Dissertation

Vorsitzende(r): Prof. Dr. Peter Jakob
1. Prüfer: Prof. Dr. Charles Gould
2. Prüfer: Prof. Dr. Friedrich Reinert
3. Prüfer: Prof. Dr. Giorgio Sangiovanni
im Promotionskolloquium

Tag des Promotionskolloquiums: 18.06.2021

Doktorurkunde ausgehändigt am: .....

For my loving and beautiful wife Emma
who is always supporting me.
Thank you for spending your life with me.

Contents

1

Introduction

In 1968 semiconductor technology was utilized to build the first dynamic random access memory (DRAM) that was compatible with electronics set on integrated chips [1]. Since then the market for RAM is dominated by this cheap and scalable technology which is reaching its physical limits that lie in the order of 10 nm [2]. This trend leads to higher standby power resulting in an overall bottleneck for standard logic systems. Non-volatile technologies, like magnetic RAM (MRAM), show great potential to reduce power consumption by exploiting the spin property of electrons. A magnetic tunnel junction (MTJ), which consists of two ferromagnets (FM), a free layer and a reference layer, separated by a thin oxide, form the basic element of MRAM [3]. The MTJ exhibits two distinct states, parallel and anti-parallel, which can be efficiently switched by a charge current utilizing a promising mechanism called spin transfer torque (STT) [4]. Due to their high efficiency and downscaling feasibility STT-MRAM appear to be the most promising candidates to replace standard memory systems [5].

In a STT geometry electrons have to pass all layers starting with the reference layer where their spin is oriented in order to transfer the spin angular momentum, just a single time, when traveling through the recording layer [6]. Moreover the writing path is also used as the reading path. As the writing current has to be higher than the reading current in order to induce a change, too high currents could damage the tunnel barrier in a MTJ and result in high power consumption as well as reliability issues. These problems get resolved by another famous switching mechanism known as spin orbit torque (SOT). This effect stems from the conversion of a charge current to spin according to spin Hall effect (SHE) and inverse spin galvanic effect (iSGE) [7]. Here the writing mechanism consists of generating a small amount of spin polarization each time an electron gets scattered. Subsequently a small amount of torque gets transfered to the adjacent free layer leading to switching at corresponding current directions and values. Two terminal SOT-MRAM configurations already proved to use 70% less critical current than STT-MRAM devices [8]. Furthermore such SOT driven devices offer high endurance as well as magnetization switching

times in the sub-nanosecond regime [9]. Due to its high spin orbit coupling (SOC) property, heavy metals like Pt or Ta were utilized as the current channel in early SOT experiments [10–12]. In general the measured SOT depends highly on the SOC capabilities of the used material system. Thus it is not surprising that topological insulators (TIs), which exhibit high SOC and therefore high current-to-spin conversion rates, are regarded as an optimal material system for SOT studies [7, 13]. Among all existing TIs it is HgTe that can be reliably grown as an insulator. Together with its band inversion and resulting topological surface states HgTe can be regarded as the prototype topological insulator.

The aim of this work is to investigate the SOT efficiencies generated by a current on the surface of the three dimensional material system HgTe. In order to achieve this a device has to be build where the effect of a current induced torque can be measured. A specific layer stack consisting of two in sample plane oriented ferromagnets offers two states, parallel and anti-parallel, that result in two distinct measurable resistances. This layer stack has to be properly separated from the TI to avoid electric transport through the stack which alters the measurability of the SOT. Consequently there are two important steps that have to be carried out before building the final device. Firstly a tunnel barrier on top of the TI has to be established, which is thin enough to exploit the SOT and, at the same time, thick enough to exhibit high vertical resistance so that electrons from the TI cannot pass easily to the ferromagnet. Secondly a ferromagnetic layer stack has to be established that is able to exhibit two distinct resistance states. For this a hard and soft magnetic layer have to be chosen, optimized and finally shaped into $600 \times 200\,\mathrm{nm}^2$ pillars to view the average sensor behavior. As will be shown later the performance of such a layer stack differs significantly when it gets deposited on a TI.

In order to address all mentioned points in a sensible sequence the thesis is divided into five further chapters. We first start with an introduction of the material system. Here it describes how CdTe /HgTe /CdTe heterostructures form topological surface states which exhibit a linear dispersion relation and a perpendicular relation between momentum and spin of the surface state electrons. Consequently the application of a current at a certain direction will lead to a perpendicular and in sample plane spin accumulation. In chapter 3 the development of the tunnel barrier is discussed. The theoretical background serves as a guideline how working tunnel barriers behave. After some remarks on device fabrication the experimental results are shown for confirmation of proper tunneling behavior. Aside from this some samples have been tested for thermopower measurements. Chapter 4 addresses the difficulties of developing a working layer stack. In the case of HgTe it appears that the favored magnetic direction cannot be easily biased by a fixed external field. FMR and SQUID measurements had to be deployed in order to gain knowledge about the behaviour of sputtered layer stacks on big area ($3 \times 3\,\mathrm{mm}^2$) and pillar sized ($600 \times 200\,\mathrm{nm}^2$) samples. Chapter 5 deals with the production of the final device and the investigation on its intrinsic properties. With the description of the measurement procedures and the expected behavior all experimental results are sensibly discussed. These contain the measured giant magnetoresistance of a nano pillar, current induced switching of the adjacent

magnetization and finally the extraction of efficiencies accompanied with their comparison to other material systems. It will be shown that the final device on hand exhibits the highest efficiencies of switching in plane magnetized anisotropies ever recorded. Finally all results are summarized at the last chapter.

1

References

[1] S. Bhatti, R. Sbiaa, A. Hirohata, H. Ohno, S. Fukami, and S. Piramanayagam, *Spintronics based random access memory: a review,* Materials Today **20**, 530 (2017).

[2] S.-K. Park, *Technology scaling challenge and future prospects of dram and nand flash memory,* in *2015 IEEE International Memory Workshop (IMW)* (IEEE, 2015) pp. 1–4.

[3] E. Deng, Y. Zhang, J.-O. Klein, D. Ravelsona, C. Chappert, and W. Zhao, *Low power magnetic full-adder based on spin transfer torque mram,* IEEE transactions on magnetics **49**, 4982 (2013).

[4] J. C. Slonczewski *et al.*, *Current-driven excitation of magnetic multilayers,* Journal of Magnetism and Magnetic Materials **159**, L1 (1996).

[5] W. Kim, J. Jeong, Y. Kim, W. Lim, J. Kim, J. Park, H. Shin, Y. Park, K. Kim, S. Park, *et al.*, *Extended scalability of perpendicular stt-mram towards sub-20nm mtj node,* in *2011 International Electron Devices Meeting* (IEEE, 2011) pp. 24–1.

[6] J. Sinova and T. Jungwirth, *Surprises from the spin hall effect,* Physics Today **70**, 38 (2017).

[7] A. Manchon, J. Železnỳ, I. M. Miron, T. Jungwirth, J. Sinova, A. Thiaville, K. Garello, and P. Gambardella, *Current-induced spin-orbit torques in ferromagnetic and antiferromagnetic systems,* Reviews of Modern Physics **91**, 035004 (2019).

[8] N. Sato, F. Xue, R. M. White, C. Bi, and S. X. Wang, *Two-terminal spin–orbit torque magnetoresistive random access memory,* Nature Electronics **1**, 508 (2018).

[9] K. Garello, C. O. Avci, I. M. Miron, M. Baumgartner, A. Ghosh, S. Auffret, O. Boulle, G. Gaudin, and P. Gambardella, *Ultrafast magnetization switching by spin-orbit torques,* Applied Physics Letters **105**, 212402 (2014).

[10] K. Garello, I. M. Miron, C. O. Avci, F. Freimuth, Y. Mokrousov, S. Blügel, S. Auffret, O. Boulle, G. Gaudin, and P. Gambardella, *Symmetry and magnitude of spin–orbit torques in ferromagnetic heterostructures,* Nature nanotechnology **8**, 587 (2013).

[11] S. Emori, U. Bauer, S.-M. Ahn, E. Martinez, and G. S. Beach, *Current-driven dynamics of chiral ferromagnetic domain walls,* Nature materials **12**, 611 (2013).

[12] L. Liu, C.-F. Pai, Y. Li, H. Tseng, D. Ralph, and R. Buhrman, *Spin-torque switching with the giant spin hall effect of tantalum,* Science **336**, 555 (2012).

[13] W. Han, Y. Otani, and S. Maekawa, *Quantum materials for spin and charge conversion,* npj Quantum Materials **3**, 1 (2018).

2

3D HgTe as the Material under Investigation

A Topological insulator (TI) is a state of quantum matter which differs from classical insulators, conductors or semiconductors. In contrast to the latter states TIs are insulating in their bulk while their interfaces with different materials (even vacuum) are conducting [1]. There are many material systems that are classified as a TI, e.g. Bi_2Se_3 , $Bi_{0.9}Sb_{0.1}$ or HgTe. This thesis focuses on the 3D TI material system HgTe which is incorporated into a CdTe /$Cd_{0.68}Hg_{0.32}$Te /HgTe /$Cd_{0.68}Hg_{0.32}$Te heterostructure.

The following chapter aims to give an overview of HgTe properties. It begins with the description of its band structure followed by its behavior in a CdTe /HgTe /CdTe heterostructure. Beside the derivation of the typical cone-like dispersion relation the final sections address the mechanism of spin accumulation through a current on the interfaces of the heterostructure. This effect forms the base for the main investigations on SOT in our material system.

2.1. Band Structure and material Properties

2

In a periodic lattice electron states are classified in terms of their crystal momentum $\vec{k}$. Those states obey the physics given by the Bloch Hamiltonian H. They are described by the Bloch states $u_m\left(\vec{k}\right)$ which are defined in a unit cell of the crystal for the m-th band. Mathematically the Bloch states are eigenstates of H which allow, according to the Schrödinger equation $H\Psi = E\Psi$, the derivation of the eigenvalues $E_m\left(\vec{k}\right)$. Those eigenvalues define the energy of the m-th band. All bands together form the band structure of the crystal. In order to calculate the band structure of HgTe in Figure 2.1 the empirical pseudo potential method was used [2]. Within that method only the valence electrons are considered resulting in a weak periodic potential of the lattice. Additional expansion of the wave functions Ψ leads to further simplifications in solving the Schrödinger equation [3].

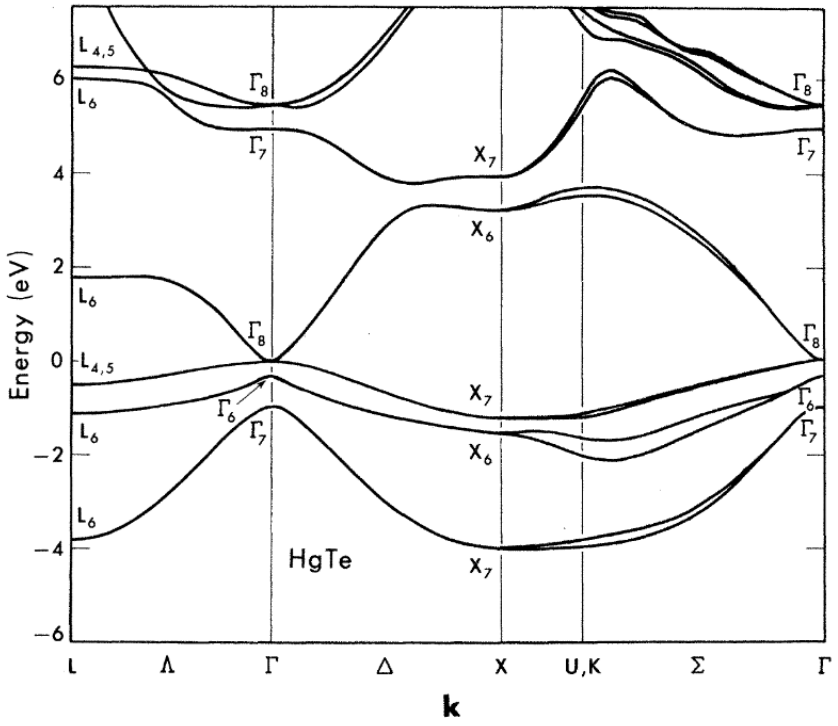

Figure 2.1: Calculated band structure of intrinsic HgTe. The Γ_6 band lies below the Γ_8 which is double degenerate resulting in HgTe being a semimetal. Picture taken from [2]

The band structure is represented in energies at specific values of $\vec{k}$. The $\vec{k} = 0$ value Γ is known as the point of highest symmetry. The electronic states in Γ_6 are of s-type with a total angular momentum of $j = 1/2$ while electronic states in Γ_8 are of p-type with $j = 3/2$. As the band gap is defined by the difference $\Delta E = E(\Gamma_6) - E(\Gamma_8)$, HgTe exhibits a negative band gap of $\Delta E = -0.3\,\mathrm{eV}$ at $T = 0\,\mathrm{K}$. The reason for this inversion stems from relativistic corrections of the Hamiltonian due to the heavy Hg atoms [4]. In this case the light hole band of Γ_8 acts as the

conduction band while the heavy hole band of Γ_8 forms the valence band. As a result the band gap in unstrained HgTe, where Γ_8 is double degenerate, does not exist leaving intrinsic HgTe as a semi metal. By growing HgTe on CdTe it is possible to introduce strain to the HgTe crystal [5, 6]. This leads to lifting of the degeneracy of the Γ_8 bands with a band gap of $\Delta E = 22\,\text{meV}$ [7]. The inversion of the Γ_8 and Γ_6 band together with a strain induced band gap are the key elements that make HgTe a topological insulator.

2.2. CdTe/HgTe Heterostructures

2.2.1. The topological Surface State

As soon as two different materials come into contact they form a heterostructure. During this process bands of the same symmetry form a continuous connection. This thesis focuses on $Cd_{0.68}Hg_{0.32}Te$ /HgTe /$Cd_{0.68}Hg_{0.32}Te$ layer systems which are conceptually similar to CdTe /HgTe /CdTe layer systems schematically shown in Fig. 2.2 [8].

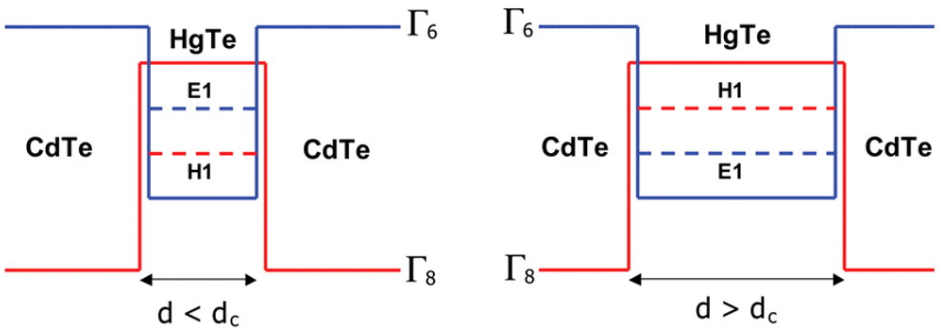

Figure 2.2: Schematic picture of CdTe /HgTe /CdTe layer system for two different thicknesses. E_1 and H_1 are the lowest subbands for the Γ_6 and Γ_8 band respectively. Picture is taken from [8].

Here E_1 and H_1 are the lowest sub bands for the Γ_6 and Γ_8 band respectively. It can be seen that for HgTe thicknesses below a critical thickness d_c the band structure in the well is not inverted. As a result the layer system behaves as a trivial insulator. By increasing the thickness above d_c the sub band E_1 goes below H_1 which drives the system into the topological insulating state. In the case of HgTe the critical thickness was found to be $d_c = 6.3\,\text{nm}$ [9]. Fig. 2.3a shows the calculated dispersion relation of a quantum well with $d < d_c$ (trivial insulator). In Fig. 2.3b the same calculation was done for $d > d_c$. With the Fermi energy E_F lying in the band gap of HgTe it becomes possible to get conducting electronic states at the interface of a CdTe /HgTe heterostructure.

The in blue and red depicted energetic states (Fig. 2.3b) are called surface states. In order to understand their behavior and origin an effective model Hamiltonian will be discussed in the next section.

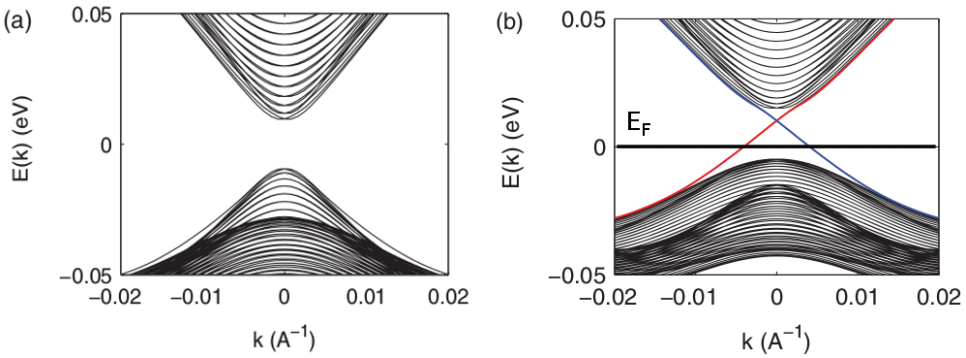

Figure 2.3: Calculated energetic dispersion of a thin (a) and a thick (b) quantum well. In (b) the inversion of E_1 and H_1 subbands leads to formation of surface states. In principle a Fermi energy E_F could be placed inside the gap leading to conducting electronic states at sites where it cuts the surface states. Picture is taken and modified from [1].

2.2.2. Effective Model Hamiltonian

In 2006 Bernevig, Hughes and Zhang (BHZ) introduced a model which describes the physics of the edge states of a two-dimensional topological insulator in CdTe /HgTe quantum wells [8]. In 2009 H. Zhang developed, based on the BHZ model, a model for three-dimensional topological insulators of the Bi_2Se_3 family of materials [10]. The following presentation of the theoretical background is based on the review of [1]. Within the model for a 3D TI the orbital states of Bi and Se undergo changes due to the impact of chemical bonding, crystal field splitting and spin-orbit coupling (SOC) until they form the conduction and valence bands of Bi_2Se_3. The inversion that drives the system into a topological insulator phase occurs at a high enough SOC strength when the energetic levels $|P1_z^+\rangle$ and $|P2_z^-\rangle$ cross. This is similar to the crossing of E_1 and H_1 in chapter 2.2.1. The model Hamiltonian is written in the basis $|\Psi\rangle = \{|P1_z^+,\uparrow\rangle, |P2_z^-,\uparrow\rangle, |P1_z^+,\downarrow\rangle, |P2_z^-,\downarrow\rangle\}$ and has the following form:

$$
\begin{aligned}
\hat{H} &= \tilde{H}_0 + \tilde{H}_1, \\
\tilde{H}_0 &= \tilde{\epsilon}(k_z) + \begin{pmatrix} \tilde{M}(k_z) & A_1 k_z & 0 & 0 \\ A_1 k_z & -\tilde{M}(k_z) & 0 & 0 \\ 0 & 0 & \tilde{M}(k_z) & -A_1 k_z \\ 0 & 0 & -A_1 k_z & -\tilde{M}(k_z) \end{pmatrix}, \\
\tilde{H}_1 &= D_2 k_\perp^2 + \begin{pmatrix} -B_2 k_\perp^2 & 0 & 0 & A_2 k_- \\ 0 & B_2 k_\perp^2 & A_2 k_- & 0 \\ 0 & A_2 k_+ & -B_2 k_\perp^2 & 0 \\ A_2 k_+ & 0 & 0 & B_2 k_\perp^2 \end{pmatrix}.
\end{aligned}
\tag{2.1}
$$

Here $\tilde{\epsilon}(k_z) = C + D_1 k_z^2$ and $\tilde{M}(k_z) = M - B_1 k_z^2$. The parameters $A_{1,2}, B_{1,2}, C_{1,2}, D_{1,2}$ and M depend on the considered material system. Furthermore the Hamiltonian describes the behavior

in the half-space $z > 0$ representing the region of the topologically non-trivial material (the interface lies at $z = 0$). The Hamiltonian is invariant under time-reversal symmetry, inversion symmetry and $C_3(z)$ symmetry. The crucial parameter that drives the system into a topological non-trivial phase is the mass term M. From $\tilde{H}_0$ in equ. 2.1 one can see that for a negative sign of $\tilde{M}(k_z)$ the $|P1_z^+\rangle$ state is energetically favored over $|P2_z^-\rangle$ state (as $E_0 \propto \langle\Psi|\,\tilde{H}_0\,|\Psi\rangle$) resulting in a band inversion and a topological non-trivial insulating state of the system.

For determining the surface state at the Γ-point $\tilde{H}_1$ can be neglected due to $k_x = k_y = 0$. By considering an infinite system k_z has to be replaced by the operator $-i\partial_z$ so that the full Schrödinger equation reduces to

$$\tilde{H}_0\left(k_z \to -i\partial_z\right)\Psi = E\Psi, \tag{2.2}$$

where the eigenstates can be written as

$$\Psi_\uparrow = \begin{pmatrix} \Psi_0(z) \\ \mathbf{0} \end{pmatrix}, \qquad \Psi_\downarrow = \begin{pmatrix} \mathbf{0} \\ \Psi_0(z) \end{pmatrix}. \tag{2.3}$$

Here $\mathbf{0}$ is a two component 0 vector. The solution of equ. 2.2 can be obtained analytically by neglecting $\tilde{\epsilon}(-i\partial_z)$ and assuming a possible solution at $E = 0$:

$$\Psi_0(z) = \left\{ \begin{array}{ll} a\left(e^{\lambda_1 z} - e^{\lambda_2 z}\right)\Phi_+, & A_1/B_1 > 0 \\ c\left(e^{-\lambda_1 z} - e^{-\lambda_2 z}\right)\Phi_-, & A_1/B_1 < 0 \end{array} \right\} \tag{2.4}$$

where $\Phi_\pm$ is a two component spinor defined by $\pm\Phi_\pm = \sigma_y\Phi_\pm$ (σ_y is the Pauli matrix) and $\lambda_{1,2} = \frac{1}{2B_1}\left(A_1 \pm \sqrt{A_1^2 - 4MB_1}\right)$. The coefficients a and c can be determined by boundary conditions and normalization. With the acquired solutions it is now possible to derive an effective surface hamiltonian by projecting the bulk hamiltonian onto the surface states [1, 11]:

$$H_{Surf}(k_x, k_y) = C + A_2\left(\sigma_x k_y - \sigma_y k_x\right), \tag{2.5}$$

where $\sigma_{x,y}$ are the Pauli matrices. In order to solve the eigenvalue equation for the surface Hamiltonian in equ. 2.5 one simply needs to diagonalize the Hamiltonian

$$\begin{aligned} & \left(H_{Surf} - E\mathbb{1}\right)\hat{\Psi} = 0 \\ \Rightarrow \qquad & \det\begin{bmatrix} -E & A_2k_+ \\ A_2k_- & -E \end{bmatrix} = 0 \\ \Rightarrow \qquad & E^2 - A_2k_+ \cdot A_2k_+ = 0 \\ \Rightarrow \qquad & E_\pm = \pm A_2\sqrt{k_+k_-} = \pm A_2\,|k|\,, \end{aligned} \tag{2.6}$$

where $k_\pm = k_x \pm ik_y$. The result of equ. 2.5 is a linear dispersion relation $E(\vec{k})$ with spins

pointing perpendicular to the direction of $\vec{k}$ (Fig. 2.4). While the helicity of the spin texture depends on the sign of A_1/B_1, the slope of the dispersion relation is given by $\hbar \cdot v = A_2$ in terms of velocity v of the surface states. Here v is actually the Fermi velocity $v_F \approx 5.0 \cdot 10^5\,\mathrm{m/s}$ [1].

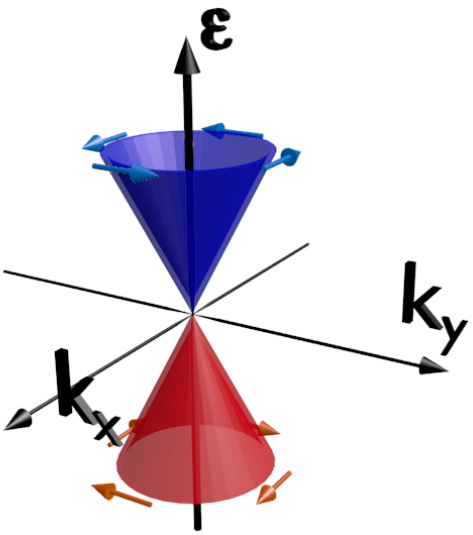

Figure 2.4: Representation of spin polarized surface states on top of a 3D TI. The specific features of the sruface states are the linear dispersion relation and the perpendicular relation between spin direction (indicated by arrows) and momentum.

2.3. Electronic Transport in 3D topological Insulators

One of the important features of a 3D TI is the perpendicular relation between spin direction and momentum also known as spin-momentum locking. Due to this behavior it is possible to extract a general relationship between current density $\vec{j}(y)$ and spin density $\vec{S}(x)$ whenever an electric field $\vec{E}(y)$ is applied:

$$\vec{j}(y) = v\left[\Psi^\dagger(y)\vec{\sigma}\Psi(y) \times \hat{\vec{z}}\right] = v\vec{S}(x) \times \hat{\vec{z}}. \tag{2.7}$$

The expression in equ. 2.7 results from the Hamiltonian in equ. 2.5 [12]. The $\hat{\vec{z}}$ vector is the unity vector in z-direction.

According to Boltzmann transport theory the situation of charge carriers being accelerated in the direction of an electric field and simultaneously colliding with lattice sites leads to the same equilibrium state as represented by a shift of all electronic states in k-space. The shift happens along the field direction and is proportional to the field value. In the case of a 3D TI the total spin density $\vec{S}(x) = 0$ at $\vec{E} = 0$ as every spin at $\vec{k}$ can be compensated by a spin at $-\vec{k}$ at a specific Fermi energy E_F. As soon as $\vec{E} \neq 0$ the whole Fermi surface shifts resulting in a

tilt of spins due to spin-momentum locking and thus leading to an effective spin accumulation (Fig. 2.5)

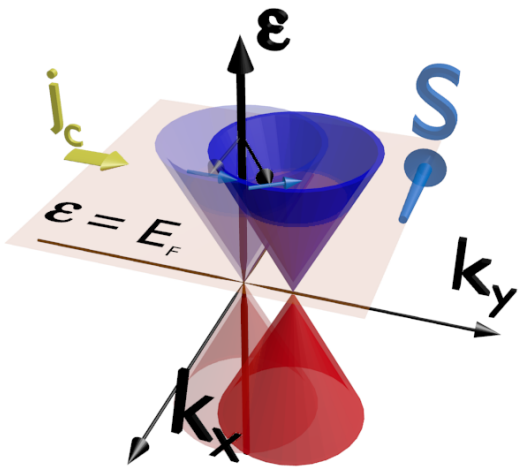

Figure 2.5: Representation of a shift of the surface states due to an external current density $\vec{j}_c$ (resulting from an electric field $\vec{E}$). The shift happens at the Fermi energy E_F and leads to tilting of the spin due to spin-momentum locking resulting in a net spin accumulation perpendicular to the current.

2.4. Summary

Looking at the intrinsic band structure of HgTe shows that the Γ_6 and Γ_8 bands are inverted. With the Γ_8 band being doubly degenerate intrinsic HgTe forms a semi metal. By growing HgTe on $Cd_{0.68}Hg_{0.32}Te$ it is possible to induce strain which lifts the degeneracy and opens a band gap of $\Delta E = 22\,\text{meV}$ allowing for placement of a Fermi energy inside the gap. In contrast to other TIs HgTe can be grown reliably as an inulator. As bands of the same symmetry connect while forming heterostructures it comes to an inevitable crossing of bands as soon HgTe is grown on $Cd_{0.68}Hg_{0.32}Te$. Furthermore the Fermi energy cuts bands of different parity which results in the existence of electronic surface states. These can be described by a theoretical model given by the surface Hamiltonian of equ. 2.5. The peculiarities of the surface states are the linear dispersion relation and the spin-momentum locking where spin and momentum $\vec{k}$ are oriented perpendicular to each other inside the surface plane. This feature also allows for accumulation of a spin density by applying a current along the surface.

References

[1] X.-L. Qi and S.-C. Zhang, *Topological insulators and superconductors,* Reviews of Modern Physics **83**, 1057 (2011).

[2] D. Chadi, J. P. Walter, M. L. Cohen, Y. Petroff, and M. Balkanski, *Reflectivities and electronic band structures of cdte and hgte,* Physical Review B **5**, 3058 (1972).

[3] M. L. Cohen and T. Bergstresser, *Band structures and pseudopotential form factors for fourteen semiconductors of the diamond and zinc-blende structures,* Physical Review **141**, 789 (1966).

[4] M. Cardona, *A fine point on topological insulators,* Physics Today **63**, 10 (2010).

[5] L. Liu and W. Leung, *Transport property of zero-gap semiconductors under tensile stress,* Physical Review B **12**, 2336 (1975).

[6] A. V. Germanenko and G. M. Minkov, *Narrow-gap and gapless semiconductors under uniaxial stress. energy spectrum and galvanomagnetic phenomena,* physica status solidi (b) **184**, 9 (1994), https://onlinelibrary.wiley.com/doi/pdf/10.1002/pssb.2221840102 .

[7] C. Brüne, C. Liu, E. Novik, E. Hankiewicz, H. Buhmann, Y. Chen, X. Qi, Z. Shen, S. Zhang, and L. Molenkamp, *Quantum hall effect from the topological surface states of strained bulk hgte,* Physical Review Letters **106**, 126803 (2011).

[8] B. A. Bernevig, T. L. Hughes, and S.-C. Zhang, *Quantum spin hall effect and topological phase transition in hgte quantum wells,* science **314**, 1757 (2006).

[9] M. König, S. Wiedmann, C. Brüne, A. Roth, H. Buhmann, L. W. Molenkamp, X.-L. Qi, and S.-C. Zhang, *Quantum spin hall insulator state in hgte quantum wells,* Science **318**, 766 (2007).

[10] H. Zhang, C.-X. Liu, X.-L. Qi, X. Dai, Z. Fang, and S.-C. Zhang, *Topological insulators in bi 2 se 3, bi 2 te 3 and sb 2 te 3 with a single dirac cone on the surface,* Nature physics **5**, 438 (2009).

[11] C.-X. Liu, X.-L. Qi, H. Zhang, X. Dai, Z. Fang, and S.-C. Zhang, *Model hamiltonian for topological insulators,* Physical Review B **82**, 045122 (2010).

[12] S. Raghu, S. B. Chung, X.-L. Qi, and S.-C. Zhang, *Collective modes of a helical liquid,* Physical review letters **104**, 116401 (2010).

3

Tunnel Barriers on HgTe

The tunnel effect can be utilized in the framework of semiconductor devices where charge current between two materials is governed by properties of a separating insulator, namely the tunnel barrier. The main purpose of the tunnel barrier, used for the SOT-device in this thesis, is to separate the FM $Ni_{80}Fe_{20}$ (free layer) from etched HgTe in a TI-I-FM structure. This kind of junction will be present in the final device geometry where the TI serves as a current channel. The schematic depicted in fig. 3.1 shows the two current paths that are present in the SOT-device. By using ZrO_2 as the insulator it is possible to make the barrier very thin as this material can be easily grown by atomic layer deposition. This is important as the coupling between spins and the magnetic moments gets smaller with increasing distance. Furthermore ZrO_2 is stable against oxidation which offers higher reproducibility when the sample gets exposed to air during fabrication [1].

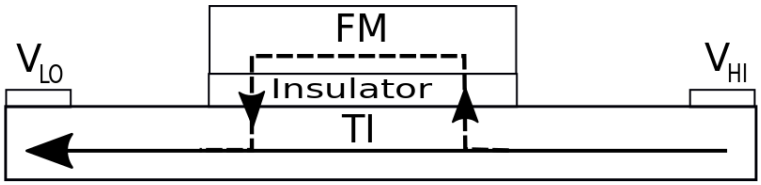

Figure 3.1: Schematic representation of the two current paths for a vertical electric field along the TI in a TI-I-FM heterostructure.

The final resistance area product should be $R \cdot A \approx 3\,\mathrm{k\Omega\mu m^2}$ in order to get $R \approx 20\,\mathrm{k\Omega}$ as the resistance of the tunnel barrier of the final device which has an area of $0.12\,\mu\mathrm{m}^2$. This ensures that the current through the barrier is reduced so that the biggest fraction of electrons is traveling below the insulator as this leads to higher spin accumulation and finally to less current

needed for observing the SOT effect.

This chapter addresses the theoretical background for tunneling between two metallic leads as test structures consist of an FM on one side and metallic surface states on the other side. Based upon this the main features of a working tunnel barrier get derived. The device fabrication process is discussed briefly. The main focus is set on experimental results. At the end of this chapter one test sample is checked for suitability for thermopower measurements.

3

3.1. Preliminary Considerations

3.1.1. Theoretical Background

The charge current between two metals is governed by properties of all materials involved in the process. As depicted in Fig. 3.2 there are multiple ways for an electron to pass the tunnel barrier.

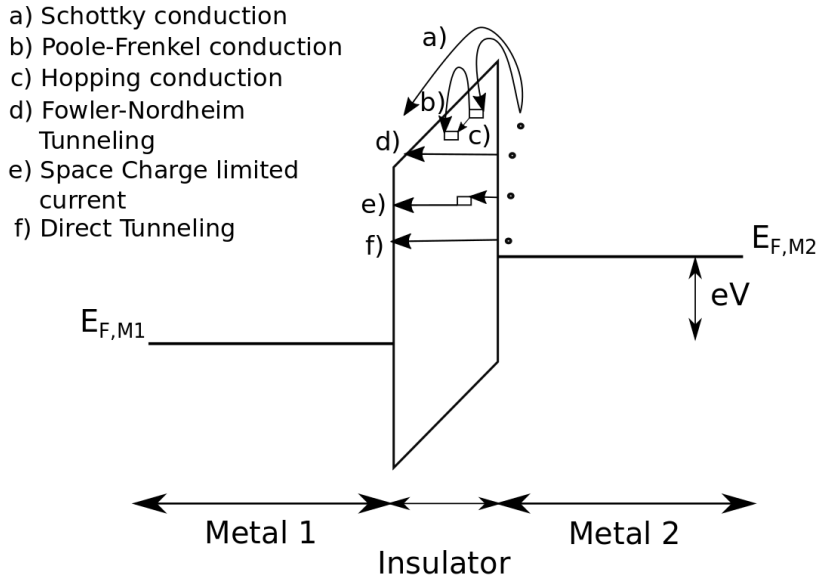

Figure 3.2: Representation of different tunneling mechanisms between two metals separated by an insulating barrier. Picture was adopted from [2].

By applying a Voltage V between the metals the conduction and valence bands of the insulator get tilted in real space. Very high energetic electrons (usually thermionic) can overcome the barrier and relax to the other side along the conduction band, a process called Schottky conduction (Fig. 3.2a). Localized states near the conduction band inside the insulator offer thermionic electrons to travel in small distances through the insulator (Fig. 3.2b). In highly disordered materials the conduction of electrons at low temperatures mainly happens by "hopping" from one close electronic state to another (Fig. 3.2c). It was Mott who defined a typical length l_{VRH} which increases with decreasing temperature according to [3]:

$$\sigma_{VRH} \propto exp\left(-l_{VRH}\right) \propto exp\left[\left(-1/T\right)^{1/4}\right]. \tag{3.1}$$

Another form of tunneling arises from the tilt of the conduction band as above certain energies the thickness of the barrier varies with energy (Fig. 3.2d). Injected electrons have the possibility to be "trapped" inside energetically deep states lying inside the insulator. As a consequence space charges form which limit the current through the barrier (Fig. 3.2e). The dominant transport mechanism for thin barriers is direct tunneling (Fig. 3.2f). Here electrons travel through the

barrier depending on their energy, the barrier height and barrier thickness. A more detailed description of the above mentioned and additional transport mechanisms is given in [4].

There are different models which describe charge transport between two metallic leads separated by a thin insulator. The most famous ones are the model according to Simmons [5] and according to Brinkman, Dynes and Rowell (BDR) [6]. The Simmons model focuses on the nonlinearity of the I-V curve gained by putting a voltage on the barrier and measuring the resulting current on a reference resistor. Subsequently barrier parameters like thickness and height can be extracted. The BDR model on the other hand handles this by measuring the conductance G(V) which shows usually a parabolic behavior. The modeled current densities of both models have the same origin, namely Fermi's golden rule

$$P_{\mu\nu} = \frac{2\pi}{\hbar}\delta\left(E_\mu^{M1} - E_\nu^{M2}\right)\left|M_{\mu\nu}\right|^2, \tag{3.2}$$

which describes the transition rate between two electronic states μ and ν (with eigenenergies E_μ and E_ν) according to the matrix element $M_{\mu\nu}$ [7]. The term $\delta\left(E_\mu^{M1} - E_\nu^{M2}\right)$ assures that only elastic tunneling between the states in metal 1 and metal 2 (Fig. 3.2) is considered. For the calculation of the tunneling current occupied states of one side have to reach unoccupied states of the other side. The probability of an electronic state being occupied is given by the fermi function $f(E - E_F)$. As the tunneling current is proportional to $2eP_{\mu\nu}$ (prefactor due to spin) the two currents for tunneling from $M1$ to $M2$ and vice versa are given by

$$\begin{aligned} I_{M1\to M2} &= \frac{4\pi e}{\hbar}\sum_{\mu\nu} f\left(E_\mu^{M1} - E_F^{M1}\right)\left[1 - f\left(E_\nu^{M2} - E_F^{M2}\right)\right]\left|M_{\mu\nu}\right|^2 \delta\left(E_\nu^{M2} - E_\mu^{M1} - eV\right) \\ I_{M1\leftarrow M2} &= \frac{4\pi e}{\hbar}\sum_{\mu\nu} f\left(E_\mu^{M2} - E_F^{M2}\right)\left[1 - f\left(E_\nu^{M1} - E_F^{M1}\right)\right]\left|M_{\mu\nu}\right|^2 \delta\left(E_\nu^{M2} - E_\mu^{M1} - eV\right). \end{aligned} \tag{3.3}$$

By introducing a density of states $n(E)$ the sum $\sum_\mu$ turns into an integral $\int n(E)dE$ as the energetic eigenvalues consist of a continuum leading to a total tunneling current of

$$\begin{aligned} I = \frac{4\pi e}{\hbar}\int_0^{eV} dE\left[f\left(E_F^{M1} - eV + E\right) - f\left(E_F^{M2} + E\right)\right] \\ \times n^{M1}\left(E_F^{M1} - eV + E\right) n^{M2}\left(E_F^{M2} + E\right)\left|M(E)\right|^2, \end{aligned} \tag{3.4}$$

where n^{M1} and n^{M2} are the density of states at metal 1 and metal 2 respectively.

Within a slowly varying tunnel barrier potential $V(x)$ (assuming x as the tunneling direction) the Wentzel-Kramers-Brillouin (WKB) approximation can be used to describe $M(E)$ in equ. 3.4

$$M(E) = exp\left(\frac{-4\pi}{h}\int_0^d \left[2m(V(x) - E)\right]^{1/2} dx\right), \tag{3.5}$$

where d is the thickness of the tunnel barrier [5]. The equ. 3.5 is valid for metal-insulator-metal and for metal-insulator-semiconductor structures as the band-bending of a semiconductor has only little influence on the transmission coefficient [8]. In Simmons' model $V(x)$ gets rewritten in terms of an average potential $\bar{\phi}(V)$ that depends explicitly on the applied voltage V so that the total current results in a dependence of

$$I \propto V \cdot exp(V), \tag{3.6}$$

which is non linear in an I-V plot. In the model according to BDR $V(x)$ is described as $\phi(x, V)$ which depends on the two barrier heights of metal 1 and metal 2. The derivative of the total current with respect to V becomes

$$dI/dV \propto \alpha V + \beta V^2, \tag{3.7}$$

where α and β are functions of the mean barrier height, thickness and the difference in barrier heights [6]. Independent of α and β the behavior in equ. 3.7 is generally parabolic.

3.1.2. Features of a working Tunnel Barrier

With the review given in section 3.1.1 the main features of a working tunnel barrier can be extracted. The first indication for a working tunnel barrier is its increase in resistance with decreasing temperature. This behavior is valid for barriers with many defects where transport happens mainly through hopping (equ. 3.1) as well as for barriers with direct tunneling as the dominant mechanism. In the latter case the tunneling current has a thermal contribution of $j(V,T) \propto j(V,0) \cdot (1 + \gamma \cdot T^2)$, with γ depending on barrier thickness and barrier height [9]. As a consequence the resistance $r \propto dV/dI$ increases with decreasing temperature. Another indication of a tunnel barrier is its exponential growth of resistance with barrier thickness. This feature stems from equ. 3.5 where the WKB approximation takes the thickness as the integrand of the argument of the exponential function. In general an exponential function dominates the behavior so that the depiction of the logarithmic resitance area product of a tunnel barrier as a function of thickness should show linear behavior. Lastly a working tunnel barrier should be non linear in an I-V plot and mainly parabolic in conductance $G(V)$ according to equs. 3.6 and 3.7 respectively.

It is mainly the last two properties that are commonly used as a proof for working tunnel barriers. Nevertheless it was shown that also the temperature dependence should be taken into account as it rules out conductance via pinholes [10].

3.2. Device Fabrication

3.2.1. Geometric Design

As a first step a geometry has to be designed in order to measure the properties of ZrO_2 on top of HgTe . Thus the device geometry has to exhibit the following properties:

- The metal-insulator-metal (M-I-M) structure consists of $Ni_{80}Fe_{20}$ as one of the leads, ZrO_2 as the tunnel barrier and edged HgTe as the other lead
- The $Cd_{0.68}Hg_{0.32}Te$ /HgTe /$Cd_{0.68}Hg_{0.32}Te$ heterostructure has to be characterizable as growth and/or lithographic procedures could alter the usability of the material
- The maximum number of contacts on a chip carrier is 18 which limits the number of tunnel barriers
- In order to minimize the probability for pinholes the area size of a MIM structure should lie in the limits of photolithographic procedures
- The whole device structure should be as symmetric as possible so that parasitic potential differences can be minimized

All mentioned properties are implemented in the device geometry shown in Fig. 3.3.

Figure 3.3: Representation of the device geometry used to investigate on the behavior of tunnel barriers on edged HgTe . The inset shows the layer stack at the site of the MIM structure used in the experiment.

A standard Hall bar design allows for determination of charge carrier density and mobility. Both parameters can be calculated from standard measurements where a biasing voltage gradient $V_{1,9}$ is set between contacts 1 and 9 while a magnetic field perpendicular to the geometry plane is swept and the voltage drops $V_{15,3}$ and $V_{3,5}$ are acquired [11]. Appropriate values for densities are $n \approx 10^{11}\,\mathrm{cm}^{-2}$ and $\mu \approx 100\,\mathrm{cm}^2/(\mathrm{Vs})$ for mobilities. The maximum number of contacts per

chip carrier leads to a total number of three M-I-M structures on one sample. Within those restrictions it is possible to make redundant top contacts (contacts 4,6 and 12,14) which in principle allow for pseudo 4-terminal measurements. The main channel depicted in Fig. 3.3 shows only at the sites of the M-I-M structures the presented layer stack. For the rest of the channel the $Cd_{0.68}Hg_{0.32}Te$ cap is not supposed to be removed in order to keep high mobilities [12]. Furthermore the device structure should be symmetric. In the case of Hall leads this is necessary in order to avoid contributions from the longitudinal resistance. Another reason is to avoid pickup due to thermal voltages. As the main channel (1,9) contains heated electrons due to a charge current a perpendicular symmetric temperature gradient can be build up. In this case a symmetric positioning of the metallic leads at the Hall probes would result in the same temperature at the opposite junctions. This in turn nullifies a thermal voltage as an additional contribution.

3.2.2. Lithography Process

With the preliminary considerations of the geometric structure being in place a lithographic process can be developed. The main aim is to develop a tunnel barrier of certain resistance area product which stops charge carriers to move freely into the ferromagnet. The shape of the tunnel barrier is in general not critical. Thus a bigger area would provide the same information as a smaller sized pillar. As the resolution for the process is not critical an optical lithography process is favored over an electron-beam lithography process. Consequently a higher yield in combination with shorter processing times is provided. Fig. 3.4 shows microscope pictures of all steps of the lithographic process from its beginning to the end.

First alignment marks are defined together with three central pillars (Fig. 3.4a). The total structure occupies an area of 2x2 mm^2 where the pillars have an area of 5x5 μm^2 each. Ion beam etch (IBE) with argon ions is used to etch away the capping $Cd_{0.68}Hg_{0.32}Te$ layer at the pillar sites [13]. Now ZrO_2 gets deposited via atomic layer deposition (ALD) where Zr containing chemicals and O_2 containing water are sequentially pulsed into a reaction chamber under constant pressure and temperature [14]. This process method allows for conformal growth and accurate thickness. In the case of the machine used in this thesis the typical growth per cycle has an approximate value of 0.16 nm. Continuing with lithography the mesa is defined by Argon milling of the full $Cd_{0.68}Hg_{0.32}Te$ /HgTe /$Cd_{0.68}Hg_{0.32}Te$ layer stack. The dimensions of the main channel in Fig. 3.4b are 10x40 μm^2. After depositing the Au contacts (Fig. 3.4c) the whole area gets covered with 50 nm of SiN by plasma enhanced chemical vapor deposition (PECVD) [15]. Now it is possible to etch SiN via reactive ion etching (RIE) at the inner of the Au contacts and the center of the pillars (Fig. 3.4d). Finally a path between contacts and pillars can be defined so that evaporated Ti and Au are used to contact both areas directly without shorting the mesa (Fig. 3.4e). The final device is shown in Fig. 3.4f. A precise description of the process is given in the recipe in appendix A.

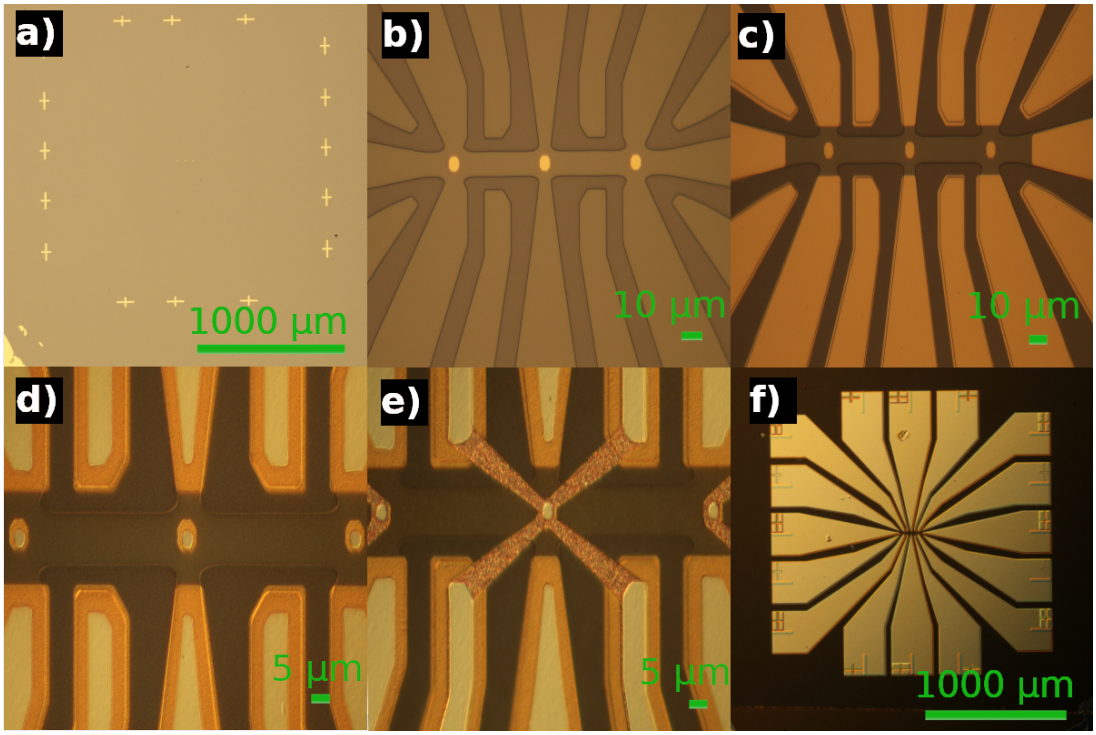

Figure 3.4: Microscope pictures of all optical lithographic process steps for a tunnel barrier device. Starting with the placement of alignment marks and pillars (a) the mesa (b) can be etched and contacts (c) can be deposited. Small 2x2 μm^2 holes are etched into deposited SiN (d). Finally Au gets deposited contacting the outer Au pads and the central pillars (e,f).

3.3. Experimental Results

3.3.1. Measurement Procedure

The measurement procedure for all samples can be described according to Fig. 3.5.

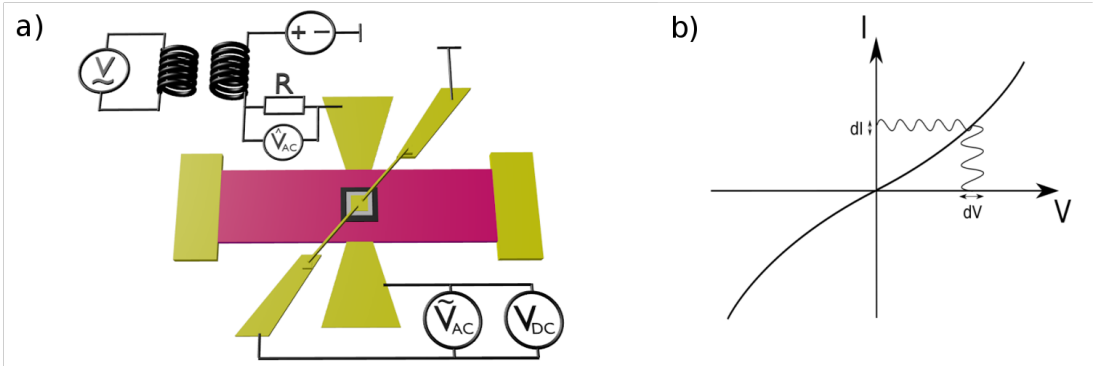

Figure 3.5: Schematic representation of measurement procedure for tunnel junctions. The measurement circuit (a) shows a small AC voltage inductively superimposed on a DC voltage and applied over the barrier. The resulting DC and AC signals are measured separately. The total differential current is measured by the voltage drop over the reference resistor R. In the case of I-V measurements the dc source is fed directly into R so that only DC voltages get measured. In (b) the influence of an AC voltage on a sample with non-linear $I(V)$ curve is shown. A small biasing ac signal leads to a periodic response at the sample according the slope of the $I(V)$ curve.

In Fig. 3.5a the schematic shows the main HgTe channel and one pillar together with four measurement contacts and two outer channel contacts. One of the top contacts is used as a measurement ground while one of the bottom contacts is connected to a source. The bias signal consists of a DC voltage source with an superimposed AC voltage. Both are coupled inductively allowing for measurements of $dV/dI(V)$ curves at the two opposite contacts. The measurement of V_{DC} gives the values of the $x-axis$ of the $dV/dI(V)$ curve while V_{AC} at the reference resistor R and at the sample give dI and dV respectively. The signal can be understood in the context of an $I(V)$ curve in Fig. 3.5b. Here an AC biasing signal (dI) results in a periodic response of the sample (dV) according the slope of the $I(V)$ of the sample. Thus the AC part of the source results in a voltage drop $\hat{V}_{AC}$ across R which leads to $dI = \hat{V}_{AC}/R$ on one hand. On the other hand a voltage drop across the sample $\tilde{V}_{AC} = dV$ is gained and the resistance of the barrier can be calculated by $r(V_{DC}) = dV/dI$. In the case of I-V measurements the DC source is directly connected to R (no transformator) so that only DC voltages get measured.

3.3.2. Confirmation of tunneling Behavior

As mentioned in section 3.1.2 a working tunnel barrier has to exhibit a weak insulating temperature dependence, a non-linear $I(V)$ curve, a parabolic dI/dV curve and an exponential increase in resistance with barrier thickness. For all working tunneling devices the differential resistance ($dV/dI(V=0)$) increased when cooling down. The amount of change is usually not predictable and ranges between factors of 2 and 50. This big fluctuation could arise from not having sufficient control over trap states in the barrier as the deposition happens through low temperature ALD. Collected water from preceded operations can disturb the growth process significantly. As a consequence the current through the barrier gets limited by space charges leading to a bigger increase in resistance (Fig. 3.2e). A typical graph of the behavior of differential resistance at cool down is shown in Fig. 3.6.

The sample *QC0509 O 13c* has GaAs as the substrate which allows for back gating and a much bigger amount of samples (2 inch wafer) but also introduces additional surface roughness due to lattice mismatch between CdTe and GaAs . The description O and $13c$ in the sample name stand for 15th sample (letter O in alphabet) with 13 cycles of ZrO_2 used ($d \approx 2\,\mathrm{nm}$). Although surface roughness should be minimized in building tunneling devices the benefit to build different samples on the same wafer is more preferable. Furthermore the focus lies on gaining about $20\,\mathrm{k\Omega}$ as resistance of the tunnel barrier which is an empirical value [16]. In order to reach this for the SOT-device where the pillars exhibit an area of $0.12\,\mu\mathrm{m}^2$ a resistance area product of $R \cdot A \approx 3\,\mathrm{k\Omega}\mu\mathrm{m}^2$ is needed.

Further evidence of proper tunneling behavior is given in Fig. 3.7. Here the shown samples exhibit non-linear $I(V)$ dependence (Fig. 3.7a) and parabolic dI/dV curves (Fig. 3.7b). All samples show the presented behavior. Fitting the curves according to models discussed in section 3.1 do not yield reasonable parameters for barrier thicknesses and heights as those models focus on pure M-I-M structures while the present layer stack is of the form FM-I-TI.

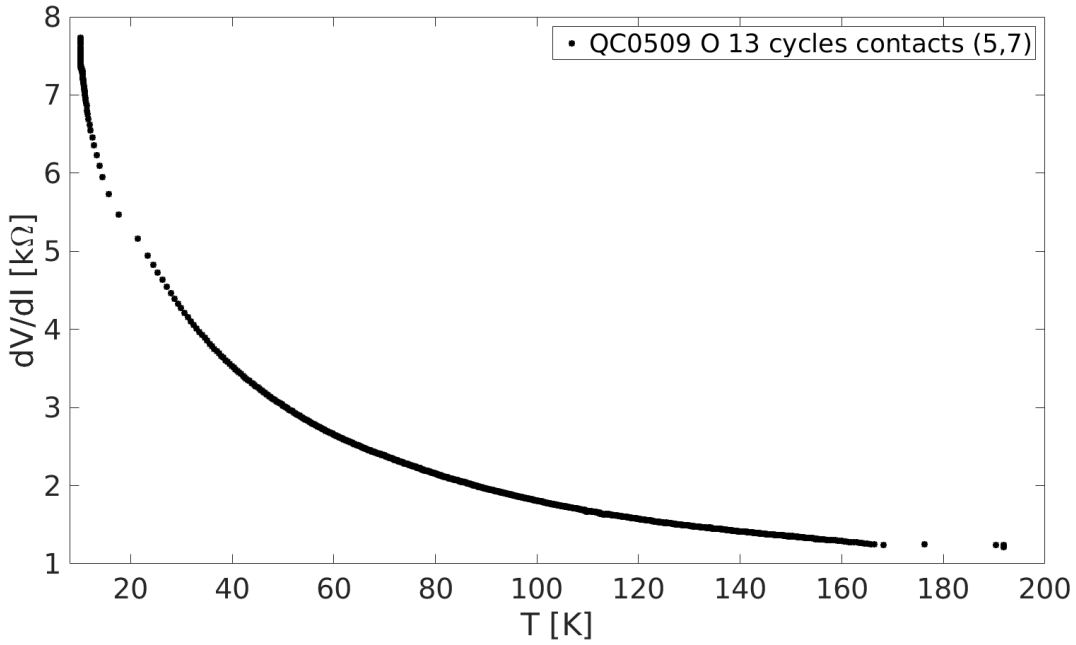

Figure 3.6: Typical behaviour of differential resistance of a tunneling device at cool down. The shown sample belongs to a wafer on GaAs as the substrate and is the 15th sample (letter O) made out of that wafer. The tunnel barrier has a thickness of 13 cycles of ZrO_2 which is approximately 2 nm.

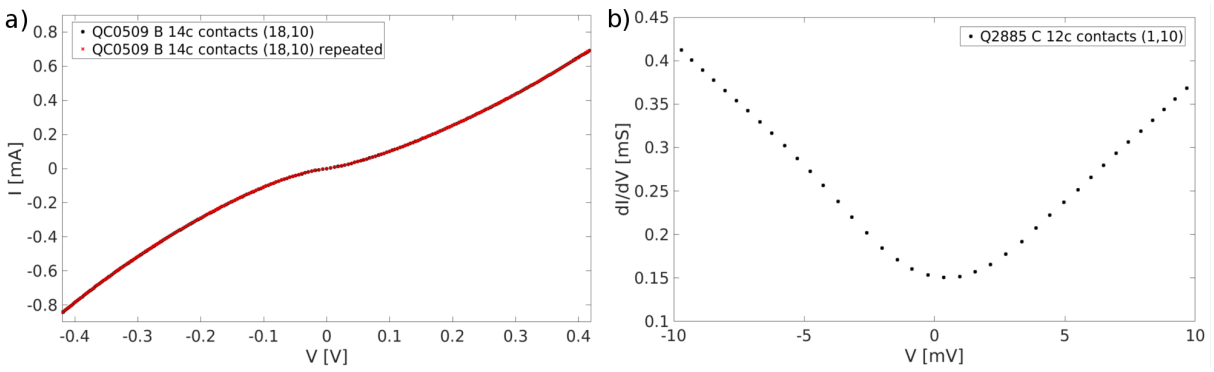

Figure 3.7: Depiction of measured non-linear $I(V)$ (a) and parabolic dI/dV (b) curves of QC0509 B 14c and Q2885 C 12c.

Lastly the resistance area product values $R \cdot A$ of all working tunnel barriers are presented in Fig. 3.8. The general trend is an increase with rising thickness. As the scattering ranges over two orders of magnitude it is not possible to determine an exact slope for gaining an accurate cycle number which corresponds to $R \cdot A \approx 3\,\mathrm{k\Omega\mu m^2}$. Nevertheless it becomes obvious from Fig. 3.8 that 10 cycles of ZrO_2 lead most likely to the desired $R \cdot A$. Values at 14 cycles are of the same order as values at 20 cycles so that saturation occurs early leading to a small window of 10 to 15 cycles where resistances are acceptable. Samples with barriers of 11 cycles were built at the end to provide additional information. Unfortunately the ALD machine stopped working at this time so that only one sample could be produced. Out of the three pillars only one showed tunneling behavior.

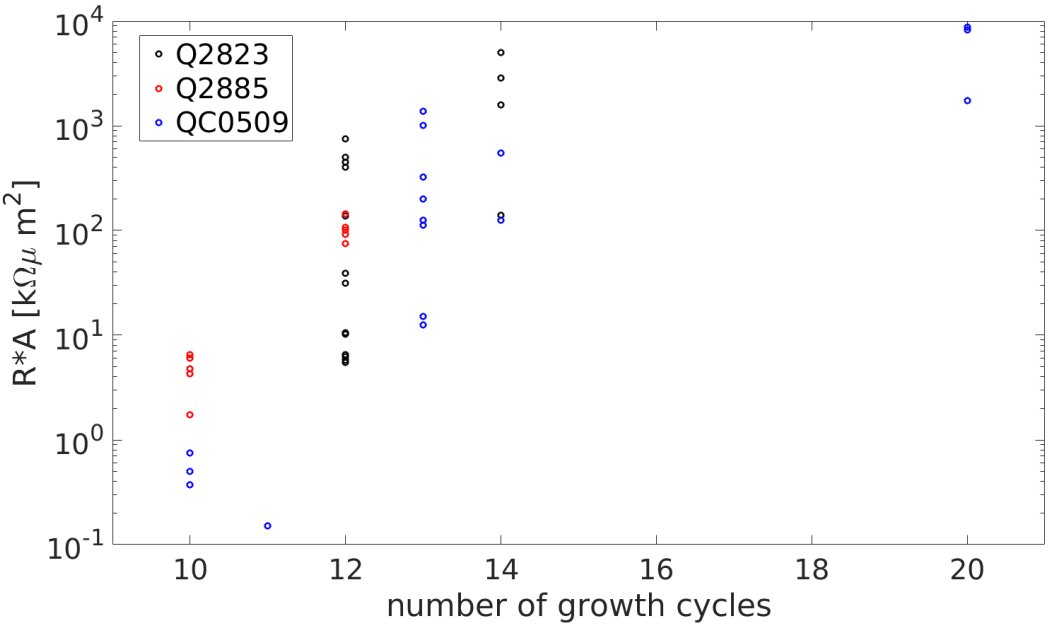

Figure 3.8: Representation of the differential resistance area product $R \cdot A$ as a function of thickness. Samples are made out of three different wafers. The area of the pillars is always $25\,\mu\mathrm{m}^2$. The thickness per cycle has an approximate value of 0.16 nm.

3.4. Suitability for Thermopower Measurements

According to the device geometry in Fig. 3.3 all samples can be used to perform thermopower measurements. In this case an AC bias voltage of V_ω is applied at the left and right contact of Fig. 3.5a while the resulting signal of twice the frequency $V_{2\omega}$ is measured between top and bottom contacts (Fig. 3.9).

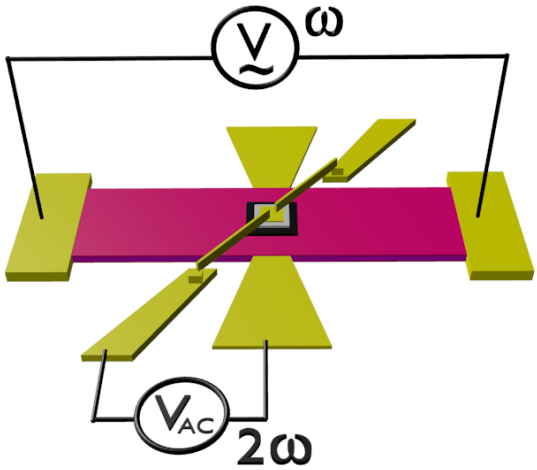

Figure 3.9: Schematic representation of the measurement circuit for thermopower measurements of tunnel junctions.

The background for the need of $V_{2\omega}$ is that due to $I_\omega = V_\omega / R \propto \sin(\omega t)$ the resulting heating

power can be expressed as $P_{heat} = RI_\omega^2 \propto \sin^2(\omega t) \propto \sin(2\omega t)$. In this case it is assumed that the heating energy mainly excites the electron system rather than the lattice which is constantly cooled at $T = 4.2\,\mathrm{K}$. As a result electrons in the heating channel have higher temperature than electrons at the ferromagnetic top contact. This temperature gradient leads to diffusive tunneling until the increased charge concentration is high enough to balance the influx. This charge concentration is the potential difference $V_{2\omega}$.

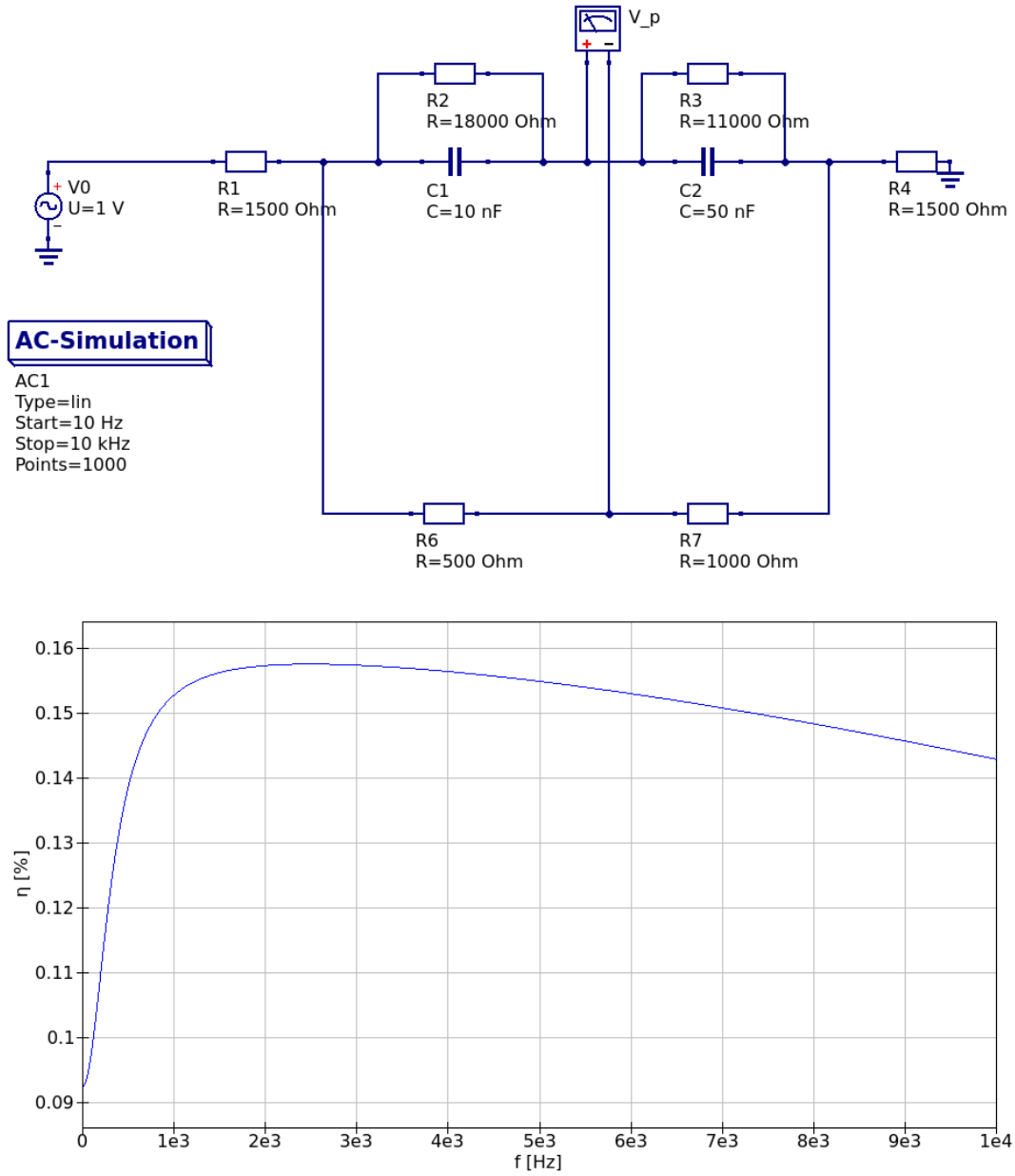

Figure 3.10: Equivalent circuit for thermopower measurements where the ratio $\eta = V_{p,\omega}/V_0$ can be simulated. $V_{p,\omega}$ is the parasitic potential that overlays with $V_{2\omega}$ while V_0 is the input voltage. Asymmetries in resistances and capacitances lead to the shown η behavior. The simulation was carried out by *Qucs* [18].

In general a tunnel junction can be modeled as a circuit with a tunnel resistance R_T being set in parallel with a capacitance C_T [17]. For the given geometry in Fig. 3.9 the current path is defined between the left and right contacts. On its way the current has to split into two channels, one going through the tunnel barrier and the other going below and at the sides of the junction. As some current goes through the barrier a pick up of a parasitic voltage $V_{p,\omega}$ at frequency ω can be expected. If the value of $V_{p,\omega}$ is much higher than $V_{2\omega}$ the measurement of the thermopower cannot be trusted as it is unclear which influences $V_{p,\omega}$ on $V_{2\omega}$ has. By putting capacitances and resistances of realistic values into a circuit simulator one can gain the behavior of the parasitic voltage $V_{p,\omega}$ with respect to frequency (Fig. 3.10) [18].

All resistances of the HgTe channel are distributed according to $R_{sample} \approx 5\,\mathrm{k}\Omega$. There are two capacitance-resistance pairs as the current is assumed to tunnel in at a different spot than tunneling out. By introducing an asymmetry among the pairs and among the resistances below the pillar, one gets the $V_{p,\omega}/V_0(f)$ curve shown in Fig. 3.10. Such a frequency sweep has been carried out for one of the junctions of sample *QC0509 A* (Fig. 3.11).

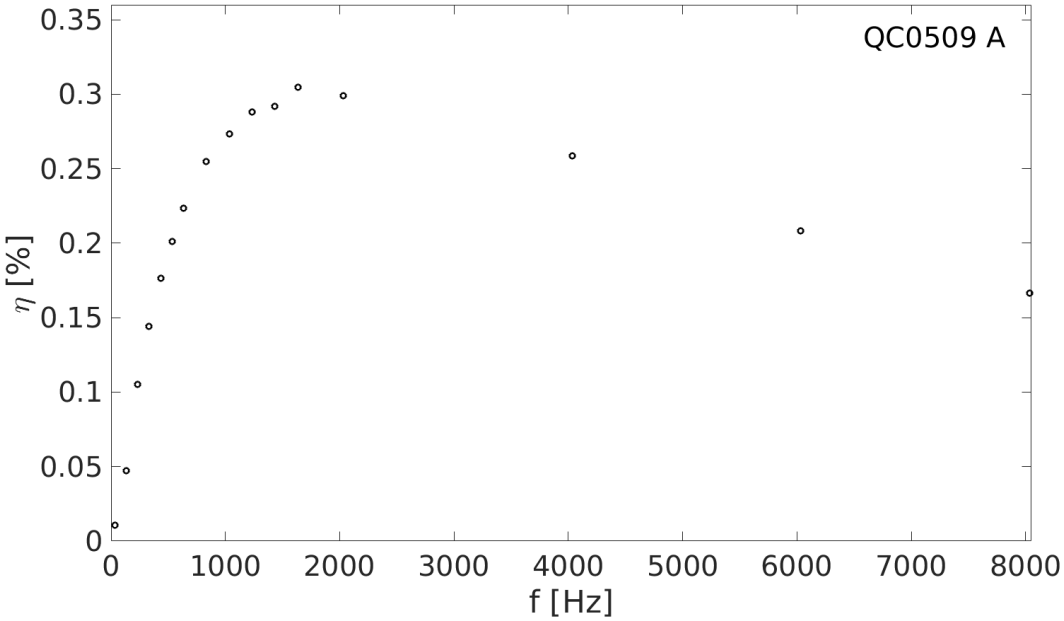

Figure 3.11: Representation of $\eta = V_{p,\omega}/V_{input}$ behavior against frequency for one of the tunnel junctions in *QC0509 A*.

Comparing the results of $\eta = V_{p,\omega}/V_{input}$ in Fig. 3.10 and 3.11 shows the same qualitative behavior so that the model seems to cover the important features. As a consequence it can be assumed that an asymmetry along the tunnel barrier can indeed cause high pick-ups of a parasitic potential $V_{p,\omega}$. This potential than overlaps with $V_{2\omega}$ and results in a ω dominated signal. In all measurements the ratio between $V_{p,\omega}$ and $V_{2\omega}$ has been approximately $V_{p,\omega}/V_{2\omega} \approx 100$. Trying to notch out the $V_{p,\omega}$ resulted in ratios of $V_{p,\omega}/V_{2\omega} \approx 1 - 10$ which is still too high for deriving proper conclusions.

3.5. Summary

The SOT-device contains FM-I-TI structures where the FM serves as a tool for sensoring the effect of torques originating from moving surface state electrons. In order to avoid high currents running through the FM, which would alter the effect, an insulating layer has to be deposited. Due to its peculiarities, like stability against oxidation and the possibility to grow it in ALD, ZrO_2 is chosen to serve as the insulator. Its properties lead to the development of a thin tunnel barrier which still exhibits a high resistance.

The results of built tunnel barriers have been compared to features that define working tunnel barriers. These are the weak insulating temperature dependence, non-linear $I(V)$ and parabolic dI/dV curves and lastly an exponential resistance increase with barrier thickness. All junctions shown in this chapter exhibit the mentioned behaviors. The pillar area of the SOT-device is nominally $0.12\,\mu\mathrm{m}^2$. By aiming for a tunnel resistance of $R_T \approx 20\,\mathrm{k}\Omega$ a resistance area product of $R \cdot A \approx 3\,\mathrm{k}\Omega\mu\mathrm{m}^2$ would be needed which is possible by growing 10 cycles of ZrO_2 . This is roughly equivalent to a barrier thickness of $d \approx 1.6\,\mathrm{nm}$.

The design and simulation of an equivalent circuit for thermopower measurements leads to the conclusion that asymmetries at the interfaces can result in a high pick up of parasitic voltages. Those voltages would overlap with the thermal voltages of interest which complicate proper conclusions.

References

[1] M. Mamun, H. Baumgart, and A. Elmustafa, *Ald zirconium oxide (zro2) thin films mechanical/structural properties for high-tech applications,* ECS Journal of Solid State Science and Technology **4**, Q35 (2015).

[2] H. Bentarzi, *Review of transport mechanism in thin oxides of mos devices,* in *Transport in Metal-Oxide-Semiconductor Structures* (Springer, 2011) pp. 29–37.

[3] Y. Xu, D. Ephron, and M. Beasley, *Directed inelastic hopping of electrons through metal-insulator-metal tunnel junctions,* Physical Review B **52**, 2843 (1995).

[4] F.-C. Chiu, *A review on conduction mechanisms in dielectric films,* Advances in Materials Science and Engineering **2014** (2014).

[5] J. G. Simmons, *Generalized formula for the electric tunnel effect between similar electrodes separated by a thin insulating film,* Journal of applied physics **34**, 1793 (1963).

[6] W. F. Brinkman, R. Dynes, and J. Rowell, *Tunneling conductance of asymmetrical barriers,* Journal of applied physics **41**, 1915 (1970).

[7] S. Lounis, *Theory of scanning tunneling microscopy,* arXiv preprint arXiv:1404.0961 (2014).

[8] R. Putman and R. Van Overstraeten, *Influence of band-bending on the tunnelling probability in mis structures,* physica status solidi (a) **9**, 247 (1972).

[9] J. G. Simmons, *Generalized thermal j-v characteristic for the electric tunnel effect,* Journal of Applied Physics **35**, 2655 (1964).

[10] B. Jönsson-Åkerman, R. Escudero, C. Leighton, S. Kim, I. K. Schuller, and D. Rabson, *Reliability of normal-state current–voltage characteristics as an indicator of tunnel-junction barrier quality,* Applied Physics Letters **77**, 1870 (2000).

[11] S. Datta, *Electronic Transport in Mesoscopic Systems*, Cambridge Studies in Semiconductor Physics and Microelectronic Engineering (Cambridge University Press, 1995).

[12] C. Becker, C. Brüne, M. Schäfer, A. Roth, H. Buhmann, and L. Molenkamp, *The influence of interfaces and the modulation doping technique on the magneto-transport properties of hgte based quantum wells,* physica status solidi c **4**, 3382 (2007).

[13] V. Srivastav, R. Pal, and H. Vyas, *Overview of etching technologies used for hgcdte,* OPTOELECTRONICS REVIEW **13**, 197 (2005).

[14] M. Leskelä and M. Ritala, *Atomic layer deposition (ald): from precursors to thin film structures,* Thin solid films **409**, 138 (2002).

[15] L. Liu, W.-g. Liu, N. Cao, and C.-l. Cai, *Study on the performance of pecvd silicon nitride thin films,* Defence Technology **9**, 121 (2013).

[16] T. Naydenova, P. Dürrenfeld, K. Tavakoli, N. Pégard, L. Ebel, K. Pappert, K. Brunner, C. Gould, and L. Molenkamp, *Diffusion thermopower of (ga, mn) as/gaas tunnel junctions,* Physical review letters **107**, 197201 (2011).

[17] H. Grabert and M. H. Devoret, *Single charge tunneling: Coulomb blockade phenomena in nanostructures*, Vol. 294 (Springer Science & Business Media, 2013).

[18] M. Brinson and V. Kuznetsov, *Qucs-0.0.19s: A new open-source circuit simulator and its application for hardware design,* in *2016 International Siberian Conference on Control and Communications (SIBCON)* (2016) pp. 1–5.

4

Characteristic behavior of ferromagnetic Trilayers on 3D HgTe in an external magnetic Field

In order to measure the efficiency of SOT in 3D HgTe it is indispensable to implement a sensor on top of the spin generating current channel. A ferromagnetic trilayer stack, consisting of $Ni_{80}Fe_{20}$ /Cu /$Co_{50}Fe_{50}$, serves as an instrument for this. The combination of the soft FM $Ni_{80}Fe_{20}$ (free layer) and hard $Co_{50}Fe_{50}$ (reference layer) gives a measurable giant magnetoresitance (GMR) signal that contains two distinguishable resistance states. These are necessary to capture instant and irreversible changes of the GMR which are induced by a DC current.

The following chapter contains a small summary of the theoretical behavior of magnetic moments in an external magnetic field. Additionally a simulation of two interacting magnetic moments is presented in order to show the main features of measured SQUID curves. Furthermore emphasis is set on the sample preparation as the crystal axis of the used sample is a critical parameter for the development of an preferred orientation direction of the trilayer. The focus is set on experimental results of SQUID and ferromagnetic resonance (FMR) measurements. At the end of the chapter an array of ellipse shaped sub-micron layer stacks is shown in order to investigate the average features of a sensor.

4.1. Preliminary Considerations

4.1.1. Theoretical Background

Ampère deduced that moving charges produce a magnetic field [1]. The simplest circuit that can generate a magnetic field, is a circular loop of area A carrying a current I and therefore generating a magnetic dipole moment

$$\vec{m} = I \cdot \vec{A}, \tag{4.1}$$

which is considered to be the most elementary quantity of magnetism [2]. In ferromagnetically ordered solids of volume V one can define a normalized quantity called magnetization $\vec{M} = \vec{m}/V$. The easiest way to model the behavior of a ferromagnet in an external magnetic field B_{ext} is to represent it by one single magnetization. The change of $\vec{M}$ can than be described by the well known Landau-Lifschitz-Gilbert (LLG) equation

$$\frac{d\vec{M}}{dt} = -\gamma \vec{M} \times \vec{B}_{ext} + \frac{\alpha}{M} \vec{M} \times \frac{d\vec{M}}{dt}, \tag{4.2}$$

where γ is the gyro-magnetic ratio and α is the Gilbert damping factor [3]. The first term leads to a precession of $\vec{M}$ around $\vec{B}_{ext}$ while the second term damps the motion in order to align $\vec{M}$ with $\vec{B}_{ext}$ (Fig.4.1).

Microscopic ferromagnetic domains usually exhibit one or more natural directions of magnetizations [2]. With $\vec{M}$ pointing along one favored direction $-\vec{M}$ gives the same energetic state. This stems from the fact that magnetism can be associated by circulating electron currents giving rise to time reversal symmetry. In that sense it is possible to define an *easy axis* with a corresponding anisotropy energy per unit volume

$$E_a = K_U \cos^2(\theta) \tag{4.3}$$

where K_U is the anisotropy constant and θ the angle between $\vec{M}$ and one easy axis. In the case of two easy axes the energy can be described by [4]

$$E_1 = K_1 \sin^2(2\theta). \tag{4.4}$$

Magnetic anisotropy has multiple sources like shape, crystal symmetry, external fields and interaction with neighboring magnetizations. Equs. 4.3 and 4.4 can be used to represent simple magnetocrystalline anisotropies like uniaxial and cubic, respectively. Typical values for Co (uniaxial) are $K_U = 4.1 \cdot 10^5\,\mathrm{J/m^3}$ and for Fe (cubic) $K_1 = 0.48 \cdot 10^5\,\mathrm{J/m^3}$ [1].

In the final SOT-device the GMR stack is shaped into an elliptical cylinder which height is one order of magnitude smaller than its width or length. This introduces shape anisotropy with an energy per unit volume given by [5]

$$E_{Demag} = 1/2\mu_0 \cdot M^2 \cos^2(\theta). \tag{4.5}$$

This allows to push the easy axis into a desired direction defined during the lithographic process. The SOT-device in this thesis contains two ferromagnets which are separated by a thin non-magnetic Cu layer. As a result an additional energy term, namely the exchange energy per unit volume

$$E_{ex} = J \cdot cos(\theta_1 - \theta_2), \tag{4.6}$$

is present, where J is the coupling constant and θ_1 and θ_2 represent the angle with respect to the easy axes of the corresponding magnetization M_1 and M_2. For $J > 0$ the exchange energy E_{ex} is maximum at $\theta_1 - \theta_2 = 0°$ and minimum at $\theta_1 - \theta_2 = 180°$. Thus anti-ferromagnetic coupling between M_1 and M_2 is favored. For $J < 0$ analogously ferromagnetic coupling is favoured.

The influence of an external magnetic field on a magnetization can be described by the Zeeman energy per unit volume [1, 4]

$$E_Z = -\vec{M} \cdot \vec{B}_{ext} = -M \cdot B_{ext} \cdot \cos(\theta - \theta_H), \tag{4.7}$$

where $\vec{B}_{ext} = \mu_0 \vec{H}_{ext}$ is the external magnetic field, θ is the angle between easy axis and magnetization $\vec{M}$ and θ_H is the angle between easy axis and external magnetic field. The origin of this term is that magnetic moments tend to align with an external energy source (magnetic field) in order to minimize the potential energy.

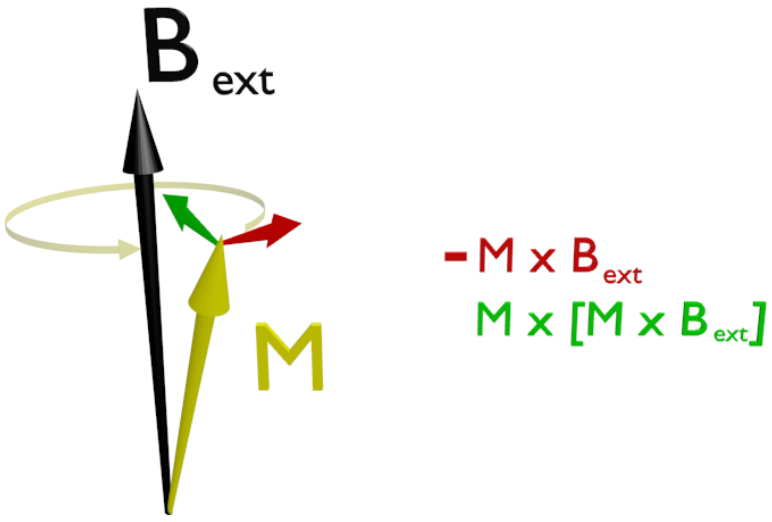

Figure 4.1: Schematic of magnetization behavior in an external magnetic field. The two terms on the right show the main contribution for the motion of $\vec{M}$ in $\vec{B}_{ext}$.

By neglecting shape anisotropy the total energy reads

$$\begin{aligned} E &= E_{a1} + E_{a2} + E_{11} + E_{12} + E_{Z1} + E_{Z2} + E_{ex}, \\ &= K_{U1}\sin^2(\theta_1) + K_{U2}\sin^2(\theta_2) \\ &+ K_{11}\sin^2(2\theta_1) + K_{12}\sin^2(2\theta_2) \\ &+ M_1 \cdot B_{ext}\cos(\theta_1 - \theta_H) + M_2 \cdot B_{ext}\cos(\theta_2 - \theta_H) \\ &+ J \cdot cos(\theta_1 - \theta_2) \end{aligned} \tag{4.8}$$

for a system with two separate but interacting single domain magnetizations. The total energy in equ. 4.8 contains the uniaxial crystalline anisotropies E_{a1} and E_{a2} for the two material systems forming $\vec{M}_1$ and $\vec{M}_2$. Furthermore contributions of cubic crystalline anisotropies E_{11} and E_{12} are incorporated as well. The energy terms E_{Z1} and E_{Z2} are mandatory as they describe the influence of an external field on $\vec{M}_1$ and $\vec{M}_2$. Lastly the exchange interaction between the two magnetizations is represented by E_{ex}.

For the investigation of the behavior of a GMR stack on HgTe only thin films of ferromagnets are used. As the shape is not a critical parameter it is appropriate to use $3\times3\,\mathrm{mm}^2$ squared sample pieces to magnetron sputter the $Ni_{80}Fe_{20}$ /Cu /$Co_{50}Fe_{50}$ /Ta /Ru multilayer. This approach has the advantage of higher yield and faster processing time. In the final SOT-device the multilayer stack is shaped into a thin $600 \times 200\,\mathrm{nm}^2$ oval cylinder inducing shape anisotropy to support the easy axis orientation given by the crystal structure.

In order to understand the mechanism behind changes of a magnetization at the presence of an external magnetic field it is necessary to understand what happens inside a ferromagnetically ordered solid. A ferromagnet consists of multiple domains (Weiss domains) which contain large numbers (up to 10^{15}) of atomic moments that are locally saturated and pointing at a certain direction. In the demagnetized state those directions differ from domain to domain in a random manner leading to a total magnetization of 0. By applying an external field domains with magnetic moments pointing in the same direction as $\vec{B}_{ext}$ start to grow while other domains start to diminish. First the magnetization of the domains aligns with the easy axis closest to $\vec{B}_{ext}$ until the external field gets high enough so that all moments point in the same direction as $\vec{B}_{ext}$ reaching the saturation magnetization M_0. All those processes are governed by the minimization of the total energy in equ. 4.8. In one dimension the energetic landscape with uniaxial anisotropy and $B_{ext} \neq 0$ can take the shape shown in Fig. 4.2. The current direction of the magnetization is represented by the red dot at the energetically higher local minimum. With rising B_{ext} also the difference between the two minima rise so that at $\Delta E = \epsilon$ the ferromagnetic system overcomes the domain wall nucleation energy ϵ in order to reach the global energy minimum. At this stage the magnetization points in the opposite direction, meaning it *switched*. This basic principle is used to simulate the behavior of $Ni_{80}Fe_{20}$ and $Co_{50}Fe_{50}$ by taking two different domain nucleation wall energies ϵ_1 and ϵ_2 into account. This allows to demonstrate the main features of SQUID

measurements that will be presented later.

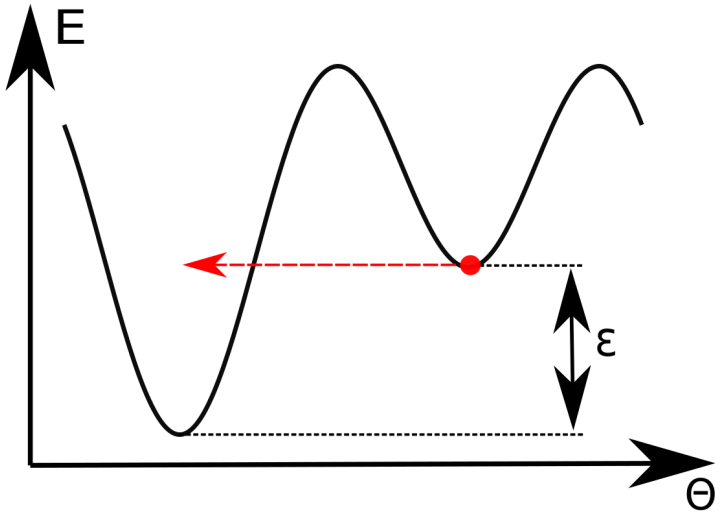

Figure 4.2: Schematic depiction of the energetic landscape of a single magnetization material with uniaxial anisotropy and $B_{ext} \neq 0$. The current magnetization direction (red dot) changes instantly to the next minimum as soon as its energy surpasses the domain wall nucleation energy ϵ.

4.1.2. Simulation of the Energy Landscape of two interacting single domain Magnetizations

In a system consisting of two interacting single domain magnetizations the energy landscape can be described by equ. 4.8. For simplicity the easy axis is chosen to be at $\theta = 0°$. The two material systems of interest are $Ni_{80}Fe_{20}$ (permalloy) and $Co_{50}Fe_{50}$ which are represented by magnetization M_1 and M_2 as well as the angles θ_1 and θ_2 respectively. The external magnetic field $\vec{B}_{ext} = \mu_0 \vec{H}_{ext}$ is applied homogeneously in the x-y plane and points at the direction defined by θ_H (Fig. 4.3).

The energetic landscape can be visualized by defining a grid of θ_1 and θ_2 values. The saturation magnetizations are chosen to be $M_{0,1} = 800$ kA/m for $Ni_{80}Fe_{20}$ and $M_{0,2} = 1500$ kA/m for $Co_{50}Fe_{50}$ [6]. The volume of the samples is $V = d \cdot A$, where the thickness d of one layer is aimed to be $d = 10$ nm while the area A can be adjusted to the value measured under the microscope or SEM. For the following simulation results only an uniaxial anisotropy of $K_{U,1} = 10$ kJ/m^3 and $K_{U,2} = 8$ kJ/m^3 is taken into account as it forms the dominant contribution in E_a. Furthermore the coupling constant is chosen to be anti-ferromagnetic with $J = -0.08$ mJ/m^2 to simulate the behavior of an average oval that is used in the final structure. The anti-ferromagnetic coupling arises from the interaction between the stray fields and magnetizations of the layers. For small patterns, where the stray field is strong, the energy of two dipoles $E = -\mu_0 \int \vec{H}_1 \vec{M}_2 dV_2 = -\mu_0 \int \vec{H}_2 \vec{M}_1 dV_1$ (reciprocity theorem) gets minimized by aligning anti-parallel.

Deploying the mentioned parameters and $\theta_H = 0°$ into eq. 4.8 leads to an energetic landscape depicted in Fig. 4.4. At $B_{ext} = -100$ mT the point of lowest energy is $(\theta_1, \theta_2) = (180°, 180°)$

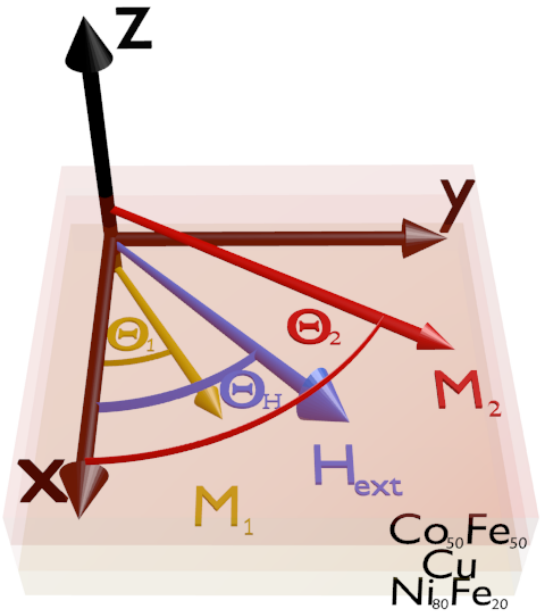

Figure 4.3: Schematic of defined directions for the single domain magnetizations M_1 and M_2 of the two material systems $Ni_{80}Fe_{20}$ and $Co_{50}Fe_{50}$ used for simulations. The easy axes is chosen to be $\phi = 0°$. An external magnetic field is applied homogeneously in the direction of θ_H.

representing M_1 and M_2 pointing in the same direction as B_{ext}. As the external magnetic field reduces to $B_{ext} = -7$ mT, two additional minima at $(0°, 180°)$ and $(180°, 0°)$ form due to the anti-ferromagnetic coupling. The favored energetic state depends on the specific domain wall nucleation energies $\epsilon_1 < \epsilon_2$, as $M_{0,1} < M_{0,2}$. Taking this into account the two ferromagnetic system switches to the state at $(0°, 180°)$. At $B_{ext} = +7$ mT the local minimum at $(180°, 180°)$ start to disappear while a minimum at $(0°, 0°)$ begins to form. This minimum dominates the state at $(180°, 0°)$, which would be unphysical, so that the total state stays at $(0°, 0°)$ as B_{ext} rises.

This simulation shows the main features of measured SQUID curves which will be presented later. Thus it can be assumed that the FM in the layer stack act primarily as single domain magnetizations with uniaxial anisotropies. This leads to the possibility of a simplified description of experimental results.

4.2. Experimental Results of $Ni_{80}Fe_{20}$ /Cu /$Co_{50}Fe_{50}$ Trilayers on HgTe

4.2.1. Measurement Procedures

For the characterization of the trilayers two setups, namely SQUID and FMR, are used. The term SQUID stands for superconducting quantum interference device and is an aperture that allows to measure the magnetic moment of a sample. It utilizes the inducted current of a spatially

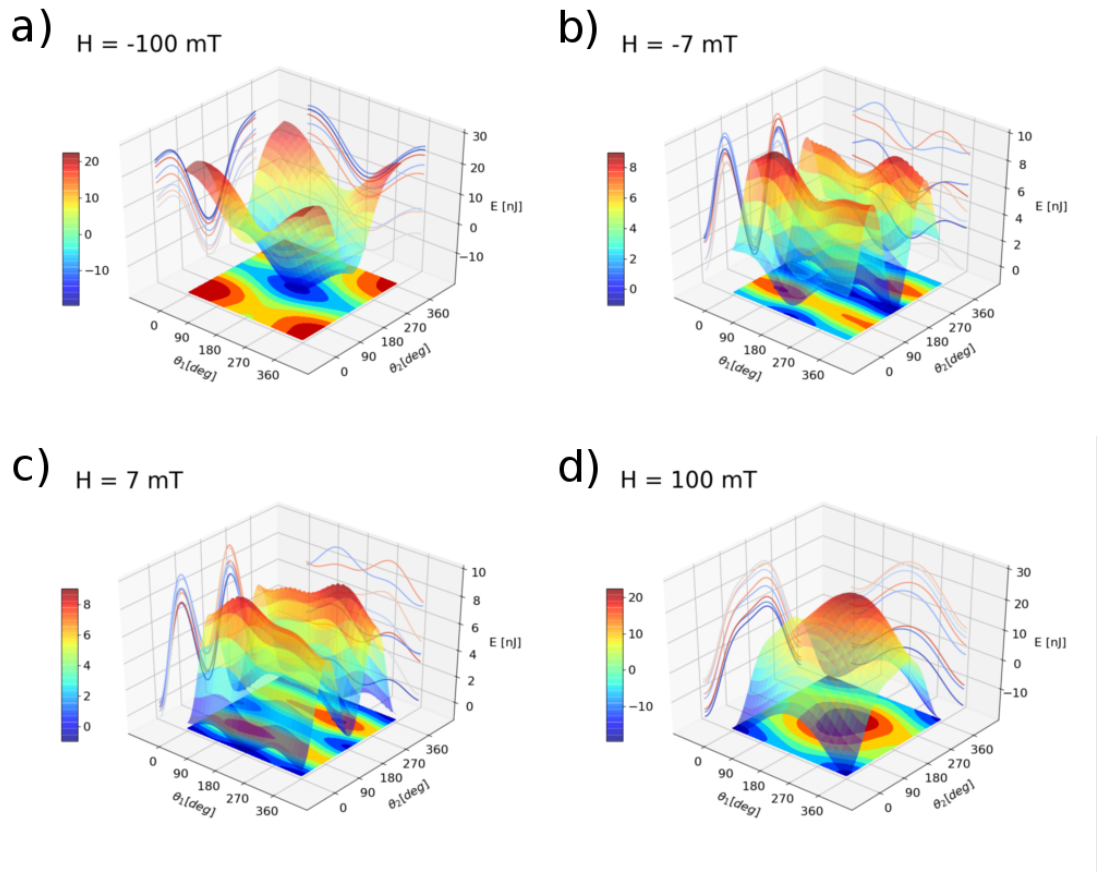

Figure 4.4: Depiction of the simulated energetic landscape for two interacting magnetizations according to eq. 4.8 for different external magnetic fields. Values for constants can be found in the main text.

sweeping magnetization through superconducting coils in order to calculate a value for the magnetic moment. More details are given in [7].

The term FMR stands for ferromagnetic resonance and describes a tool to measure the anisotropy of a sample. The basic principle and functionality can be described as follows.

The Zeeman energy of eq. 4.7 defines the potential energy between a magnetization $\vec{m}$ and an external magnetic field $\vec{B}_{ext}$. In general $\vec{m}$ of an electron can be associated with spin momentum $\hbar\vec{S}$ as

$$\vec{m} = \gamma\hbar\vec{S} = \frac{g\mu_B}{\hbar}\vec{S}, \tag{4.9}$$

where g and μ_B are the g-factor and Bohr magneton respectively. Taking the z component $S_z = m_S = \pm 1/2$ one gets in combination with eq. 4.7 an energy difference of

$$\Delta E = \gamma\hbar B_0 = \frac{g\mu_B}{\hbar}B_0 = \hbar\omega_0, \tag{4.10}$$

where ω_0 is the frequency (Larmor frequency) needed to induce resonant transitions between the two energetic states $E_\pm = \pm g\mu_B B_0/2$. Here $B_{ext} = B_0$ is the resonance magnetic field. This

resonance condition can be achieved by absorbing the energy of an oscillating magnetic field. Maximum absorption occurs when the magnetic field B_{ext} is perpendicular to the oscillating field B_{HF} as it is the precession of the spin around B_{ext} that has to be synchronized. Fig. 4.5a shows a schematic of the $E(B_{ext})$ dependence of a typical FMR measurement. Due to the energy uncertainty $\Delta E \Delta t \approx \hbar$ transitions do not happen sharply at B_0. The resonances occur in Lorentzian forms with temperature and material specific line widths ΔB. Those shapes can be measured directly with the help of coplanar waveguides (CPW) (Fig. 4.5b). It consists of three Au pads deposited on an Si substrate. The central strip carries the high frequency signal (V_{HF}) while the outer conductors serve as ground electrodes [8]. The sample is positioned face down and $\vec{B}_{ext}$ and $\vec{B}_{HF}$ are set to be in the plane of the sample. While B_{HF} has a fixed direction due to the fixed position of the sample on the main strip, the external field direction and strength can be changed. Resonance measurements are taken by sweeping B_{ext} at different angles and stepped frequencies of B_{HF}.

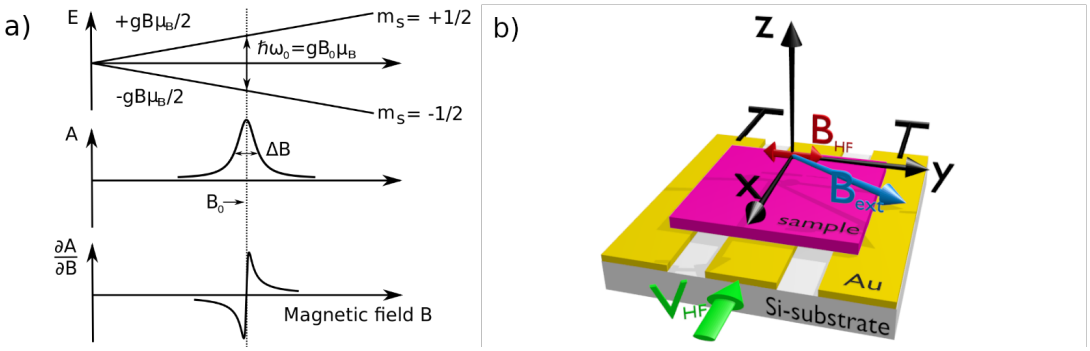

Figure 4.5: Measurement principles of an FMR setup. a) $E(B_{ext})$ dependence in an FMR measurement starting with the energetic splitting of an electron in an external field. Due to the energy uncertainty the absorption follows a Lorentzian with linewidth ΔB and center B_0. b) Schematic of a coplanar waveguide consisting of two ground electrodes and the main strip. The sample is positioned face down and exposed to an oscillating in-sample-plane magnetic field B_{HF} and an adjustable (in direction and strength) in-sample-plane external magnetic field B_{ext}.

4.2.2. Sample Preparation

The first step in developing a GMR trilayer stack for resistance state measurements is investigating the behavior of the ferromagnets on the material under study. MBE grown $Cd_{0.68}Hg_{0.32}Te$ /HgTe /$Cd_{0.68}Hg_{0.32}Te$ layer stacks on a CdTe substrate are prepared by cleaving approximately $A \approx 2 \times 2$ mm^2 pieces. At this point two non-identical edges of the full 1×1 cm^2 wafer have to be defined as *edge* $\vec{\alpha}$ and *edge* $\vec{\beta}$ (Fig. 4.6a). As will be shown later the trilayer exhibits a strong dependency on developing an easy axis along either $(1\bar{1}0)$ or (110). That means whenever starting with an unprocessed CdTe /$Cd_{0.68}Hg_{0.32}Te$ /HgTe /$Cd_{0.68}Hg_{0.32}Te$ wafer one has to define $\vec{\alpha}$ and $\vec{\beta}$ because exactly one of these edges will always be the only appropriate choice for an easy direction.

The next step in preparing the sample is removing the $Cd_{0.68}Hg_{0.32}Te$ capping layer by ion-beam-etching and depositing an ALD layer of 10 cycles (section 3.2.2). Next the sam-

ple is placed on a molyblock which has two bar magnets mounted on it in order to produce a constant magnetic field $\vec{B}_{sputter}$ at the sample site. This technique is used to generate a controlled easy axis direction for the ferromagnets [9]. Finally the GMR layer stack $Ni_{80}Fe_{20}$ (10)/Cu (10)/$Co_{50}Fe_{50}$ (10)/Ta (5)/Ru (5), here numbers in parenthesis indicate thickness in nm, gets magnetron sputtered. The insertion of Ta is known to lead to bigger GMR effects if Ta is placed further than 2 nm away from the FM/NM interface [10]. Ru on the other hand serves as a capping layer due to its high resistance towards oxidation conditions [11].

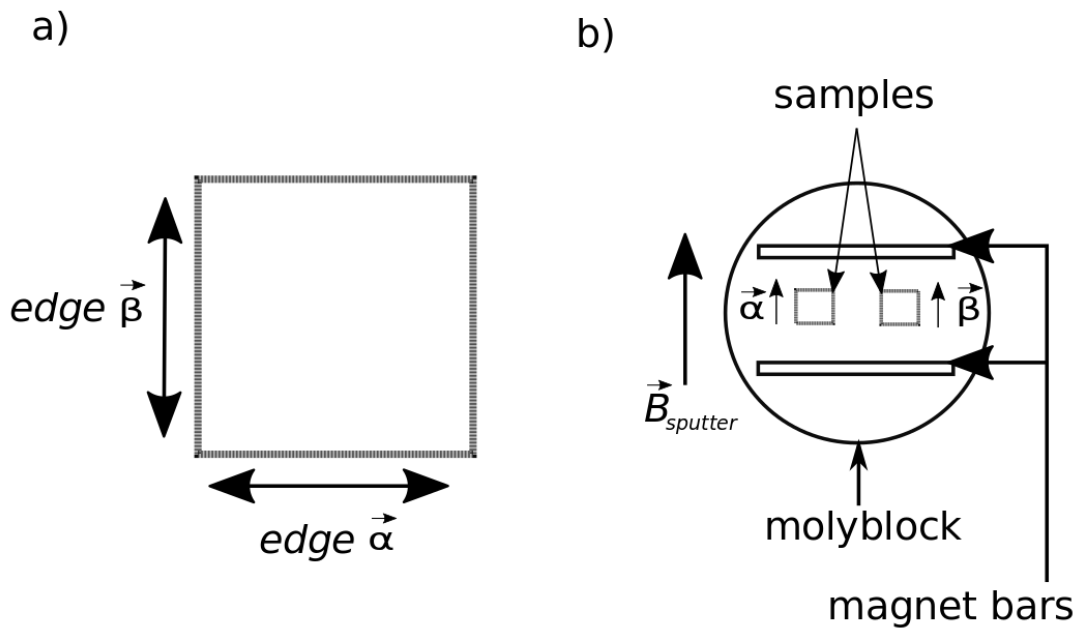

Figure 4.6: Preparation of samples for SQUID and FMR measurements. In a) the non-identical edges $\vec{\alpha}$ and $\vec{\beta}$ are defined. Subsequently two different pieces are placed in different orientations on the molyblock at a constant magnetic field $\vec{B}_{sputter}$ which is used to define an easy direction (b).

Experiments have shown that samples of the same wafer sputtered at $\vec{B}_{sputter} \parallel \vec{\alpha}$ do not yield the same results as sputtered at $\vec{B}_{sputter} \parallel \vec{\beta}$. In order to investigate this behavior samples are placed in pairs on the molyblock so that one sample has its edge $\vec{\alpha}$ and the other its edge $\vec{\beta}$ aligned with $\vec{B}_{sputter}$ (Fig. 4.6b). According to measurements with a Hall sensor at the center of the magnet bars the approximate magnetic field reads $B_{sputter} \approx 100\,\mathrm{mT}$.

4.2.3. SQUID Measurements

The prepared SQUID samples are always measured in two configurations with respect to the external magnetic field of the SQUID $\vec{B}_{SQUID}$, namely *edge* $\vec{\alpha} \parallel \vec{B}_{SQUID}$ and *edge* $\vec{\beta} \parallel \vec{B}_{SQUID}$ at $T = 4.3\,\mathrm{K}$. Scans inside the SQUID are acquired at $T = 300\,\mathrm{K}$ and usually at $\vec{B}_{SQUID} = 0\,\mathrm{mT}$.

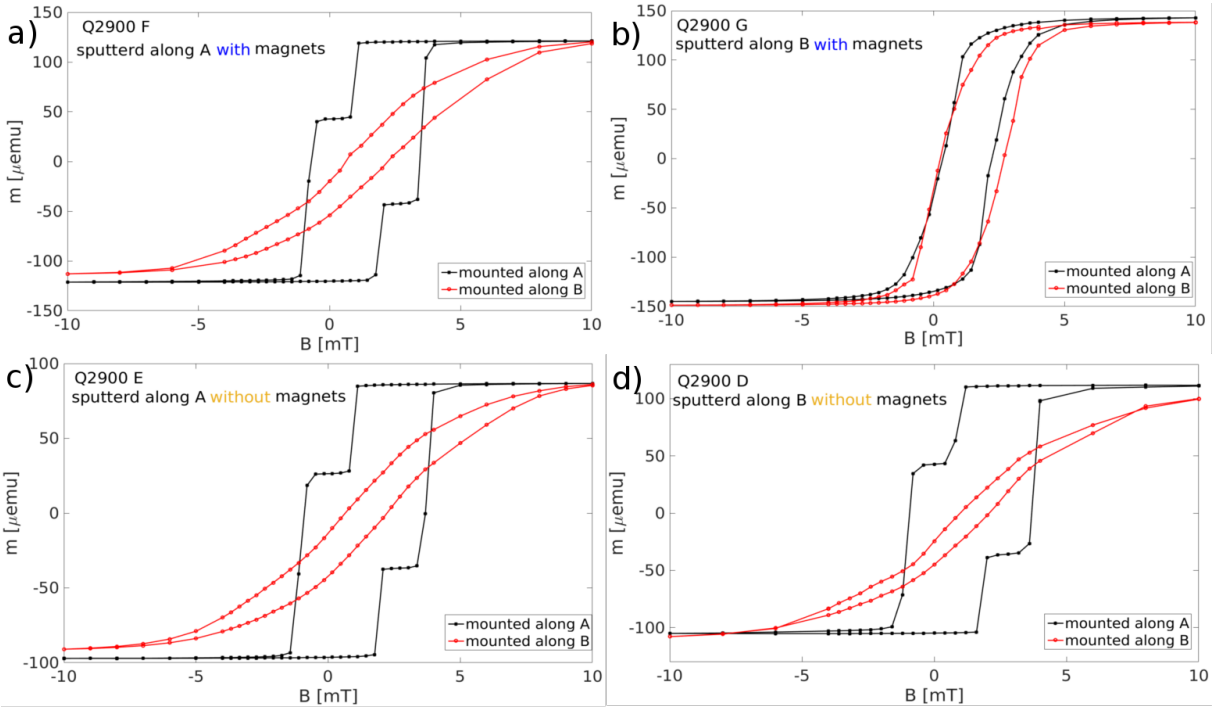

Figure 4.7: Experimental results acquired by SQUID for the HgTe based sample Q2900. Samples were put in pairs into the sputter chamber with either installed bar magnets (a,b) or without them (c,d). Each pair has one sample sputtered along edge $\vec{\alpha}$ as well as $\vec{\beta}$ ($\vec{B}_{sputter} \parallel \vec{\alpha}, \vec{\beta}$). In the case of no magnets the typical direction of $\vec{B}_{sputter}$ is kept as reference.

Fig. 4.7 shows the experimental results that have been acquired by SQUID. All samples are prepared according to sec. 4.2.2 either with or without installed bar magnets. Sample positioning on the molyblock is always taken in reference to $\vec{B}_{sputter}$, so that $\vec{B}_{sputter} \parallel \vec{\alpha}, \vec{\beta}$. In Fig. 4.7a,c,d all samples show similar behavior. It can be clearly distinguished between an easy axis and a hard axis. As two ferromagnets with different magnetizations $M_{0,1}$ and $M_{0,2}$ are involved the absolute value of the magnetic moment $m = \mid \vec{m} \mid$ can reach four different values when $\vec{B}_{SQUID}$ is swept along the easy axis. These four values are $(M_{0,1}+M_{0,2})$, $(-M_{0,1}+M_{0,2})$, $(M_{0,1}-M_{0,2})$ and $(-M_{0,1}-M_{0,2})$. Here transitions happen abruptly by switching. At the hard axis on the other hand the magnetic moment changes smoothly its direction. A completely unexpected behavior can be seen in Fig. 4.7b where m changes smoothly with both $\vec{B}_{SQUID} \parallel \vec{\alpha}$ and $\vec{B}_{SQUID} \parallel \vec{\beta}$. Reconsidering that $\vec{B}_{sputter} \approx 100\,\mathrm{mT}$ this quite astonishing result leads to a constraint for building an SOT-device. Now one has first to find out the correct edge of the virgin wafer in order to gain a behavior similar to Fig. 4.7a. Only if the sample shows the *double step* the final GMR pillar has a chance to deliver a binary resistance curve.

All samples of Fig. 4.7 are measured at values between $B_{SQUID} = \pm 10\,\mathrm{mT}$. Consequently full saturation could not be reached resulting in different values of m at the maximum and minimum magnetic fields. The total values of m for all four samples are different as the sputtered surfaces have different sizes as well as slightly different thicknesses. Nevertheless the measured values for

m fit well to values calculated from magnetization constants $M_{0,1}$ and $M_{0,2}$ given in section 4.1.2. In general all curves are antisymmetric to $B_{SQUID} = 0$. The slight shift to the right side could stem from the SQUID coils as they were not completely demagnetized at the beginning of the measurement.

The results presented in Fig. 4.7 are typical for all $Cd_{0.68}Hg_{0.32}Te$ /HgTe /$Cd_{0.68}Hg_{0.32}Te$ based materials with CdTe substrates. The two crystal directions of those materials are (1 1 0) and ($\bar{1}$ 1 0) as $Cd_{0.68}Hg_{0.32}Te$ and HgTe grow in zinc-blende structure. The two directions can be distinguished depending on the terminating material. Nevertheless all samples have in common that the $Cd_{0.68}Hg_{0.32}Te$ cap first gets etched und subsequently covered by ALD. Thus neither of both directions should be favored and lead to anisotropy. All samples of a wafer behave the same way although conditions during sample preparation do not. Such conditions would be for example the time between IBE and ALD growth or sample positioning on a molyblock before IBE. One could also think about the possibility of drawing furrows during IBE. This would result in an ordering structure which than favors one of the crystal axes. However the sample is rotating during IBE which averages out any sort of ballistic structuring. Another possibility would be the formation of sputter ripples during the sputtering step [9]. But in this case Fig. 4.7c,d would yield qualitatively different results as the only difference between the samples is their orientation on the molyblock. Lastly it is possible to introduce a quasi periodic sequence of mono atomic steps by a miscut of the CdTe wafer [12]. This could lead to an anisotropic behavior of the FM provided that the miscut happens always along one of the two axes. In general a fully grown single crystal is always cut along one direction. Nevertheless the cutting direction is usually not defined resulting in not fixed miscut directions. This makes miscut as a source for the observed anisotropy rather unlikely. It is striking that the easy axis of the system develops along edge $\vec{\alpha}$ although no magnetic field $\vec{B}_{sputter}$ is provided. The reason for this could stem from the topological nature of the material especially because topographic causes seem to be unlikely.

4.2.4. FMR Measurements

FMR measurements have the advantage to easily determine the magnetic anisotropy of a sample. This information is needed to find out whether the energetic landscape of the two magnetizations in the used GMR stack contains local minima that would disturb GMR measurements of the SOT-device. The aim is to produce a stack which GMR signal exhibits two distinct resistance states depending on the applied external magnetic field. Furthermore the transition between these states has to happen abruptly and irreversibly. In order to find out the magnetic anisotropy with the help of the setup described in sec. 4.2.1 one has to set a constant frequency for B_{HF} and sweep the magnetic field while the angle Φ_H for B_{ext} is stepped. Here the sample is always placed with its sputtering direction being parallel with B_{ext} at the start ($\Phi_H = 0$). For example Q2900F has its edge $\vec{\alpha} \parallel \vec{B}_{ext}(\Phi_H = 0)$.

Fig. 4.8 shows a typical result for an absorption measurement. V_{DC} is the detector diode voltage which in turn is proportional to the absorption rate of the ferromagnetic materials. Two

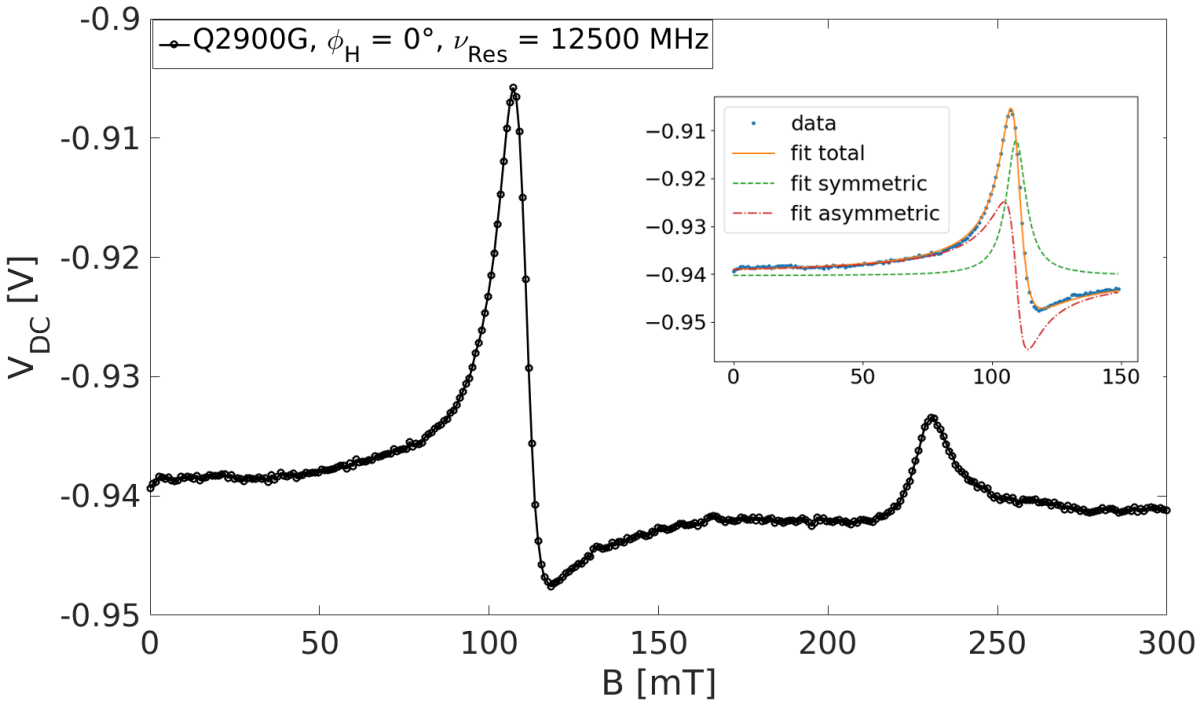

Figure 4.8: Detector diode voltage as a function of B_{ext} for the trilayer. The first and highest peak corresponds to $Co_{50}Fe_{50}$ while the second one belongs to $Ni_{80}Fe_{20}$. The inset shows symmetric and antisymmetric Lorentzian fits on the first peak.

separate peaks can be extracted where the first and also highest one belongs to $Co_{50}Fe_{50}$ while the second peak corresponds to $Ni_{80}Fe_{20}$. Here the distinction is easy to do as the sample is lying face down on the CPW with $Co_{50}Fe_{50}$ becoming the closest FM to the three Au stripes. The further an FM is located from the CPW the smaller the resulting absorption signal gets. This stems from the fact that B_{HF} does not extend far from the CPW leading to stronger coupling of $Co_{50}Fe_{50}$. Furthermore Fig. 4.8 shows an inset depicting a symmetric and antisymmetric Lorentzian on the $Co_{50}Fe_{50}$ peak. Just like the driving current $\vec{j}_{HF} \propto V_{HF}$ has components in the x-y-plane (Fig. 4.5b) also B_{HF} can be separated into two components. With

$$\begin{aligned} \vec{m} &= \chi \vec{H}_{HF}, \\ &= \begin{pmatrix} \chi_{xx} & i\chi_{xy} & 0 \\ -i\chi_{xy} & \chi_{yy} & 0 \\ 0 & 0 & 0 \end{pmatrix} \vec{H}_{HF} \end{aligned} \tag{4.11}$$

the susceptibility matrix elements $\chi_{xx,xy,yy}$ can be processed to

$$\chi_{xx,xy,yy} \approx A_{xx,xy,yy} \cdot \frac{\Delta H(H_{ext} - H_0) + i\Delta H^2}{(H_{ext} - H_0)^2 + \Delta H^2}. \tag{4.12}$$

Here $A_{xx,xy,yy}$ are constants depending on ω_0 and B_0. Furthermore the first part $\propto \frac{\Delta H(H_{ext}-H_0)}{(H_{ext}-H_0)^2+\Delta H^2}$

in equ. 4.12 is proportional to an antisymmetric Lorentz line shape while the second part $\propto \frac{\Delta H^2}{(H_{ext}-H_0)^2+\Delta H^2}$ is proportional to a symmetric Lorentzian [13].

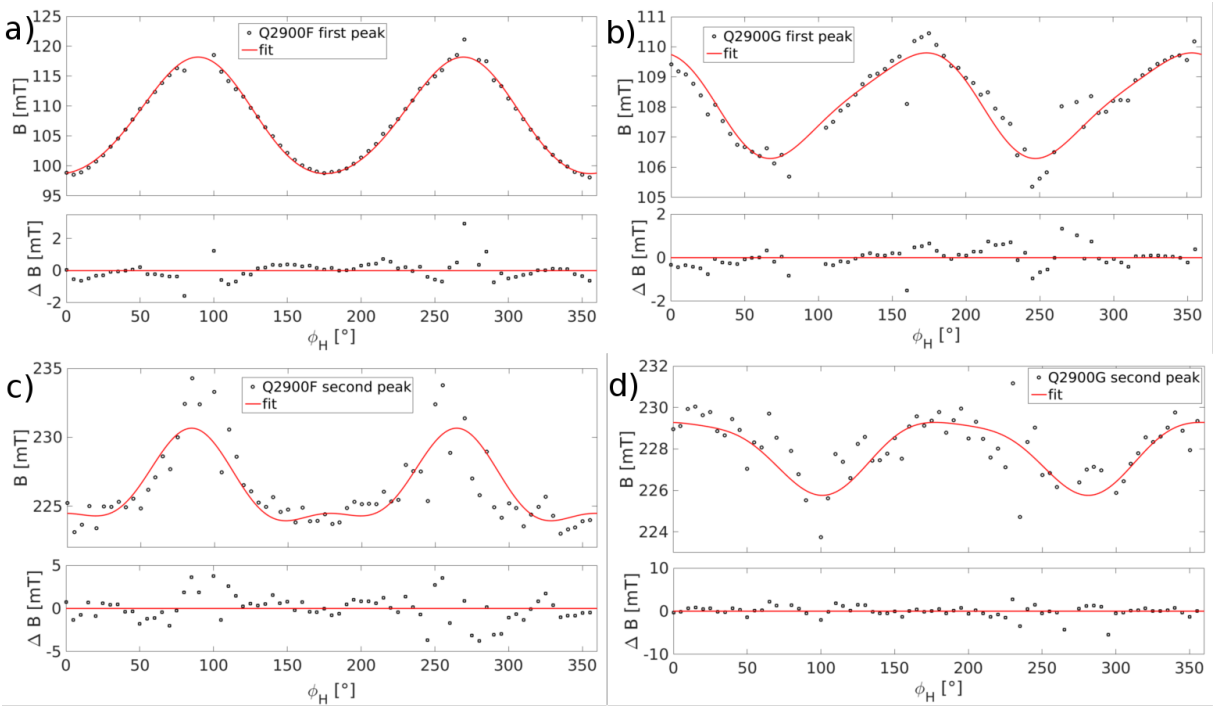

Figure 4.9: Depiction of magnetic anisotropy behavior for the first and second peak of a sample pair sputtered with mounted magnet bars. Q2900F in a) and c) showed expected switching behavior in SQUID while Q2900G (b,d) showed no easy or hard axis. $\Delta B(\Phi_H)$ plots represent the deviation of the fit from the measurement

By changing Φ_H and extracting B_0 from the symmetric fits one can determine the anisotropic behavior of a sample in a $B_0(\Phi_H)$-plot (Fig. 4.9). Q2900F has shown optimal switching behavior in SQUID measurements while Q2900G did not exhibit a typical easy or hard axis (Fig. 4.7a,b). All graphs are fitted to the simple function $F = A\sin^2(\phi-\phi_0) + B\sin^2(2\cdot[\phi-\theta_0]) + C$. The term $\propto \sin^2(2\phi)$ is necessary as the $\Delta B(\Phi_H)$ plot shows a systematic fluctuation without it. The results of the fitting parameters are listed in Table 4.1.

Fig. 4.9a,b show less fluctuations than c) and d). Their shapes behavior is dominated by the term $\propto A\sin^2(\phi)$, which in all four cases can be seen by $\frac{A}{B} \approx 3-10$. Comparing the phases ϕ_0 and θ_0 between Figs. 4.9a,c and b,d reveals a shift of $\phi_{0,2900F} - \phi_{0,2900G} \approx 78°$ for all cases while $\theta_{0,2900F,first} - \theta_{0,2900G,first} \approx 187°$ and $\theta_{0,2900F,second} - \theta_{0,2900G,second} \approx 26°$. Comparing Fig. 4.9a with c one can clearly see that the energetically lowest state can be placed at $\phi_H = 0°$ or $\phi_H = 180°$ as both anisotropy curves favor these positions. On the other hand Fig. 4.9b and d do not exhibit a clear common spot as both minima are shifted. With two non parallel easy axes it is not possible to get a step-like hysteresis behavior. Reminding that the sample is always positioned in a manner that $\vec{B}_{ext}(\phi_H = 0)$ is parallel to the sputtering direction, the presented results point to a clearly shifted easy axes towards edge $\vec{\alpha}$. Due to the low signal of the second peak it is quantitatively hard to argue reliably about a change. Nevertheless the available data

	Q2900F	**Q2900G**
first peak	$\phi_0 = -0.0348$, $\theta_0 = 0.8476$, $A = 0.0194$, $B = 0.0016$, $C = 0.0972$	$\phi_0 = 1.2897$, $\theta_0 = 4.1243$, $A = 0.0033$, $B = 0.0006$, $C = 0.1062$
second peak	$\phi_0 = -0.1184$, $\theta_0 = 0.7034$, $A = 0.0062$, $B = 0.0025$, $C = 0.2220$	$\phi_0 = -1.4146$, $\theta_0 = 0.2355$, $A = 0.0035$, $B = 0.0008$, $C = 0.2257$

Table 4.1: List of fitting parameters according to $F = A\sin^2(\phi - \phi_0) + B\sin^2(2 \cdot [\phi - \theta_0]) + C$ for fits shown in Fig. 4.9.

seem to impose a change from peaks to valleys at $\phi_H \approx 100°$ as well as at $\phi_H \approx 280°$.

Consequently it remains to be noted that it is upmost important to know the correct edge of the sample in order to place a GMR stack on top of a HgTe based TI with CdTe substrate that behaves according to Q2900F. Here the SQUID results together with FMR results exhibit the desired qualities for proper GMR measurements.

4.2.5. Comparison with $Ni_{80}Fe_{20}$ /Cu /$Co_{50}Fe_{50}$ Trilayers on CdTe

In order to support the argumentation that the behavior of the trilayer is not independent of the underlying material, this section addresses the SQUID response of the GMR stack on top of dry etched CdTe (Fig. 4.10). The untreated substrate is bought from *Nikko Metals*. All preparations and measurements are done analogue to sec. 4.2.3. Fig. 4.10a,c show similar results with a clear easy axis along edge $\vec{\alpha}$. Measurements without mounted magnet bars have been repeated several times leading to qualitatively similar results as in Fig. 4.10c. Typically permanent magnets are used to enhance the magnetic anisotropy of a sample leading to a controlled easy axis direction [14]. Thus without them the easy axis develops along energetically lower states which include terms like stray fields and shape anisotropy. The most striking feature of Fig. 4.10b is that the colors of the two graphs changed compared to Fig. 4.10a. It means that $B_{sputter} = 100\,\mathrm{mT}$ is high enough to impose an anisotropy on the CdTe sample which is not the case for a HgTe based sample. A difference between CdTe and HgTe is that HgTe forms surface states with any non-inversed material on top of it. This fact might be part of the answer why $Ni_{80}Fe_{20}$ /Cu /$Co_{50}Fe_{50}$ trilayers show an unexpected behavior on top of HgTe.

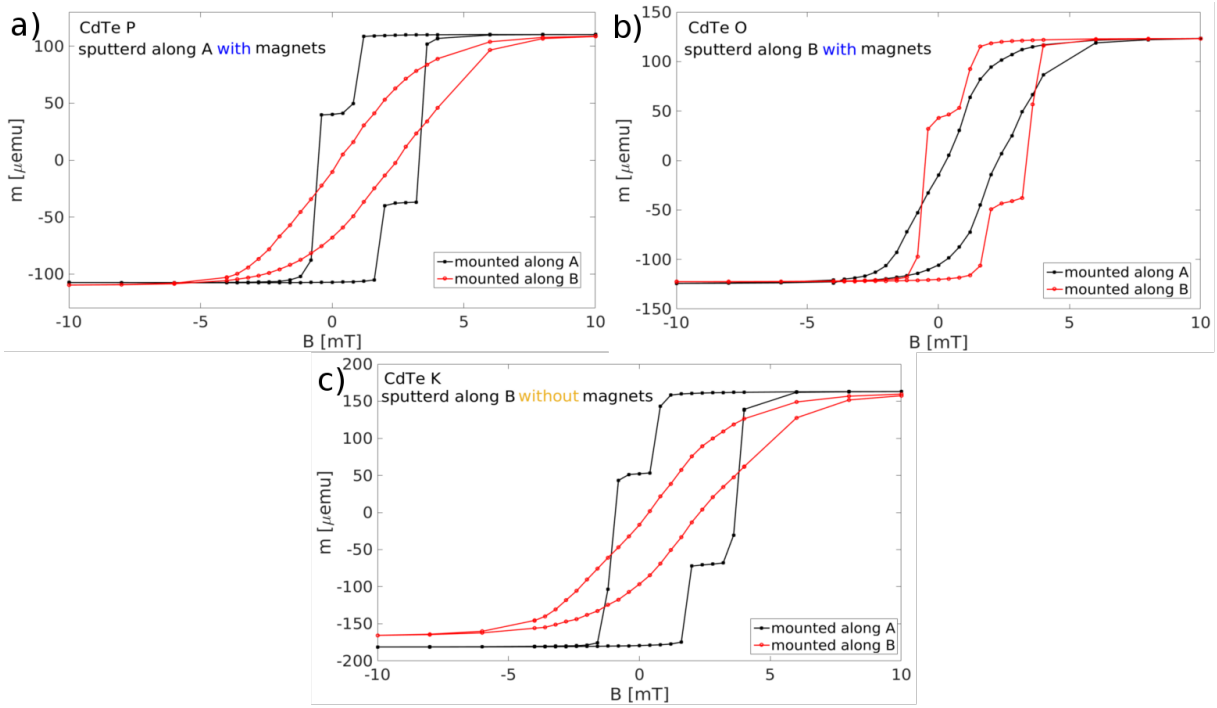

Figure 4.10: Experimental results acquired by SQUID for GMR stack on dry etched CdTe . All samples show expected easy and hard axis behavior. In c), where $\vec{B}_{sputter} = 0$, the easy axis still aligns with edge $\vec{a}$.

4.3. Implementation of the ferromagnetic layer stack in an elliptical nano Structure

4.3.1. Sample Preparation for SQUID Measurements

Having investigated the behavior of the layer stack on $2 \times 2\,\mathrm{mm}^2$ HgTe pieces the focus will now be set on constructing $Ni_{80}Fe_{20}$ /Cu /$Co_{50}Fe_{50}$ trilayers shaped into ellipses of same dimensions as the ones in the SOT-device. By implementing millions of pillars on a $4 \times 4\,\mathrm{mm}^2$ area of etched HgTe it is possible to measure the average sensor behavior via SQUID. Typical sensitivities of SQUIDS lie in the order of $1.0 \cdot 10^{-7}$ emu [15]. Therefore a minimum magnetic moment of $1.0 \cdot 10^{-6}$ emu, which is 10 times the sensitivity, is needed. As the calculated magnetic moment of one pillar is $m_{pillar} = (M_{0,1} \cdot d_1 + M_{0,2} \cdot d_2) \cdot A_{pillar} \approx 2.76 \cdot 10^{-12}$ emu (d_1 and d_2 are the thickness of $Ni_{80}Fe_{20}$ and $Co_{50}Fe_{50}$ respectively) an approximate number of $N = \frac{1.0 \cdot 10^{-6}}{2.76 \cdot 10^{-12}} = 3.6 \cdot 10^5$ pillars is needed. Here $d_1 = d_2 = 10\,\mathrm{nm}$, $M_{0,1} = 800\,\mathrm{kA/m}$, $M_{0,1} = 1500\,\mathrm{kA/m}$ and $A_{pillar} = 0.12\,\mu\mathrm{m}^2$. By putting $2\mu m$ between pillar centers and one additional pillar in the center of a $2 \times 2\,\mu\mathrm{m}^2$ square, a total of $\approx 8 \cdot 10^6$ pillars can be reached, which is one order of magnitude larger than the calculated minimum number of pillars. Lithographically this has to be done by electron-beam-lithography (EBL) leading to scanning electron microscope (SEM) pictures presented in Fig. 4.11. Multiple arrays of $100 \times 100\,\mu\mathrm{m}^2$, which contain thousands of pillars each, had been prepared (Fig. 4.11a). Fig. 4.11b shows an arrangement of multiple pillars inside an array. Bright

spots represent pillars where side walls, which developed during IBE and ALD, could not be removed during lift-off.

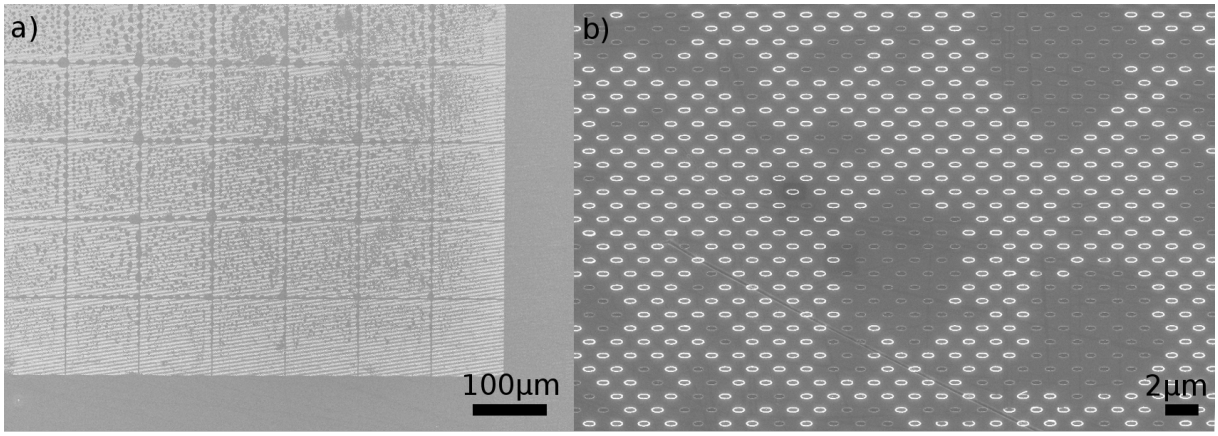

Figure 4.11: SEM pictures of pillar arrays. In a) multiple $100 \times 100\,\mu m^2$ arrays can be seen. In b) the elliptical structure of the pillars is clearly visible. Bright spots represent those sensors where side-walls could not be removed.

4.3.2. SQUID Results

Putting the array of pillars into a SQUID and measuring the magnetic moment results in $m(B)$ curves shown in Fig. 4.12. Fig. 4.12a shows the high magnetic field as well as a zoom into the low-field behavior of the pillar array along easy and hard axis. The application of an offset for the hard axis measurement is needed because the signal would be otherwise too small to measure. Noteworthy is the stepping behavior, which is also present in big sized samples (sec. 4.2.3), with the difference that the step happens before $B_{SQUID} = 0$. This means that both magnetizations couple anti-ferromagnetically, which happens due to the small size of the pillar as well as the small distance between the magnetizations. The difference between the $m(B = 1000\,\mathrm{mT})$ or $m(B = -1000\,\mathrm{mT})$ values of easy and hard axis is less than 10% and could stem from magnetic contamination during orientation change of the sample.

Fig. 4.12b shows a low-field measurement without saturation at higher fields. Additionally a minor loop has been taken in order to emphasize the fact that the anti-parallel magnetization state is indeed a stable magnetic state. The red curve does clearly not follow the same path as before. Furthermore every transition is accompanied by several points, which is expected as the sample contains $N \approx 8 \cdot 10^6$ pillars depicting simply the average behavior of a layer stack. Points at $B \approx -40\,\mathrm{mT}$ or $B \approx 70\,\mathrm{mT}$ are outliers because they are close to $m = 0$ which the SQUID does not handle properly.

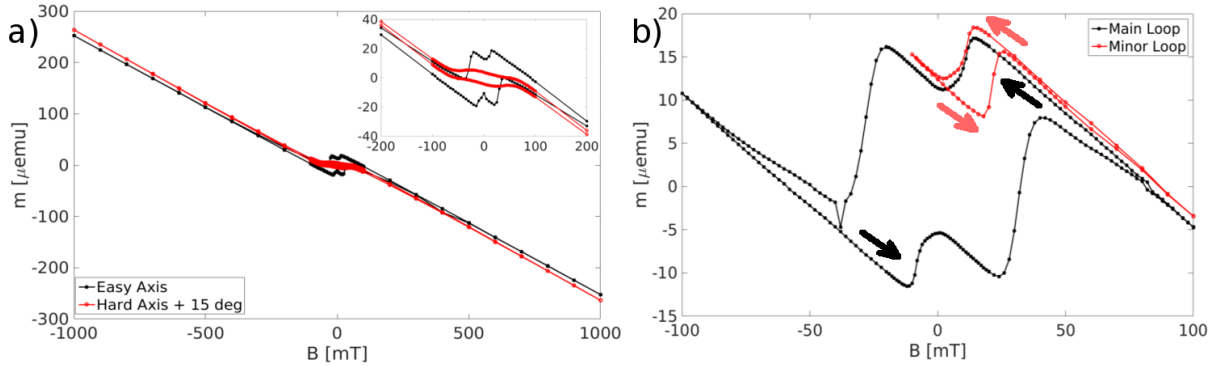

Figure 4.12: SQUID results for an array of ellipse shaped layer stacks on HgTe . a) shows high- and low-field behavior along easy and hard axis. Without an offset along the hard axis the signal in m gets too small. b) Finer low-field behavior without saturation at high fields. The included minor loop puts emphasize on the real anti-parallel state of the sample.

4.4. Summary and Outlook

A $Ni_{80}Fe_{20}$ /Cu /$Co_{50}Fe_{50}$ trilayer stack is the chosen combination of ferromagnetic materials in order to exhibit measurable GMR. This chapter addresses the behavior of such a layer stack on etched HgTe , as this has not been done before. Both SQUID and FMR results show unexpected features for samples that have been magnetron sputtered along the specific crystal direction at edge $\vec{\beta}$. Although a biasing constant magnetic field is used to orient the easy axis direction, those samples do not exhibit any clear easy and hard axis behavior. Only when the guiding fixed magnetic field $\vec{B}_{sputter}$ is parallel to edge $\vec{\alpha}$ SQUID results show optimum step like behavior for parallel and anti-parallel magnetization states. Also FMR measurements yield clear $\propto \sin^2(\phi)$ behavior without higher lying local minima, which can act as trapping states for the magnetization. Thus a good chance for a binary spin-valve GMR behavior can be provided. These FMR results apply mainly to $Co_{50}Fe_{50}$ as it is the FM lying closest to the surface providing higher signals than deeper lying $Ni_{80}Fe_{20}$. An array of elliptical pillars containing $N \approx 8 \cdot 10^6$ sensors is used for examining the average behavior of a nano pillar. SQUID results provide that $Ni_{80}Fe_{20}$ and $Co_{50}Fe_{50}$ couple anti-ferromagnetically and exhibit two distinct magnetic states indicated by a minor loop in the $m(B)$ plot.

Due to the unexpected behavior of the layer stack on top of HgTe it is recommendable to conduct further experiments in order to find a sensible answer. First it should be tested whether a simpler layer stack like $Ni_{80}Fe_{20}$ /Ru or $Ni_{80}Fe_{20}$ /Ta /Ru shows similar behavior in SQUID and FMR. The surface structure of those sputtered surfaces could be further investigated by AFM and SEM. If the crystal structure does not yield clear results it is possible to try measuring the anisotropy of the Gilbert damping factor in FMR. According to *Chen et al.* the Gilbert damping factor α exhibits a magnetic anisotropy in the case of strong spin-orbit interaction of Fe /GaAs [16]. The same kind of interaction is present in Pt or Ta capped half-Heusler material systems where depending on the capping material the orientation of the magnetization

of NiMnSb points either in $(1\bar{1}0)$ or (110) direction [17]. As HgTe is known to exhibit strong spin-orbit interaction it might be possible that the same mechanisms for aligning an adjacent magnetization hold as in the cases described above.

References

[1] D. Jiles, *Introduction to magnetism and magnetic materials* (CRC press, 1991).

[2] J. M. Coey, *Magnetism and magnetic materials* (Cambridge university press, 2010).

[3] T. L. Gilbert, *A phenomenological theory of damping in ferromagnetic materials,* IEEE transactions on magnetics **40**, 3443 (2004).

[4] S. Rezende, C. Chesman, M. Lucena, A. Azevedo, F. De Aguiar, and S. Parkin, *Studies of coupled metallic magnetic thin-film trilayers,* Journal of Applied Physics **84**, 958 (1998).

[5] M. Getzlaff, *Fundamentals of magnetism* (Springer Science & Business Media, 2007).

[6] B. Aktas, L. Tagirov, and F. Mikailov, *Magnetic nanostructures*, Vol. 94 (Springer Science & Business Media, 2007).

[7] M. Sawicki, W. Stefanowicz, and A. Ney, *Sensitive squid magnetometry for studying nanomagnetism,* Semiconductor Science and Technology **26**, 064006 (2011).

[8] C. P. Wen, *Coplanar waveguide: A surface strip transmission line suitable for nonreciprocal gyromagnetic device applications,* IEEE Transactions on Microwave Theory and Techniques **17**, 1087 (1969).

[9] M. A. Makeev, R. Cuerno, and A.-L. Barabasi, *Morphology of ion-sputtered surfaces,* Nuclear Instruments and Methods in Physics Research Section B: Beam Interactions with Materials and Atoms **197**, 185 (2002).

[10] C. Marrows and B. Hickey, *Impurity scattering from δ-layers in giant magnetoresistance systems,* Physical Review B **63**, 220405 (2001).

[11] H. Over, Y. He, A. Farkas, G. Mellau, C. Korte, M. Knapp, M. Chandhok, and M. Fang, *Long-term stability of ru-based protection layers in extreme ultraviolet lithography: A surface science approach,* Journal of Vacuum Science & Technology B: Microelectronics and Nanometer Structures Processing, Measurement, and Phenomena **25**, 1123 (2007).

[12] T. Leeb, M. Brockmann, F. Bensch, S. Miethaner, and G. Bayreuther, *In-plane magnetic anisotropies in fe films on vicinal ag (001) and au (001) surfaces,* Journal of applied physics **85**, 4964 (1999).

[13] N. Mecking, Y. Gui, and C.-M. Hu, *Microwave photovoltage and photoresistance effects in ferromagnetic microstrips,* Physical Review B **76**, 224430 (2007).

[14] M. Schilling and C. Ras, *Magnet designs for magneto-electronic thin film processing,* Magnetics Business & Technology (2003).

[15] M. Buchner, K. Höfler, B. Henne, V. Ney, and A. Ney, *Tutorial: Basic principles, limits of detection, and pitfalls of highly sensitive squid magnetometry for nanomagnetism and spintronics,* Journal of Applied Physics **124**, 161101 (2018).

[16] L. Chen, S. Mankovsky, S. Wimmer, M. Schoen, H. Körner, M. Kronseder, D. Schuh, D. Bougeard, H. Ebert, D. Weiss, *et al.*, *Emergence of anisotropic gilbert damping in ultrathin fe layers on gaas (001),* Nature Physics **14**, 490 (2018).

[17] F. Gerhard, M. Baussenwein, L. Scheffler, J. Kleinlein, C. Gould, and L. Molenkamp, *Engineering the magnetic anisotropy axes in epitaxial half-heusler nimnsb by pt and ta capping,* Applied Physics Letters **111**, 172402 (2017).

5

Observation of current induced Spin-Orbit Torques in a 3D HgTe based nano Device

The research field of spintronics deals with possibilities to exploit the electron spin, in contrast to electron charge, as the driving force for changes in microelectronic devices [1]. Lower power consumption and, at the same time, a higher information transfer rate are two of the main potential advantages of spin driven devices. Bit states in magnetic random access memories (MRAMs) are used to store data and can be changed by spin-polarized currents. One method is known as spin-transfer torque (STT) where a charge current passes a magnetic tunnel junction (MTJ), consisting of a free and fixed ferromagnetic layer, in order to switch, depending on current direction, the free layer [2]. Unfortunately too high currents could cause damages on the oxide layer in this geometry leading to low endurance and unreliability. These problems can be resolved with the help of spin-orbit torques (SOT) [3]. In the SOT geometry a charge current generates a spin current or a spin accumulation that subsequently interacts with an adjacent magnetic layer. Only a small read current has to flow through the magnetic layer stack and therefore no heating damage can occur [4]. Further optimization can be implemented by reducing a three-terminal geometry to a two-terminal which leads to a higher bit density and therefore higher storage capacitance [5]. This constitutes only a minor change compared to the chance to reduce power consumption even further by implementing the right material. The best choice for this matter are topological insulators (TIs) as they offer two dimensional surface states with spin and momentum locked in a helical manner (sec. 2.2). Among the variety of TIs it is HgTe that exhibits reliably an insulating state in its bulk while providing conducting surface states (sec. 2.1) with charge-to-spin conversion rates higher than in any other material system [6].

This chapter describes all necessary steps in order to build a nano device consisting of a

nano pillar which is separated by a thin oxide barrier from a dry etched HgTe surface that is shaped into a 2 μm wide current channel. Furthermore the measurement principles for the giant magnetoresistance (GMR) measurements of the pillar will be addressed as its resistance state is going to be monitored during the whole time of the DC current sweep that switches the adjacent magnetization. Experimental results as well as parasitic effects, like the influence of the generated Oersted field, will also be discussed.

5.1. Preliminary Considerations

5.1.1. Spin-orbit Torque Generation on HgTe /$Cd_{0.68}Hg_{0.32}Te$ Heterostructures

From sec. 2.3 we know that a current density $\vec{j}(y)$ at the surface of a 3D TI generates a spin accumulation $\vec{S}(x)$ where the direction of the spin depends on the helicity of the surface states. This spin subsequently couples to the adjacent magnetization $\vec{M}$ via exchange interaction $\propto -J_{ex} \cdot \vec{M}\vec{S}$, where J_{ex} is the exchange interaction constant [7]. Thus during each scattering event of a conducting electron the generated spin accumulation transfers a torque on $\vec{M}$, provided that $\vec{M}$ is not too far away [3].

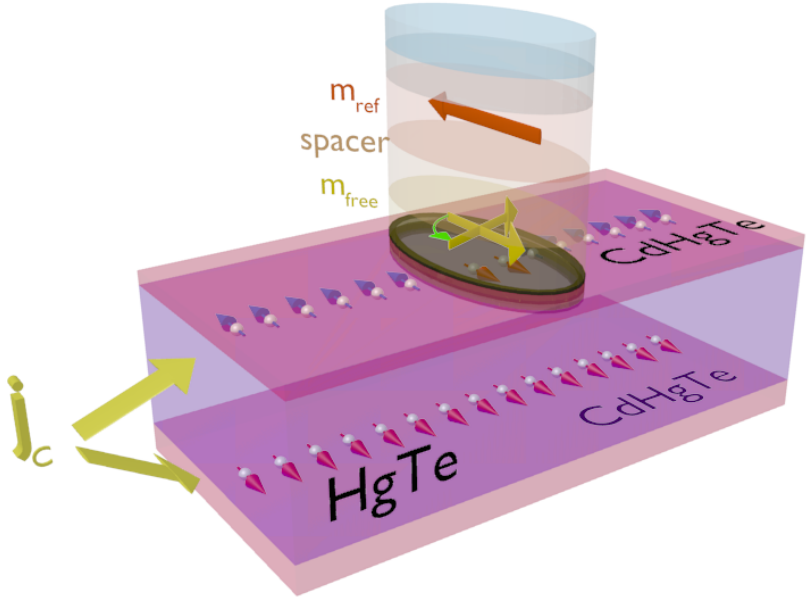

Figure 5.1: Effect of current induced SOT on an adjacent magnetic moment $\vec{m}_{free}$. The ferromagnetic GMR stack is separated by a thin ZrO_2 barrier from the dry etched HgTe surface. Spins pointing in $-x$ direction (blue) turn into spins pointing in x direction (red) as soon as they transfer a torque on $\vec{m}_{free}$. A high enough $\vec{j}_c$ could finally switch the magnetization.

Figure 5.1 shows the effect of a current induced SOT on an adjacent magnetic moment $\vec{m}_{free}$. The full $Ni_{80}Fe_{20}$ /Cu /$Co_{50}Fe_{50}$ /Ta /Ru GMR stack, indicated by the elliptical layers, is separated by a thin ZrO_2 layer from the dry etched HgTe surface. It can be seen that a current density $\vec{j}_c$ generates a spin polarization at the top and bottom surface of the $Cd_{0.68}Hg_{0.32}Te$ /HgTe /$Cd_{0.68}Hg_{0.32}Te$ heterostructure. The top electronic states (blue) interact with $\vec{m}_{free}$, as soon as they are close to each other (below the pillar), by transferring a torque. In this process $\vec{m}_{free}$ acts on these electrons so that their spin points into $+x$ direction (red). Due to spin orbit coupling those electrons gain again their original spin polarization which they can subsequently transfer again to $\vec{m}_{free}$ leading to multiple hits and therefore higher efficiencies than in the case of STT.

In sec. 4.1.1 the LLG equation shows the dynamics of a magnetization $\vec{M}$ in an external magnetic field $\vec{B}_{ext}$ (equ. 4.2). In 1996 Slonczewski introduced an additional term to the equation, which consequently governs current induced torques as well [8]. With definition of the magnetization unit vector $\vec{\hat{m}} = \frac{\vec{M}}{M_s}$ the Lnadau-Lifschitz-Gilbert-Slonczewski (LLGS) equation reads

$$\frac{d\vec{\hat{m}}}{dt} = -\gamma\vec{\hat{m}} \times \vec{B}_{ext} + \alpha\vec{\hat{m}} \times \frac{d\vec{\hat{m}}}{dt} + \frac{\gamma}{M_s}\vec{T}, \tag{5.1}$$

where $\vec{T}$ is the term representing the current induced torques in $\mathrm{J/m^3}$ and M_s is the saturation magnetization in A/m [9]. These torques are in general perpendicular to the magnetization and can be expressed as

$$\vec{T} = \tau_{FL}\vec{\hat{m}} \times \vec{S} + \tau_{DL}\vec{\hat{m}} \times \left(\vec{\hat{m}} \times \vec{S}\right). \tag{5.2}$$

In the case of TIs $\vec{T}$ has a special dependence on $\hat{m}_z$ of the form

$$\vec{T} = \tau_{FL}\vec{\hat{m}} \times \left(\vec{\hat{z}} \times e\vec{E}\right) + \tau_{DL}\hat{m}_z\vec{\hat{m}} \times e\vec{E}, \tag{5.3}$$

where τ_{FL} and τ_{DL} represent the field-like and damping-like component respectively and $\vec{E}$ is the applied electric field [10]. According to equ. 5.3 the second term vanishes as soon as the magnetization lies in the sample plane ($\hat{m}_z = 0$) leading to a pure field-like behavior of the torque. In this case the first term of equ. 5.1 can be modified to an effective magnetic field with reduced or enhanced magnitude depending on the direction of the current. Thus the current induced torque contributes to the switching by changing the frequency of the precession and subsequently modifying the damping, which depends on the Gilbert-damping factor α. In the case of $\hat{m}_z = 1$ both terms in equ. 5.3 contribute to the switching. Here the second term is independent of the Gilbert-damping factor so that, under certain conditions, the switching could be enhanced.

According to equ. 5.2 one can define two effective magnetic fields $\vec{B}_{FL,DL}$ that can subsequently be compared to other magnetic fields during experiments. Here the torques would be defined as $\vec{T}_{FL,DL} = \vec{M} \times \vec{B}_{FL,DL}$. As an example the fields $\vec{B}_{FL,DL}$ would be defined as $\vec{B}_{FL} = B_{FL}\vec{\hat{x}}$ and $\vec{B}_{DL} = B_{DL}\left(\vec{m} \times \vec{\hat{x}}\right)$ for $\vec{S} \parallel \vec{\hat{z}} \times \vec{E} \parallel \vec{\hat{x}}$. Switching occurs at a specific magnetic field $B_{ext,0}$. As values of B_{FL} lie usually in the range of a few Oersted one can probe B_{FL} only in the vicinity of $B_{ext,0}$. Thus it is reasonable to define $\Delta B = B_{ext} - B_{ext,0}$ as a parameter. As discussed above in our case $B_{DL} = 0$, so that only $B_{FL} \neq 0$ remains as the driving force to switch the magnetization m. The impact of all present effective fields can be seen in Fig. 5.2. The magnetization precesses around ΔB (red arrow) according to LLG (equ. 4.2). Both ΔB and B_{FL} (blue arrow) exert a torque of the form $T_\Delta = m \times \Delta B$ (cyan arrow) and $T_{FL} = m \times B_{FL}$ (green arrow) on the magnetization m, respectively. This in turn changes the direction of m implying a dm/dt with a resulting force $m \times dm/dt$. With rising current B_{FL} grows in opposite

direction to ΔB. As soon as $\Delta B < B_{FL}$ it follows $T_\Delta < T_{FL}$ and consequently $m \times dm/dt$ starts to point away from ΔB leading to switching of m.

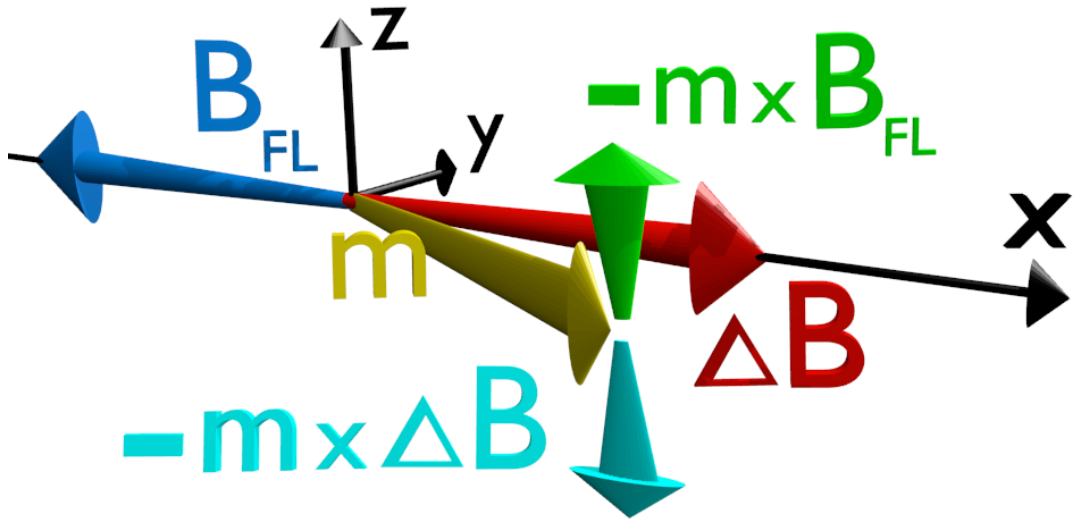

Figure 5.2: Schematic representation of all effective magnetic fields which are involved in the reorientation process of the magnetization m. In general m precesses around ΔB according to LLG. With rising current also B_{FL} grows in the opposite direction than ΔB resulting in a bigger change $m \times B_{FL}$ than $m \times \Delta B$ as soon as $B_{FL} > \Delta B$. Consequently the magnetization switches according to LLG.

5.1.2. Giant Magnetoresistance

Chapter 4 introduces a ferromagnetic layer stack consisting of $Ni_{80}Fe_{20}$ /Cu /$Co_{50}Fe_{50}$. As $Ni_{80}Fe_{20}$ has a different coercivity than $Co_{50}Fe_{50}$ the layer stack can exhibit two distinct magnetic states, parallel and anti-parallel. The measurable quantity that results from pushing a current in the plane of the layer stack is a resistance R_{GMR} that can be explained in the context of the Mott model [11]. There are mainly two ideas proposed in this model. Firstly the conducting channel of a ferromagnet can be separated into two channels (spin-up and spin-down) being in parallel. Secondly the resistances of the two channels are different due to non-equal scattering rates of spin-up and spin-down electrons [12]. In a current perpendicular to plane geometry the total resistance can be modeled by the replacement circuit diagram in Fig. 5.3.

The equivalent circuits of Fig. 5.3 are also valid for current in plane configurations where the current flows along the surface plane, just like in the case of the SOT-device. Calculating R_{GMR} within the circuit diagrams of Fig. 5.3 leads to higher resistance in the anti-parallel case ($R_{GMR,AP} > R_{GMR,P}$) which is also the case for the layer stack in our device. The total GMR is thus defined as

$$GMR = \frac{R_{GMR,AP} - R_{GMR,P}}{R_{GMR,P}} = \frac{\Delta R}{R}. \tag{5.4}$$

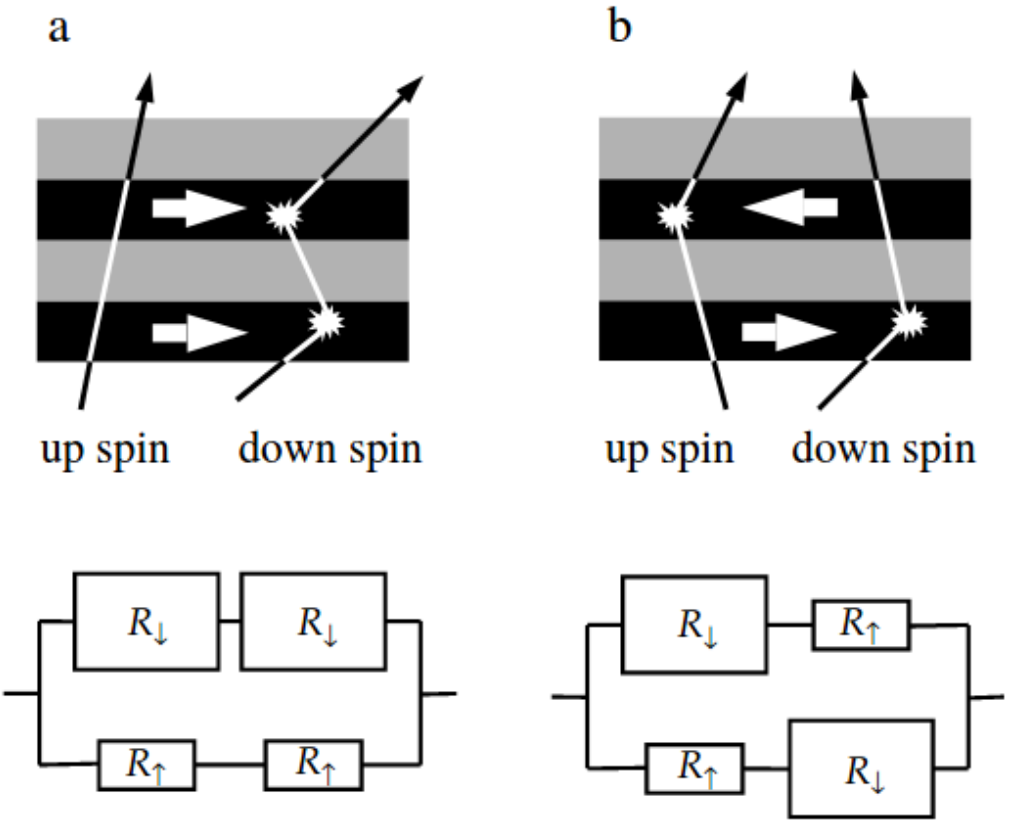

Figure 5.3: Schematic illustration of electrons trans passing a multilayer stack consisting of FM and non-FM materials. In a) the parallel case leads, according to the replacement circuit below, to a lower total resistance than in the anti-parallel case b). Picture is adopted from [12].

5.2. Description of the nano Device

5.2.1. Geometric Design

Analogous to sec. 3.2.1 the geometry for the SOT-device has to be defined beforehand. Fig. 5.4 shows the final geometric design for devices used to investigate current induced SOT efficiencies on top of 3D HgTe heterostructures. Contacts 1 and 8 define the $2 \times 40\,\mu\text{m}^2$ DC current channel. The Hall probes (2,14) and (9,7) are $30\,\mu$m apart and allow for measurements of V_{xy} and V_{xx} in order to extract carrier density n and mobility μ. Furthermore V_{xx} can be used to verify the expected behavior of the TI strip during DC current operation. The nano pillars exhibit a nominal area of $600 \times 200\,\text{nm}^2$ and have an elliptical shape in order to stabilize the easy axis due to shape anisotropy. The layer stack of the pillars is given in the inset and is the same as the one investigated in ch. 4. There are four V-shaped contact pairs which are shorted at the site of the nano pillar. The contacting area on the pillar site is $\approx 100\,$nm in diameter. Two V-shaped contact pairs are only connected by the surface of a pillar. This geometry allows for pseudo four

terminal measurements of the GMR signal with higher signal-to-noise ratio than in two terminal configuration.

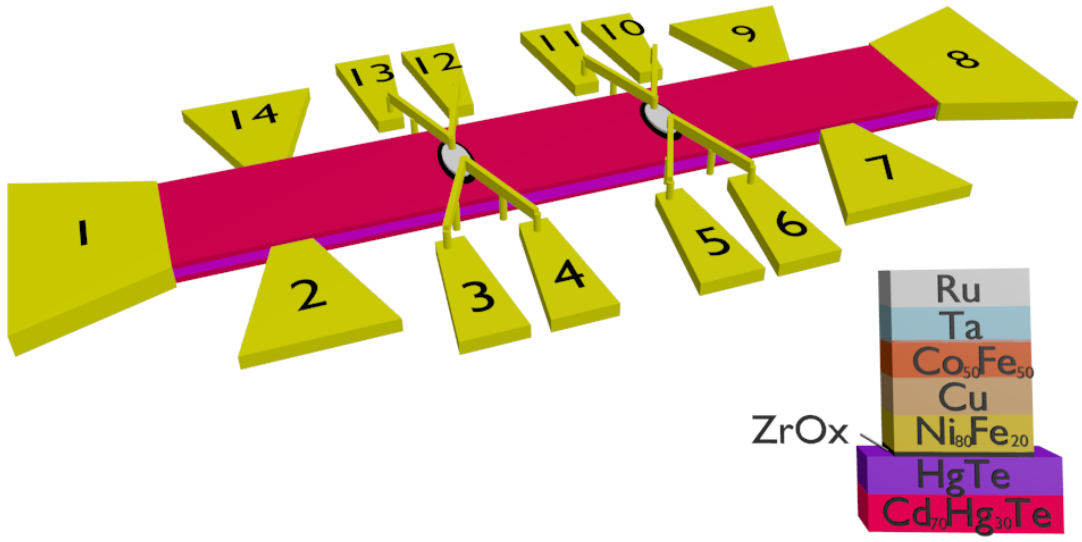

Figure 5.4: Representation of the device geometry of the final SOT device. Two ellipse shaped nano pillars, which are deposited on etched HgTe , form the sensors used for investigations of SOT efficiencies.

5.2.2. Lithography Process

Due to the small sizes of mesa and pillars this process has to be executed by electron-beam lithography (EBL). Fig. 5.5 gives a short overview of all necessary EBL steps. First the sample needs outer and inner orientation marks in order to secure precise alignment of all further steps (Fig. 5.5a,b). Then the nano pillars get defined and the $Cd_{0.68}Hg_{0.32}Te$ cap at those sites dry etched, filled with ZrO_2 via ALD and with the GMR stack by sputtering (Fig. 5.5c). After dry etching the mesa the inner contacts get deposited followed by the outer contacts that were prepared by optical lithography (Fig. 5.5d,e,f). Finally the air bridges are defined by EBL in a modified standard process [13]. A precise description of the recipe is given in appendix B.

Fig. 5.6 shows SEM pictures of the final device. In a) one can see the central structure consisting of two nano pillars and the dominant V-shaped air-bridges. Fig. 5.6b) shows a close image of an air-bridge. The DC current channel, pillar and supporting posts are clearly visible. The smallest area is located on the pillar site ($\approx 100\,\mathrm{nm}$ diameter) where the two shorted contacts are connected.

5.2.3. Evaluation of Biot-Savart Fields

One of the main concerns of this experiment is a non-negligible contribution of an Oersted field (Biot-Savart field). Those fields are generated by a current and independent of the material in use. The most general form of the Biot-Savart law reads

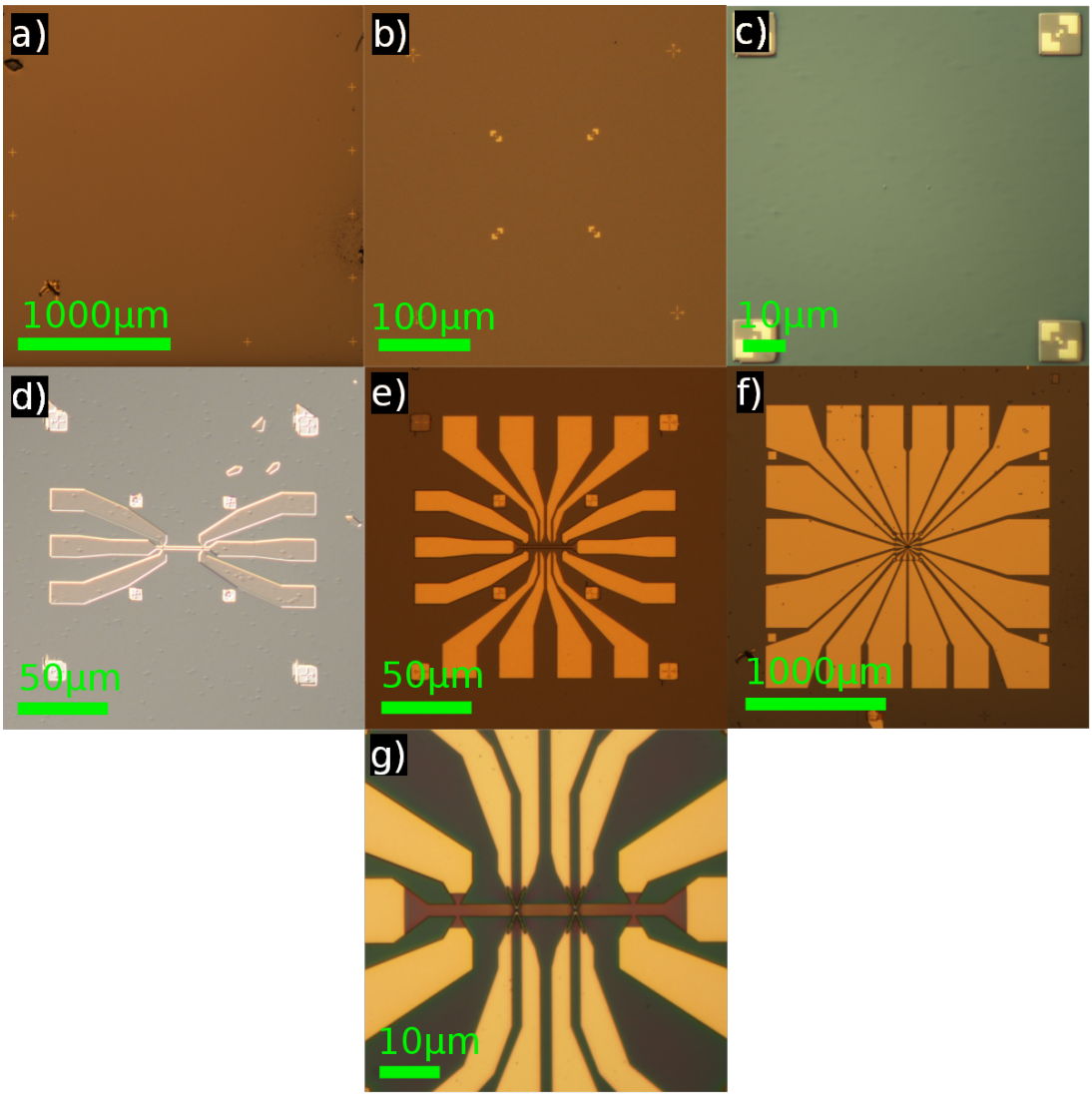

Figure 5.5: Microscope pictures of all lithographic steps for an SOT device. After the placement of outer (a) and inner (b) crosses for precise alignment the nano pillars are sputtered (c). Subsequently the mesa (d) is formed by dry etching and inner (e) contacts are deposited. Outer contacts (f) are prepared by optical lithography. Finally the air bridges (g) are deposited in order to contact the $600 \times 200\,\mathrm{nm}^2$ pillars.

$$d\vec{B} = \frac{\mu_0 I}{4\pi r^2} d\vec{l} \times \frac{\vec{r}}{r}, \tag{5.5}$$

where μ_0 is the vacuum permeability, I is the current running through an elemental length $d\vec{l}$ and r is the radial distance from $d\vec{l}$ to the point of magnetic contribution $d\vec{B}$. With equ. 5.5 the field at the perpendicular distance a from a long circular conductor can be calculated by $B = \mu_0 I/2\pi a$. This result can also be derived from Ampére's law $\oint \vec{B} d\vec{s} = \mu_0 I$ with $d\vec{s}$ being a circle outside a circular wire. In the case of an infinite rectangular wire with width w and height h the total magnetic field becomes $B = \mu_0 I/2 \cdot (w + h)$. As the cross-section of our current channel exhibits a rectangular shape with $w = 2\,\mu\mathrm{m}$ and $h = 0.08\,\mu\mathrm{m}$ the magnetic field 10 nm

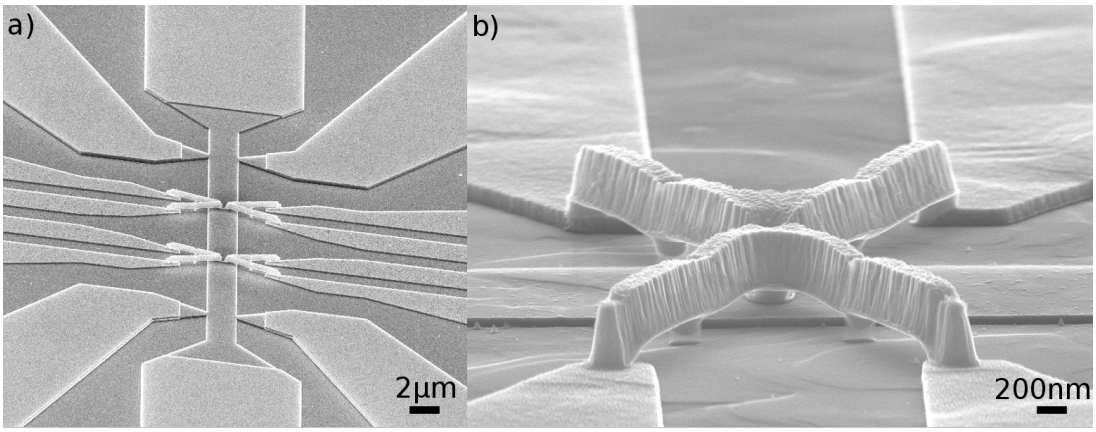

Figure 5.6: SEM pictures of the SOT device. In a) the main structure consisting of two pillars, mesa, air-bridges and contacts can be seen. b) shows a close up of the air-bridge.

above the surface calculates to $B = 1.197\,\mathrm{Oe}$.

Now it is also possible to evaluate an expression for the magnetic field of an infinite plane which can be modeled as multiple long circular conductors being placed next to each other (Fig. 5.7a). The distance between the conductors is chosen to be dx. We are only interested in $dB \cdot \cos(\theta)$ as the *z components* of dB average to zero when integrating over the full width. According to the inset of Fig. 5.7 one can evaluate the relation between dx and $d\theta$ as $rd\theta/\cos(\theta)$ leading to a total field of

$$\begin{aligned}\vec{B} &= \int_{-\pi/2}^{\pi/2} \frac{\mu_0 K \cdot dx \cdot \cos(\theta)}{2\pi r} \\ &= \int_{-\pi/2}^{\pi/2} \frac{\mu_0 K \cdot \cos(\theta)}{2\pi r} \cdot r \frac{d\theta}{\cos(\theta)} \\ &= \frac{\mu_0 K}{2\pi} \int_{-\pi/2}^{\pi/2} d\theta \\ &= \frac{\mu_0 K}{2},\end{aligned} \tag{5.6}$$

where K denotes the current surface density in A/m. For a current of $I = 400\,\mu\mathrm{A}$ and a channel width of $2\,\mu\mathrm{m}$ one gets an Oersted field of $B = 1.257 \cdot 10^{-4}\,\mathrm{T} = 1.257\,\mathrm{Oe}$. In case of our device one can model the TI as two separated conducting planes where the current is equally distributed. Consequently the full Oersted field at the adjacent FM would be $B = B_{top} + B_{bottom} = 2 \cdot \frac{\mu_0 K/2}{2} = \frac{\mu_0 K}{2}$ which would result in the same value calculated above.

The assumptions above are only valid for the case that the topological surface states' probability is zero in the bulk and non-zero at the surface. Truth is that the probability density of edge states can reach up to $\zeta \approx 10\,\mathrm{nm}$ into the bulk [14]. It is therefore reasonable to calculate the Oersted field for two 10 nm thick surfaces which are 70 nm separated from each other (thickness of HgTe). For this purpose a model has to be implemented where a $2\,\mu\mathrm{m} \times 2\,\mu\mathrm{m} \times 10\,\mathrm{nm}$ volume

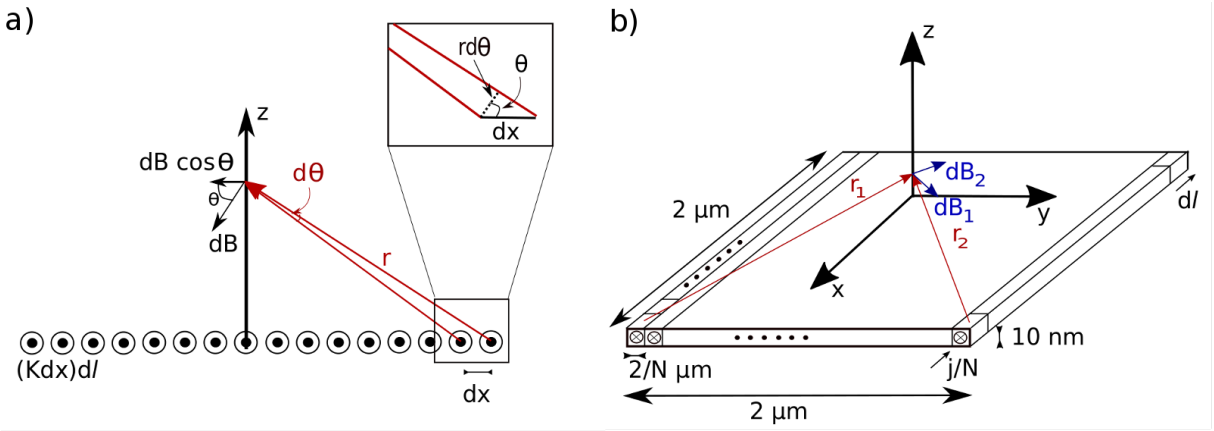

Figure 5.7: Model for calculating the Biot-Savart field of an infinite plane and a thin volume. In a) multiple long conductors, each carrying a current $K \cdot dx$ (pointing out of the paper plane), are placed next to each other. The contribution of each conductor is given by $B = \mu_0 I/2\pi r$. In b) the volume is divided in multiple elemental volumes of length dl, each carrying a current density j/N. As an example two contributions to the total field are depicted

5

is separated into small elements of $\Delta x = \Delta y = \frac{2\,\mu\text{m}}{N}$ and $\Delta z = 10\,\text{nm}$ (Fig. 5.7b). The adjacent FM has a thickness of 10 nm. That means the distance in z-direction between the center of the FM and the centers of any elemental volume is 10 nm. By taking $I = N \cdot I_0$, $N = 2000$ and $d\vec{l} = dl \cdot \hat{\vec{x}} = 1 \cdot 10^{-9}\hat{\vec{x}}$ into equ. 5.5 one gets

$$
\begin{aligned}
\vec{B} &= \int \frac{\mu_0 I_0}{4\pi r^3} \cdot d\vec{l} \times \vec{r} \\
&\approx \frac{\mu_0 I_0}{4\pi} \sum_{n,m=-1000}^{1000} \frac{1}{(x_n^2 + y_m^2 + \Delta z^2)^{3/2}} \begin{pmatrix} dl \\ 0 \\ 0 \end{pmatrix} \times \begin{pmatrix} x_n \\ y_m \\ \Delta z \end{pmatrix} \\
&= \frac{\mu_0 I_0}{4\pi} \sum_{n,m=-1000}^{1000} \frac{1}{(x_n^2 + y_m^2 + 100 \cdot 10^{-18})^{3/2}} \begin{pmatrix} 1 \cdot 10^{-9} \\ 0 \\ 0 \end{pmatrix} \times \begin{pmatrix} x_n \\ y_m \\ 10 \cdot 10^{-9} \end{pmatrix} \\
&= \frac{\mu_0 I_0}{4\pi} \sum_{n,m=-1000}^{1000} \frac{1}{(x_n^2 + y_m^2 + 100 \cdot 10^{-18})^{3/2}} \begin{pmatrix} 0 \\ -10 \cdot 10^{-18} \\ y_m \cdot 10^{-9} \end{pmatrix}.
\end{aligned}
\tag{5.7}
$$

In above equ. 5.7 $x_n = n \cdot \Delta x$ and $y_m = m \cdot \Delta y$ with $\Delta x, \Delta y = 1 \cdot 10^{-9}$. Evaluating the value of the Biot-Savart field of two 70 nm distanced planes, each of thickness $d = 10\,\text{nm}$, numerically results in a lateral Oersted field of $B_{Oe} \approx 1.200\,\text{Oe}$ for $I = 400\,\mu\text{A}$. This value differs less than 5% from the value calculated for two conducting planes. Due to symmetric summation of equ. 5.7 the perpendicular component of the resulting Biot-Savart field is $B_z = 0$.

Lastly it is also possible to assume full bulk contribution so that the current is distributed through the whole volume of the current channel. In this case the volume has to be additionally

Model	B [Oe]
infinite long rectangular wire	1.197
infinite planes	1.257
two thin volume planes	1.200
full volume	1.215

Table 5.1: List of resulting magnetic fields B depending on the chosen model of the current path

divided into u elements in the z direction. Thus Δz from equ. 5.7 becomes $z_u = u \cdot \Delta z + 10\,\text{nm}$ with $\Delta z = \Delta x = \Delta y = 1 \cdot 10^{-9}$ with an additional sum over u. Calculating the magnetic field in this approach results in $B \approx 1.215\,\text{Oe}$.

Table 5.1 summarizes the resulting magnetic fields of all four assumptions. Thus independent of the chosen model, the resulting Biot-Savart field remains $B_{Oe} \approx 1.2\,\text{Oe}$ for $400\,\mu\text{A}$ in our geometry. In section 5.3 experimentally measured current induced magnetic fields will show at least three times higher values than the calculated Oersted field.

5.3. Experimental Results

5.3.1. Measurement Procedure

The measurement procedures for all samples can be described according to Fig. 5.8. An AC current with a fixed amplitude and frequency is pushed in the plane of the nano pillar resulting in a voltage response V_{AC} that is used to calculate R_{GMR} with the help of a reference resistor. The AC current generation and R_{GMR} calculation is done by a resistance bridge. It generates an AC current on a secondary circuit, which is connected to the measurement circuit by a balance transformer with an adjustable reference resistor. Subsequently R_{GMR} is calculated via Ohm's law. The advantage of such a setup is the high signal-to-noise ratio as well as its high thermal stability. For switching measurements a DC current is pushed through the surface of the TI. The DC current source is connected to the common ground by a high resistance ($\approx 10\,\text{M}\Omega$) so that the current path on the TI is practically disconnected from the current path along the nano pillar. A constant magnetic field B_{ext} is used as a supporting field for controlled switching. Its orientation can be adjusted in the full sample plane.

Before the first measurements can be taken the direction of B_{ext} has to be adjusted to the long axis of the nano pillar as this leads to binary switching behavior of the GMR stack. This can be easily done by sweeping from high to low fields while the direction of B_{ext} gets stepped. Sweeping from high B_{ext} the $R_{GMR} = R_{GMR,P}$ becomes $R_{GMR} = R_{GMR,AP}$ after passing a certain $B_{ext,0} \neq 0$. This is the magnetic field where $Ni_{80}Fe_{20}$, which is the free layer and closest FM to the TI, switches. In order to see current induced SOT switching it is necessary to set B_{ext} $\approx 0.5\,\text{Oe}$ away from $B_{ext,0}$ before the switch and subsequently sweep I_{dc} of the DC current source. The reading of the current source is accurate as it was tested against a known resistance put in series with the sample. Depending on the helicity as well as the exchange constant between spin

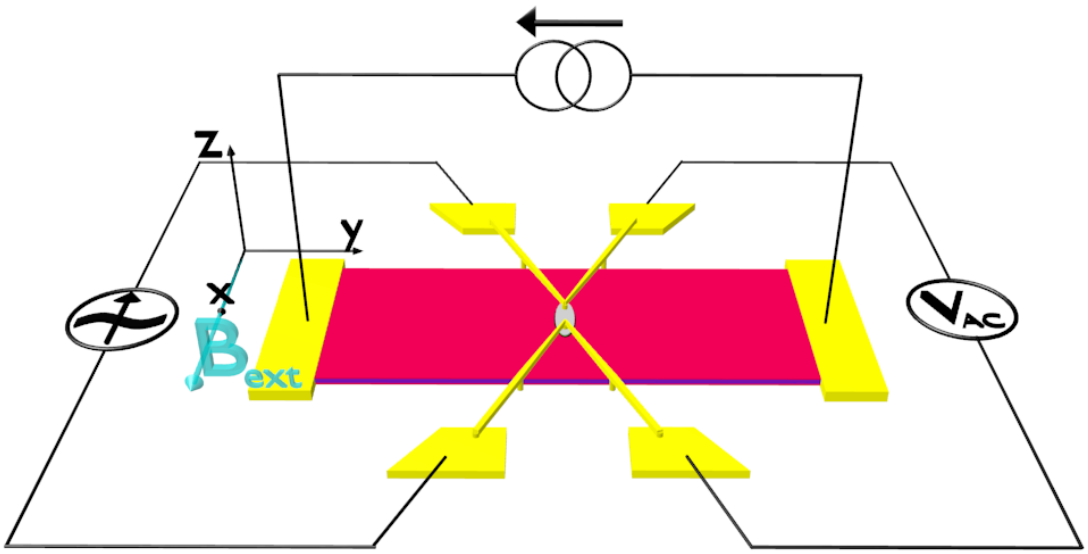

Figure 5.8: Schematic description of the measurement procedure for SOT devices. The GMR is measured by applying an AC current of fixed amplitude and frequency on the surface of the nano pillar while the AC voltage response together with a reference resistor is used to calculate R_{GMR}. Simultaneously a DC current is pushed through the TI. An external magnetic field B_{ext} is constantly applied in the sample plane in order to support the controlled switching of the adjacent ferromagnetic layer.

accumulation and magnetization the switch will occur either at $+I_{dc}$ or $-I_{dc}$. The current density j_c is calculated for an area of $A = 2 \cdot 2\,\mu\text{m} \cdot 10\,\text{nm}$ where $2\,\mu$m is the width of the current channel, the 10 nm is the penetration depth of the edge state into the bulk and the 2 accommodates for the 2 surfaces of the TI. For measurements of the SOT efficiencies the above steps have to be repeated with increased B_{ext} so that one gains a $B(I)$ chart from which a $\Delta B/j$ can be deduced. Here $\Delta B = B_{ext} - B_{ext,0}$ and $j = I_{dc}/A$ is the current density.

5.3.2. GMR of a nano Pillar

One of the first things that need to be checked, when a new SOT device sample is measured, is the functionality of the sensor. The highest GMR accompanied with an instant and irreversible R_{GMR} change can be achieved when B_{ext} is parallel to the long axis of the nano pillar. As the elliptical $Ni_{80}Fe_{20}$ /Cu /$Co_{50}Fe_{50}$ layer stack has its easy axis along the major axis a B_{ext} pointing opposite to $\vec{M}_{Py}$ changes its energetic landscape in such a way that $\vec{M}_{Py}$ holds its direction for as much B_{ext} as it can (sec. 4.1.2). Only when the difference between parallel and anti-parallel states is bigger than the domain nucleation wall energy ϵ the magnetization $\vec{M}_{Py}$ switches leading to an instant change in R_{GMR}. As described in the previous section 5.3.1 the direction of B_{ext} has to be stepped while its magnitude is swept from high to low fields. Fig. 5.9 shows a surface plot of R_{GMR} depending on B_{ext} and ϕ, which is the angle between B_{ext} and the x axis of the cryostat magnet. The most dominant features are the cyan colored maximas, which are $\approx 180°$ apart, representing the hard axis of the GMR stack at $\phi = 50°$ and $\phi = 240°$.

As a consequence the easy axis is supposed to lie at $\phi \approx 140°$ which corresponds to the *correct* orientation of the sample stick, provided that the pillar orientation relative to the cryostat x-axis is known. After comparing all graphs in the vicinity of $\phi = 140°$ the direction of $\phi = 135°$ is chosen as it yields a better switching behavior.

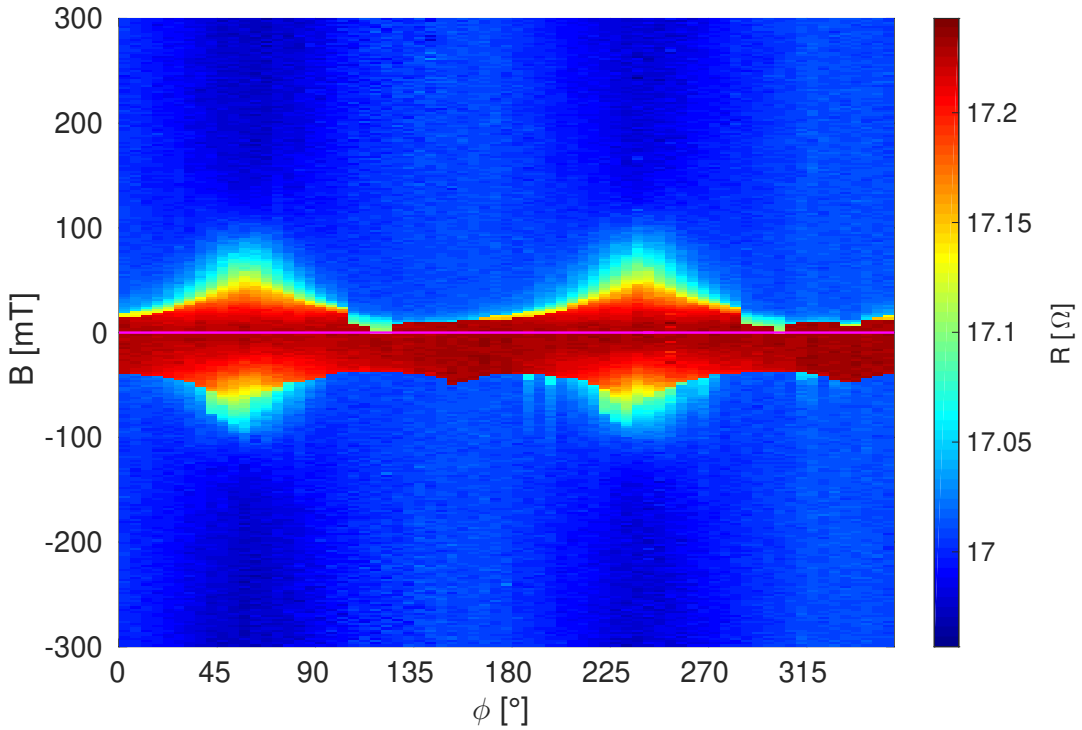

Figure 5.9: Depiction of the surface plot of R_{GMR} in dependence of B_{ext} and direction ϕ (angle between B_{ext} and x-axis of the cryostat magnet). The two maxima represent the hard axis of the GMR stack implying that the easy axis lies at $\phi \approx 140°$. This direction also corresponds to the correct orientation of the sample stick relative to the cryostat magnetic field axes. The sample under study is QC0423 C.

After getting the correct orientation of B_{ext} the major and minor loops can be measured (Fig. 5.10). Fig. 5.10a shows the GMR of the major loop between $B_{ext} = \pm 1000\,\text{Oe}$ taken for a range of $B_{ext} = \pm 3000\,\text{Oe}$, which is the reason that ΔR is normalized to the R_{GMR} value at $B_{ext} = 3000\,\text{Oe}$. The directions of change are marked by black and red arrows and show a GMR of $\approx 1.3\%$ with two clearly distinguishable states. The higher state corresponds to $Ni_{80}Fe_{20}$ and $Co_{50}Fe_{50}$ being anti-parallel (sec. 5.1.2). This state holds for both directions at $B_{ext} = 0$ which implies anti-ferromagnetic coupling between $Ni_{80}Fe_{20}$ and $Co_{50}Fe_{50}$, a constellation that had already been present in the array of pillars (sec. 4.3). The transition from parallel to anti-parallel at $B_{ext} \approx \pm 100\,\text{Oe}$ is not as sharp as the transition from anti-parallel to parallel at $B_{ext} \approx \pm 500\,\text{Oe}$. This behavior might result from a partial break up of the $Ni_{80}Fe_{20}$ layer into a few more regions with different magnetization directions. This behavior becomes more dominant in Fig. 5.10b where the minor loop of the switch at $B_{ext} \approx +100\,\text{Oe}$ and secondary minor loops are shown. Here changes are also indicated by arrows as well as corresponding numbers that indicate the order of the minor loops. The paths of 0,1 and 2 form the first minor loop. Furthermore paths

3 and 4 can also be extracted as a secondary minor loop. Switches along path 5 are used to extract SOT efficiencies for opposite currents than extracted from switches along path 1. For unknown reasons switches along path 2 only occur for low currents. All shown curves reproduce multiple times with stable fields where switching occurs. This fact is also frequently checked during SOT measurements. Sometimes the application of a DC current leads to a change of R_{GMR} which shifts the whole $R_{GMR}(B)$ curve vertically. This most probably stems from damages induced by leakage currents as the tunnel barrier has a finite resistance between $5 - 25\,\mathrm{k\Omega}$. For QC0423 C the measured resistance is $R_T \approx 8\,\mathrm{k\Omega}$ while QC0542 C reads $R_T \approx 21\,\mathrm{k\Omega}$.

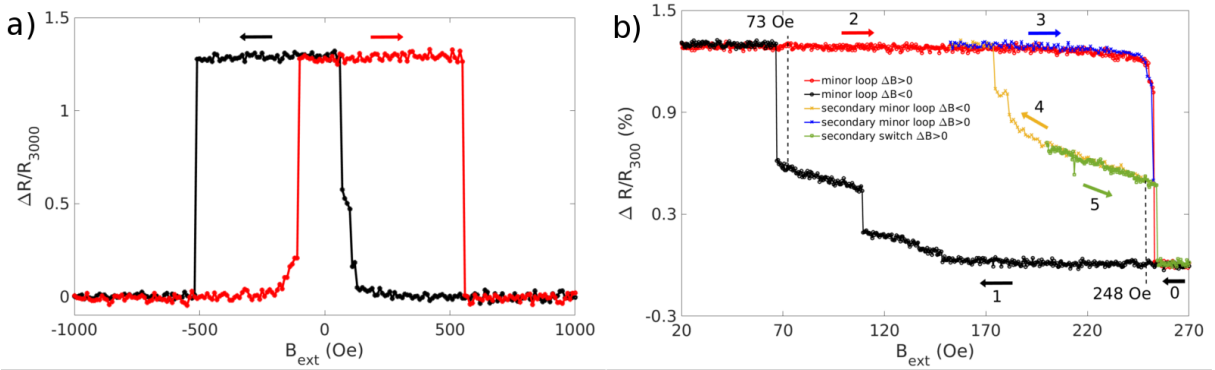

Figure 5.10: Depiction of the major and minor loops of a nano pillar along the easy axis. In a) the GMR shows good switching behavior with small deviations at $B_{ext} \approx \pm 100\,\mathrm{Oe}$. In b) the first minor loop consists of paths 0,1 and 2 while a secondary minor loop is shown by paths 3 and 4. Path 5 is used for later SOT efficiency measurements as the counter part to path 1. The sample under study is QC0423 C.

5.3.3. Current-induced Switching of an adjacent Magnetization

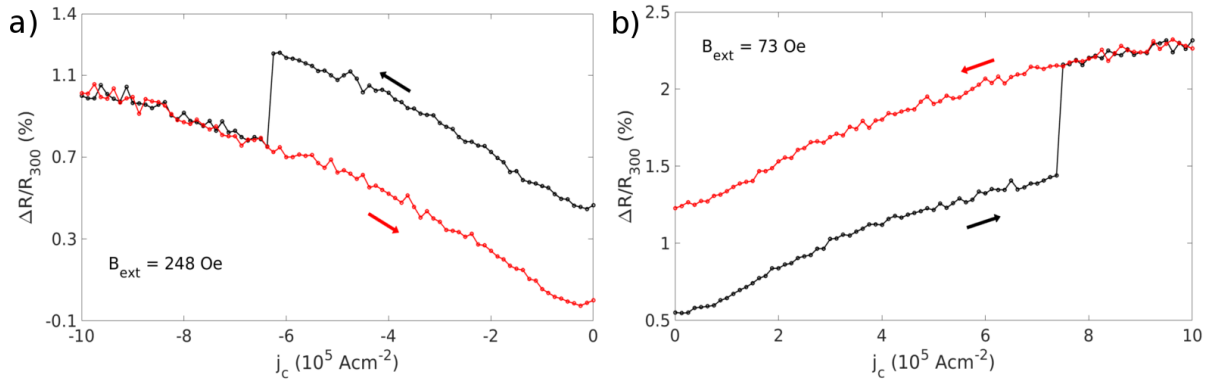

Figure 5.11: Depiction of measured GMR with respect to the DC current density j_c pushed through the current channel. For negative currents the switch occurs at $B_{ext} = 248\,\mathrm{Oe}$, while for positive currents M_{Py} is switching at $B_{ext} = 73\,\mathrm{Oe}$. The direction of change is marked by black and red arrows. Here the differences between red and black curves correspond exactly to the change in GMR at the related B_{ext}. The sample under study is QC0423 C.

From sec. 5.3.2 we know that the sensor is working correctly when responding to an external magnetic field B_{ext}. Now the idea is to set B_{ext} as close as possible to a magnetic field right before

the switch occurs. This position should be stable meaning that no switch occurs within a long period of time (e.g. 10-30 minutes), which is much larger than the duration of the measurement. In the case of the sample QC0423 C applying a positive current leads to switching of the magnetization M_{Py} when $B_{ext} = 73\,\mathrm{Oe}$ (Fig. 5.11a). This corresponds to path 1 in Fig. 5.10b). The approximate position of $B_{ext} = 73\,\mathrm{Oe}$ is marked by dotted lines. It can be seen that the GMR changes from $\frac{\Delta R}{R} \approx 0.5\%$ to $\frac{\Delta R}{R} \approx 1.3\%$ which is the same change in Fig. 5.11a at $j_c = 0$. Conceptually the same happens at $B_{ext} = 248\,\mathrm{Oe}$ of path 5 but with a negative current. The drift in $\frac{\Delta R}{R}$ can be explained by a rising instability of the resistance bridge due to a rising current that penetrates the tunnel barrier. The more parasitic current crosses the GMR measurement path the harder it gets to balance it. Heating is rather unlikely as the bath temperature is kept at $T = 4.2\,\mathrm{K}$ or $T = 1.8\,\mathrm{K}$. The shown graphs in Fig. 5.11 reproduce with varying switching currents.

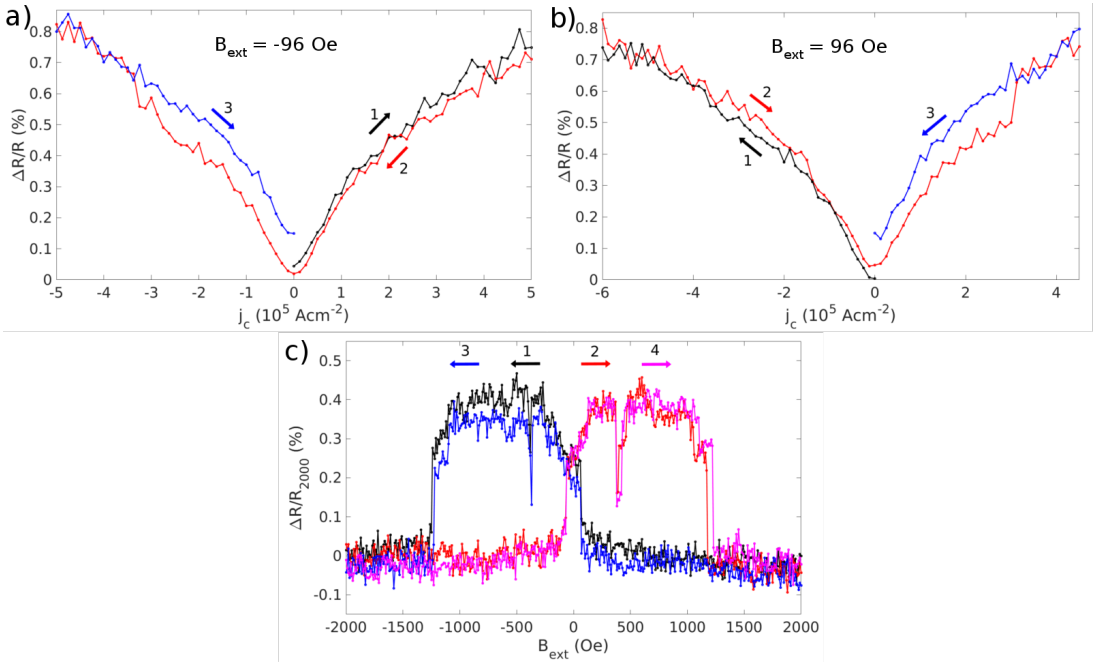

Figure 5.12: Switching behavior for two different magnetic fields $B_{ext} = -96\,\mathrm{Oe}$ and $B_{ext} = 96\,\mathrm{Oe}$ of the reference sample QC0542 C (a,b). By pushing current along paths 1 to 3 it is always one current direction where the switch occurs. c) shows the switching behavior of QC0542 C which is reproducible at $B_{ext,0} = \pm 94\,\mathrm{Oe}$.

In order to reproduce the results of QC0423 C a second sample, namely QC0542 C, is built and tested. The second sample is also used to systematically rule out heating as the reason for switching. In that case both current directions would result in changing the magnetization direction of $Ni_{80}Fe_{20}$. The experimental results are shown in Fig. 5.12. Here switching at a specific magnetic field occurs only for the corresponding current direction. For both transitions at $B_{ext} = \pm 96\,\mathrm{Oe}$ the current is swept from path 1 to path 3. The limits of j_c are $\approx 50\%$ (Fig. 5.12a) and $\approx 100\%$ (Fig. 5.12b) higher than the switching points to make sure that the effect is only one sided. Compared to QC0423 C this sample shows worse switching behavior of the sensor.

All measurements for current induced switching are performed at transitions from parallel to anti-parallel, where the switch occurs at reproducible $B_{ext,0} \approx \pm 94\,\mathrm{Oe}$ (Fig. 5.12c).

5.3.4. Extraction of Spin-Orbit Torque Efficiencies

Section 5.3.3 describes the measurement process for gaining the current density j_c needed to switch the magnetization for a certain supporting magnetic field $B_{ext} = B_{ext,0}$. With this it is possible to define an effective magnetic field $\Delta B = B_{ext} - B_{ext,0}$ which is directly proportional to the magnetic field generated by SOT (Fig. 5.2). This stems from the geometry of the sample where current direction and the magnetic easy axis are perpendicular to each other and lying in the plane of the sample. Fig. 5.13 shows all measured j_c for different ΔB. All points are presented as a range between highest and lowest j_c values.

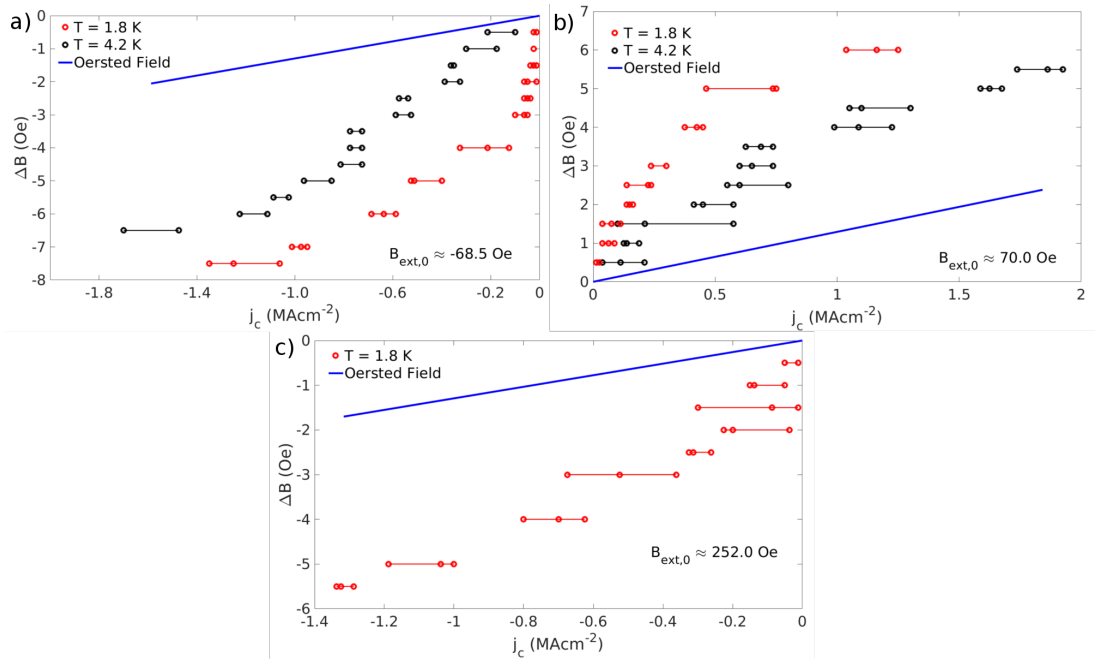

Figure 5.13: Depiction of the generated magnetic field ΔB for corresponding DC current densities j_c at different $B_{ext,0}$. All points are presented as a range between highest and lowest j_c value. In a) and b) the slope for small j_c differs significantly for the two temperatures $T = 1.8\,\mathrm{K}$ and $T = 4.2\,\mathrm{K}$ indicating that the effect is not depending on a Biot-Savart field (Oersted field). In c) only the curve for $T = 1.8\,\mathrm{K}$ is present as the initial point for switching at $B_{ext,0} = 252\,\mathrm{Oe}$ could not be reached at $T = 4.2\,\mathrm{K}$. Furthermore the calculated ΔB values for an Oersted field are much smaller than the observed behavior which is shown by the blue line.

In Fig. 5.13a a $j_c < 0$ results in $\Delta B < 0$ as $B_{ext,0} = -68.5\,\mathrm{Oe}$ (red curve of Fig. 5.10a). In Fig. 5.13b it is exactly the oppisite case at $B_{ext,0} = +70\,\mathrm{Oe}$. Furthermore Fig. 5.13c shows $\Delta B < 0$ for $j_c < 0$ just like in Fig. 5.13a). This behavior is consistent as both graphs (Fig. 5.13a,c) represent the M_{Py} switching from *left to right* (according Fig. 5.10a). Fig. 5.13c is lacking the behavior for $T = 4.2\,\mathrm{K}$ as it was not possible to reach the plateau at $\Delta R/R \approx 0.3\%$ of path 5 in Fig. 5.10b at that temperature. Both graphs in Fig. 5.13a,b show a major increase of ΔB with j_c when the temperature is lowered from $T = 4.2\,\mathrm{K}$ to $T = 1.8\,\mathrm{K}$. Such a behavior is a strong indication that

the dominant switching mechanism is not caused by Biot-Savart fields as these depend purely on current density. In order to strengthen this argument the value of a purely by current generated Oersted field B_{Oe} is plotted as well (equ. 5.7). At $T = 4.2\,\mathrm{K}$ the slope of ΔB is approximately three times higher than B_{Oe}. In the case of $T = 1.8\,\mathrm{K}$ it is even a factor of > 100. Furthermore it can be seen that the slope gets smaller for higher current densities. One possibility is that with higher energy of the electron states more scattering occurs which results in a lower current to spin conversion efficiency. Additionally activated bulk states, which do not have their spin locked to their momentum, could screen the topological surface states which reduces the effective coupling between spins and magnetization.

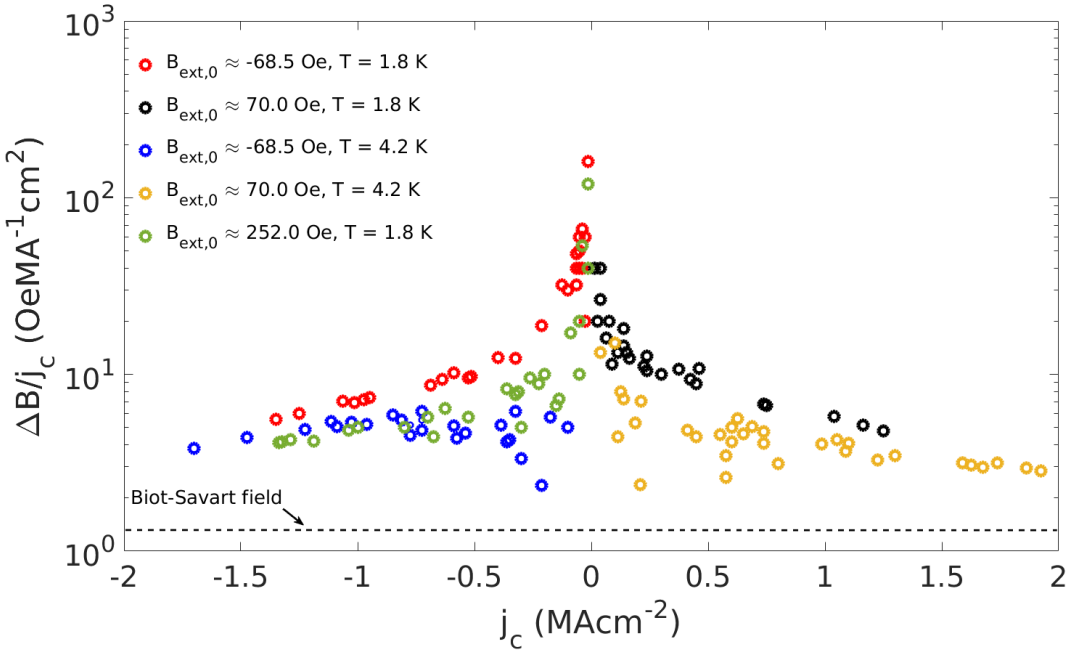

Figure 5.14: Depiction of all gathered SOT efficiency values $\Delta B/j_c$ as a function of j_c for different $B_{ext,0}$ and temperatures. The dotted line represents the current generated Oersted field which lies below all measured efficiencies. Lower temperatures show clearly higher efficiencies. The peak value reaches $\Delta B/j_c = 160\,\mathrm{OeMA^{-1}cm^2}$.

For the sake of comparability all gathered SOT efficiency values $\Delta B/j_c$ are put in one graph (Fig. 5.14). Here the SOT-efficiencies are depicted as a function of current density j_c, temperature T and external supporting magnetic field $B_{ext,0}$. The average baseline for all efficiencies for $j_c > 1 MAcm^{-2}$ is $\Delta B/j_c \approx 3$. The dotted line represents the efficiency of an Biot-Savart field and lies at $\Delta B/j_c \approx 1.2$ which is smaller than even the smallest measured efficiency values. For the lower temperature at $T = 1.8\,\mathrm{K}$ the behavior of $\Delta B/j_c$ changes drastically introducing a sharp rise even on a logarithmic scale. The highest measured value near $j_c \approx 0$ is $\Delta B/j_c = 160\,\mathrm{OeMA^{-1}cm^2}$. Average values next to this point are $\Delta B/j_c = 50\,\mathrm{OeMA^{-1}cm^2}$.

5.3.5. Comparison of Methodology and Efficiencies in other material Systems

In literature many different material systems are shown to exhibit SOT. Research on SOT was at the start dominated by heavy-metal/ferromagnet heterostructures [15, 16]. Aside from metal alloys [17] and anti-ferromagnets [18] also semiconductors [19] and topological insulators [20–23] were used as the generator for spin currents or spin accumulations. In first experiments with TIs the ferromagnetic material was simply coated onto Bi_2Se_3 [24] which leads to destruction of the helical spin structure due to hybridization of the surface states with the metal bands [25]. It became therefore unclear whether the measured SOT actually came from the surface state. Furthermore here the metallic FM channel has a much lower resistance compared to the TI resulting in a shunting effect which reduces the probability of generating a spin accumulation due to surface states. This issue was overcome by introducing magnetic insulators (MIs) on top of TIs [22, 23]. Band structure calculations have shown that TI/MI heterostructures with small lattice mismatches like Bi_2Se_3 /MnSe could exhibit a Dirac-cone feature [26]. Furthermore it was demonstrated that the MI induces ferromagnetism into the helical states of a 3D TI by the proximity effect [27]. Additionally it can be shown by first-principles calculations that a strong electrostatic potential mismatch at TI/MI interfaces could result in trivial states [28].

Despite these circumstances it is this combination of TI/MI, like $Bi_{0.9}Sb_{0.1}$ /$Mn_{0.6}Ga_{0.4}$, that exhibits huge SOT-efficiencies up to $\Delta B/j_c = 2300\,\mathrm{OeMA^{-1}cm^2}$ [22]. These values are derived directly from measurements of hysteresis curves as a function of an out-of-plane magnetic field at different current densities. It was shown that, depending on the current direction $\vec{j_c}$, the coercive force ΔH gets reduced or increased yielding high SOT-efficiencies $\Delta H/j_c$. The magnetization of the $Bi_{0.9}Sb_{0.1}$ /$Mn_{0.6}Ga_{0.4}$ heterostructure exhibits an out-of-plane magnetization with a big in-plane component $\vec{M}_x \parallel \vec{E}$ where $\vec{E}$ is the electric field. With $\vec{S} \parallel (\hat{\vec{z}} \times \vec{E}) \parallel \vec{\hat{y}}$ follows $\vec{B}_{FL} = B_{FL}\vec{\hat{y}}$ and $\vec{B}_{DL} = B_{DL}\left(\vec{m} \times \vec{\hat{y}}\right)$ resulting in maximum values for $\vec{T}_{FL,DL} = \vec{M} \times \vec{B}_{FL,DL}$ as $\vec{m} \perp \vec{\hat{y}}$. In our geometry $\vec{m} \parallel \vec{S}$ which yields minimum values for both $\vec{B}_{FL,DL}$ resulting in smaller $\vec{T}_{FL,DL}$ and therefore smaller efficiencies. Furthermore the saturation magnetization of $Mn_{0.6}Ga_{0.4}$ is $M_s \approx 250\,\mathrm{emu/cm^3}$ which is approximately 4 times smaller than for $Ni_{80}Fe_{20}$. As $d\vec{m}/dt \propto \gamma/M_s\vec{T}$ (equ. 5.1) this yields another reason why the efficiencies in our device is smaller than in the case of *Khang et al.*

Nevertheless our geometry offers the best way to investigate on B_{FL} as one can directly correspond B_{ext} to it. For TIs it is assumed that if $M_z = 0$ also $B_{DL} = 0$ (equ. 5.3). With $\vec{m}$ lying in-plane and $\vec{j_c} \perp \vec{m}$ the effective field-like component becomes $\vec{B}_{FL} \parallel \vec{m}$ being able to act directly opposed to $\vec{B}_{ext}$.

Concerning the comparison of efficiencies the only interesting references are [22, 23] where their efficiencies are more than 10 times higher than in our case. All other sources show mostly 10 times less efficiency. Furthermore *Khang et al.* and *Li et al.* provide direct measurement methods in order to gain values for efficiencies while other references derive them indirectly from fitting theoretical models to second harmonics of the measured anomalous Hall resistance [24].

Considering only the classes of in-plane magnetized anisotropies our device exhibits the up to date highest SOT efficiency ever recorded.

5.4. Summary and Outlook

Building an SOT-device requires the knowledge of the correct thickness of the tunnel barrier as well as knowledge about the correct constellation of a GMR stack. The proper device geometry and development of a lithographic process are also essential for producing working structures. Due to the sub-micron sizes, which are involved in the process, only electron-beam lithography can be used except for bigger device components like the outer contacts. In a finished SOT-device the functionality of the sensor is the first thing to measure. If the layer stack reacts to an external magnetic field like a spin-valve with two distinct states, the device can be tested for its SOT behavior. It was shown that in $Cd_{0.68}Hg_{0.32}Te$ /HgTe /$Cd_{0.68}Hg_{0.32}Te$ based nano devices only small current densities ($j \approx 10^4\,A/cm^2$) are needed to switch the magnetization of an adjacent FM. Furthermore $\Delta R/R$ measurements for positive and negative currents exhibit a switch for only one of the two directions indicating that the switching mechanism is not driven by thermal effects. SOT-efficiencies increase with decreasing temperatures and are generally higher at lower current densities. All measured efficiencies are at least three times higher than in the case of an Oersted field.

In comparison to most other material systems HgTe exhibits up to 10 times higher efficiencies. Furthermore most other geometries use second order harmonics of the measured anomalous Hall resistance in order to fit a model curve which yields values for the field-like and damping-like torques indirectly. The advantage of our geometry is that the spin induced magnetic field, in particular the field-like component, can be directly measured. In general in-plane magnetic anisotropy devices offer the advantage that they can be easaly produced. It is easier to define elongated shapes by means of modern lithography than conducting research on new materials with a perpendicular magnetic anisotropy [29]. This circumstance is most advantageous for low bit density devices as microcontrollers [30]. Considering only the classes of in-plane magnetized anisotropies the presented devices exhibit the up to date highest SOT efficiency ever recorded.

In the case of [22, 23], who are also conducting SOT experiments on TIs, efficiencies are even higher than in our case. The main reason for this could be that their magnetization is pointing out-of-plane resulting in higher spin torque contributions. Nevertheless it is unclear whether their SOT efficiencies are driven purely by surface states as magnetic insulators tend to influence the surface of TIs [27].

Due to the fact that out-of-plane magnetizations tend to generate higher efficiencies it would be interesting to put material systems with perpendicular to plane magnetic moments on top of HgTe . In this case it would be very likely to generate even higher efficiencies than in above mentioned publications. In our case such a device should be realizable as presumably any material system can be deposited on top of HgTe which is covered by ZrO_2 . Of course optimization of the layer stack would be needed. Furthermore it is unclear which influence HgTe on a perpendicular to plane magnetization has. These questions can be adressed in future investigations.

References

[1] S. Wolf, D. Awschalom, R. Buhrman, J. Daughton, v. S. von Molnár, M. Roukes, A. Y. Chtchelkanova, and D. Treger, *Spintronics: a spin-based electronics vision for the future,* science **294**, 1488 (2001).

[2] A. D. Kent and D. C. Worledge, *A new spin on magnetic memories,* Nature nanotechnology **10**, 187 (2015).

[3] J. Sinova and T. Jungwirth, *Surprises from the spin hall effect,* Physics today **70**, 38 (2017).

[4] K. Garello, F. Yasin, S. Couet, L. Souriau, J. Swerts, S. Rao, S. Van Beek, W. Kim, E. Liu, S. Kundu, *et al.*, *Sot-mram 300mm integration for low power and ultrafast embedded memories,* in *2018 IEEE Symposium on VLSI Circuits* (IEEE, 2018) pp. 81–82.

[5] N. Sato, F. Xue, R. M. White, C. Bi, and S. X. Wang, *Two-terminal spin–orbit torque magnetoresistive random access memory,* Nature Electronics **1**, 508 (2018).

[6] W. Han, Y. Otani, and S. Maekawa, *Quantum materials for spin and charge conversion,* npj Quantum Materials **3**, 1 (2018).

[7] A. Manchon and S. Zhang, *Theory of spin torque due to spin-orbit coupling,* Physical Review B **79**, 094422 (2009).

[8] J. C. Slonczewski *et al.*, *Current-driven excitation of magnetic multilayers,* Journal of Magnetism and Magnetic Materials **159**, L1 (1996).

[9] A. Manchon, J. Železnỳ, I. M. Miron, T. Jungwirth, J. Sinova, A. Thiaville, K. Garello, and P. Gambardella, *Current-induced spin-orbit torques in ferromagnetic and antiferromagnetic systems,* Reviews of Modern Physics **91**, 035004 (2019).

[10] P. B. Ndiaye, C. A. Akosa, M. H. Fischer, A. Vaezi, E.-A. Kim, and A. Manchon, *Dirac spin-orbit torques and charge pumping at the surface of topological insulators,* Physical Review B **96**, 014408 (2017).

[11] N. F. Mott, *The electrical conductivity of transition metals,* Proceedings of the Royal Society of London. Series A-Mathematical and Physical Sciences **153**, 699 (1936).

[12] E. Y. Tsymbal and D. G. Pettifor, *Perspectives of giant magnetoresistance,* in *Solid state physics*, Vol. 56 (Elsevier, 2001) pp. 113–237.

[13] T. Borzenko, C. Gould, G. Schmidt, and L. Molenkamp, *Metallic air-bridges fabricated by multiple acceleration voltage electron beam lithography,* Microelectronic engineering **75**, 210 (2004).

[14] A. Nikolic, K. Zhang, and C. Barnes, *Bulk and interface quantum states of electrons in multi-layer heterostructures with topological materials,* Journal of Physics: Condensed Matter **30**, 235001 (2018).

[15] K. Garello, I. M. Miron, C. O. Avci, F. Freimuth, Y. Mokrousov, S. Blügel, S. Auffret, O. Boulle, G. Gaudin, and P. Gambardella, *Symmetry and magnitude of spin–orbit torques in ferromagnetic heterostructures,* Nature nanotechnology **8**, 587 (2013).

[16] X. Fan, H. Celik, J. Wu, C. Ni, K.-J. Lee, V. O. Lorenz, and J. Q. Xiao, *Quantifying interface and bulk contributions to spin–orbit torque in magnetic bilayers,* Nature communications **5**, 1 (2014).

[17] L. Zhu, D. C. Ralph, and R. A. Buhrman, *Highly efficient spin-current generation by the spin hall effect in au 1- x pt x,* Physical Review Applied **10**, 031001 (2018).

[18] V. Tshitoyan, C. Ciccarelli, A. Mihai, M. Ali, A. Irvine, T. Moore, T. Jungwirth, and A. Ferguson, *Electrical manipulation of ferromagnetic nife by antiferromagnetic irmn,* Physical Review B **92**, 214406 (2015).

[19] T. Skinner, K. Olejník, L. Cunningham, H. Kurebayashi, R. Campion, B. Gallagher, T. Jungwirth, and A. Ferguson, *Complementary spin-hall and inverse spin-galvanic effect torques in a ferromagnet/semiconductor bilayer,* Nature Communications **6**, 1 (2015).

[20] S. Shi, A. Wang, Y. Wang, R. Ramaswamy, L. Shen, J. Moon, D. Zhu, J. Yu, S. Oh, Y. Feng, *et al.*, *Efficient charge-spin conversion and magnetization switching through the rashba effect at topological-insulator/ag interfaces,* Physical Review B **97**, 041115 (2018).

[21] J. Han, A. Richardella, S. A. Siddiqui, J. Finley, N. Samarth, and L. Liu, *Room-temperature spin-orbit torque switching induced by a topological insulator,* Physical review letters **119**, 077702 (2017).

[22] N. H. D. Khang, Y. Ueda, and P. N. Hai, *A conductive topological insulator with large spin hall effect for ultralow power spin–orbit torque switching,* Nature materials **17**, 808 (2018).

[23] P. Li, J. Kally, S. S.-L. Zhang, T. Pillsbury, J. Ding, G. Csaba, J. Ding, J. Jiang, Y. Liu, R. Sinclair, *et al.*, *Magnetization switching using topological surface states,* Science advances **5**, eaaw3415 (2019).

[24] A. Mellnik, J. Lee, A. Richardella, J. Grab, P. Mintun, M. H. Fischer, A. Vaezi, A. Manchon, E.-A. Kim, N. Samarth, *et al.*, *Spin-transfer torque generated by a topological insulator,* Nature **511**, 449 (2014).

[25] J. Zhang, J. P. Velev, X. Dang, and E. Y. Tsymbal, *Band structure and spin texture of bi 2 se 3 3 d ferromagnetic metal interface,* Physical Review B **94**, 014435 (2016).

[26] W. Luo and X.-L. Qi, *Massive dirac surface states in topological insulator/magnetic insulator heterostructures,* Physical Review B **87**, 085431 (2013).

[27] S. Eremeev, V. Men'Shov, V. Tugushev, P. M. Echenique, and E. V. Chulkov, *Magnetic proximity effect at the three-dimensional topological insulator/magnetic insulator interface,* Physical Review B **88**, 144430 (2013).

[28] S. V. Eremeev, M. M. Otrokov, and E. V. Chulkov, *New universal type of interface in the magnetic insulator/topological insulator heterostructures,* Nano letters **18**, 6521 (2018).

[29] S. Bhatti, R. Sbiaa, A. Hirohata, H. Ohno, S. Fukami, and S. Piramanayagam, *Spintronics based random access memory: a review,* Materials Today **20**, 530 (2017).

[30] D. Apalkov, B. Dieny, and J. Slaughter, *Magnetoresistive random access memory,* Proceedings of the IEEE **104**, 1796 (2016).

6

Summary

Magnetic random access memory (MRAM) technology aims to replace dynamic RAM (DRAM) due to its significantly lower power consumption and non-volatility [1, 2]. During the last couple of years the commercial focus was set on spin-transfer torque MRAM (STT-MRAM) systems, where a current is pushed through a ferromagnetic (FM) free layer and a reference layer which are separated by an insulator. The free layer can be set to parallel or anti-parallel depending on the current direction [3]. Unfortunately these currents have to be quite high which could lead to damages of the tunnel barrier of the magnetic tunnel junction resulting in higher power consumption as well as reliability issues. At this point a new effect, where the current is passed below the ferromagnetic layer stack, can be exploited to change the direction of the free layer magnetization. The effect is known as spin-orbit torque (SOT) and describes the transfer of angular momentum onto an adjacent magnetization either by the spin Hall effect (SHE) or inverse spin galvanic effect (iSGE) [4]. The latter describes a spin accumulation due to a current. This is similar to the process of spin accumulation in TIs, where a current corresponds to an effective spin due to spin-momentum locking [5]. Thus TIs exhibit a high current-to-spin conversion rate, which makes them a promising material system for SOT experiments. Among all TIs it is HgTe, which can be reliably grown as an insulator. This thesis covers the development of a working device for SOT measurements (SOT-device) in a CdTe /$Cd_{0.68}Hg_{0.32}Te$ /HgTe /$Cd_{0.68}Hg_{0.32}Te$ heterostructure. It involves the development of a tunnel barrier (ZrO_2) as well as the investigation of the behavior of a ferromagnetic layer stack on top of etched HgTe. The main result of this work is the successful construction and evaluation of a working SOT-device, which exhibits the up to date most efficient switching of in-plane magnetized ferromagnetic layer stacks.

In order to avoid hybridization between HgTe and the adjacent ferromagnetic atoms, which would cause a breakdown of the topological surface state, it is necessary to implement a thin tunnel barrier in between the TI and free layer [6]. Aside from hybridization a tunnel barrier avoids shunting of the current, that is pushed on the surface of the HgTe /$Cd_{0.68}Hg_{0.32}Te$ interface.

Thus a bigger part of the current can be used for spin accumulation and, at the same time, the resistance measurement of the ferromagnetic layer stack is not perturbed. In chapter 3 the focus is set on investigating the tunneling characteristics of ZrO_2 on top of dry etched HgTe . Thin barriers are used as the interaction of the current generated spin and the adjacent magnetization decreases with distance. On the other hand too small insulator thicknesses lead to leakage currents which disturb heavily the measurement of the resistance of the ferromagnetic layer stack. Thus an optimum thickness of 10 ALD cycles ($d \approx 1.6\,\mathrm{nm}$) is determined which yields a resistance area product of $R \cdot A \approx 3\,\mathrm{k\Omega\mu m^2}$. This corresponds to a tunneling resistance of $R_T \approx 20\,\mathrm{k\Omega}$ over a structure surface of $A_T = 0.12\,\mu\mathrm{m}^2$. Multiple samples with different thicknesses have been produced. All samples have been examined on their tunneling behavior. The resistance area product as a function of thickness shows a linear behavior on a logarithmic scale. Furthermore all working samples show non-linear I-V curves as well as parabolic dI/dV-curves. Additionally the tunneling resistance R_T increases with decreasing temperature. All above mentioned properties are typical for tunnel barriers which do not include pinholes [7]. The last part of chapter 3 deals with thermal properties of HgTe . By measuring the second harmonic of a biasing AC current in the channel below the tunnel barrier it is attempted to extract the diffusion thermopower of the heated electrons. Unfortunately the measured signal showed a far superior contribution of the first harmonic. According to electric circuit simulations a small asymmetry in the barrier (penetration and leaving point of electrons) could be responsible for this behavior.

A ferromagnetic layer stack, consisting of $Ni_{80}Fe_{20}$ /Cu /$Co_{50}Fe_{50}$, serves as a sensor for magnetization changes due to external fields and current induced spin accumulations. The layer stack exhibits a giant magnetoresistance (GMR) which has been measured by a resistance bridge. The biggest peculiarity in depositing a GMR stack on top of HgTe is that its easy axis forms along only one of the crystal axes ((110) or $(1\bar{1}0)$). The reason for this anisotropy is still unclear. Sources such as an influence of the terminating material, miscut, furrows during IBE or sputter ripples have been ruled out. It can be speculated that the surface states due to HgTe might have an influence on the development of this easy axis but this would need further investigation. A consequence of this unexpected anisotropy is that every CdTe /$Cd_{0.68}Hg_{0.32}Te$ /HgTe /$Cd_{0.68}Hg_{0.32}Te$ wafer has first to be characterized in SQUID in order to find the easy axis. A ferromagnetic resonance (FMR) measurement confirmed this observation. The shape of the ferromagnetic layer stack is chosen to be an ellipse in order to support the easy axis direction by shape anisotropy. Over 8 million ellipses are used to generate a SQUID signal of $m > 10^{-5}\,\mathrm{emu}$. This is sufficient to extract the main characteristics of an average nano pillar under the influence of an external magnetic field. As in the case of bigger structures the ellipse shaped structure shows a step-like behavior. A measured minor loop confirms the existence of the irreversible anti-parallel stable magnetic state. Furthermore this state persists for both directions at $m = 0$ resulting in an anti-ferromagnetic coupling between $Ni_{80}Fe_{20}$ and $Co_{50}Fe_{50}$.

The geometry of the SOT-device is chosen in such a way that the current induced spin aligns either parallel or anti-parallel to the effective magnetic field $\vec{B}_{eff} = \vec{B}_{ext} + \vec{B}_{aniso} + \vec{B}_{shape}$, which

acts on the pillar. Due to interaction of the spin with the adjacent magnetization of $Ni_{80}Fe_{20}$ the magnetization direction gets changed by a torque $\vec{T}$. In general this torque can be decomposed into two components a field-like torque $\vec{\tau}_{FL}$ and a damping-like torque $\vec{\tau}_{DL}$ [4]. In the case of TIs $\vec{T}$ is additionally depending on the z-component of $\vec{m}$ [8]. In our case the magnetization is lying in the sample plane ($m_z = 0$) which results in $\vec{\tau}_{DL} = 0$. Thus, in the case of $\vec{S} \parallel \left(\vec{\hat{z}} \times \vec{j}\right)$ and $\vec{j} \parallel \vec{\hat{y}}$, the only spin dependent effective magnetic field is $\vec{B}_{FL} = \tau_{FL} \cdot \vec{\hat{x}}$ which is lying parallel or anti-parallel to $\vec{B}_{eff}$. The evaluation of $\vec{B}_{FL}$ can therefore be done in the following manner. First a high B_{ext} has to be set along the easy axis of the pillar. Then B_{ext} has to be reduced just a few Oe before the switching occurs at the magnetic field $B_{ext,0}$. At the magnetic field $\Delta B = B_{ext} - B_{ext,0} \approx 0.5\,\mathrm{Oe}$ the lower resistive state should be stable over a longer time range $(10 - 30\,\mathrm{min})$ in order to exclude switching due to fluctuations. Now a positive or negative current can be pushed through the channel below the pillar. For one of the two current directions the magnetization of $Ni_{80}Fe_{20}$ switches. It is therefore not a thermal effect that drives the change of $\vec{m}$. Current densities that are able to switch $\vec{m}$ at small $\Delta B \neq 0$ lie in the range of $j \approx 10^4\,\mathrm{A/cm^2}$. In all experiments the switching efficiency $\Delta B/j$ decreases with rising j. Furthermore the efficiency as a function of j depends on the temperature as $\Delta B/j$ values tend to be up to 20 times higher at $T = 1.8\,\mathrm{K}$ and $j \approx 0$ than at $T = 4.2\,\mathrm{K}$. This temperature dependence suggests that switching occurs not due to Oersted fields. Furthermore the Biot-Savart fields had been calculated for four different models: an infinite long rectangular wire, two infinite planes, a full volume and two thin volume planes. Every model shows an efficiency, which is at least three times lower than the observation.

The highest efficiencies in our samples show up to 10 times higher values than in heavy-metal/ferromagnets heterostructures. In contrast to measurement procedures of most other groups our method leads to direct determination of SOT parameters like the effective magnetic field $\vec{B}_{FL}$. Other groups make use of spin-transfer FMR (ST-FMR) where they AC bias their structure and extract SOT parameters (like τ_{FL} and τ_{DL}) from second harmonics by fitting theoretical models. Material systems consisting of TIs and magnetic insulators (MIs) on the other hand show 10 times higher efficiencies [9, 10]. In those cases the magnetization points out of the sample plane which is conceptually different from in-plane magnetic anisotropy geometries like in our case. The greatest benefit in-plane magnetic anisotropy systems is its easy realisation [11]. Here only an elliptical shape has to be lithographically implemented instead of conducting research on the appropriate combination of material systems that result in perpendicular magnetic anisotropies [12]. Despite the fact that in our case only $\vec{\tau}_{FL}$ acts as the driving force for changing m our device still exhibits the up to date highest efficiencies in the class of in-plane magnetized anisotropies of all material classes ever recorded.

References

[1] R. Desikan, C. R. Lefurgy, S. W. Keckler, D. Burger, *et al.*, *On-chip MRAM as a high-bandwidth, low-latency replacement for DRAM physical memories* (Computer Science Department, University of Texas at Austin, 2002).

[2] X. Dong, X. Wu, G. Sun, Y. Xie, H. Li, and Y. Chen, *Circuit and microarchitecture evaluation of 3d stacking magnetic ram (mram) as a universal memory replacement,* in *2008 45th ACM/IEEE Design Automation Conference* (IEEE, 2008) pp. 554–559.

[3] W. Kim, J. Jeong, Y. Kim, W. Lim, J. Kim, J. Park, H. Shin, Y. Park, K. Kim, S. Park, *et al.*, *Extended scalability of perpendicular stt-mram towards sub-20nm mtj node,* in *2011 International Electron Devices Meeting* (IEEE, 2011) pp. 24–1.

[4] A. Manchon, J. Železnỳ, I. M. Miron, T. Jungwirth, J. Sinova, A. Thiaville, K. Garello, and P. Gambardella, *Current-induced spin-orbit torques in ferromagnetic and antiferromagnetic systems,* Reviews of Modern Physics **91**, 035004 (2019).

[5] X.-L. Qi and S.-C. Zhang, *Topological insulators and superconductors,* Reviews of Modern Physics **83**, 1057 (2011).

[6] J. Zhang, J. P. Velev, X. Dang, and E. Y. Tsymbal, *Band structure and spin texture of bi 2 se 3 3 d ferromagnetic metal interface,* Physical Review B **94**, 014435 (2016).

[7] B. Jönsson-Åkerman, R. Escudero, C. Leighton, S. Kim, I. K. Schuller, and D. Rabson, *Reliability of normal-state current–voltage characteristics as an indicator of tunnel-junction barrier quality,* Applied Physics Letters **77**, 1870 (2000).

[8] P. B. Ndiaye, C. A. Akosa, M. H. Fischer, A. Vaezi, E.-A. Kim, and A. Manchon, *Dirac spin-orbit torques and charge pumping at the surface of topological insulators,* Physical Review B **96**, 014408 (2017).

[9] N. H. D. Khang, Y. Ueda, and P. N. Hai, *A conductive topological insulator with large spin hall effect for ultralow power spin–orbit torque switching,* Nature materials **17**, 808 (2018).

[10] P. Li, J. Kally, S. S.-L. Zhang, T. Pillsbury, J. Ding, G. Csaba, J. Ding, J. Jiang, Y. Liu, R. Sinclair, *et al.*, *Magnetization switching using topological surface states,* Science advances **5**, eaaw3415 (2019).

[11] S. Bhatti, R. Sbiaa, A. Hirohata, H. Ohno, S. Fukami, and S. Piramanayagam, *Spintronics based random access memory: a review,* Materials Today **20**, 530 (2017).

[12] D. Apalkov, B. Dieny, and J. Slaughter, *Magnetoresistive random access memory,* Proceedings of the IEEE **104**, 1796 (2016).

7

Zusammenfassung

Magnetic random access memory (MRAM) ist eine Technologie, die darauf abzielt dynamic RAM (DRAM) aufgrund der geringeren Energieaufnahme und ihrer magnetischen Beständigkeit zu ersetzen [1, 2]. In den letzten Jahren wurde der kommerzielle Fokus auf spin-transfer MRAM (STT-MRAM) gelegt. Bei diesen Systemen wird der Strom an zwei durch einen Isolator getrennte Ferromagneten (FM), einer freien Schicht und einer Referenzschicht gelegt. Je nach Stromrichtung kann sich die freie Schicht parallel oder anti-parallel zur Referenzschicht anordnen [3]. Jedoch können die zur Ummagnetisierung notwendigen Ströme so hoch ausfallen, dass die Tunnelbarriere schaden nimmt, wodurch ein höherer Energieverbrauch und unzuverlässiges Verhalten hervorgerufen werden. An dieser Stelle besteht die Möglichkeit einen anderen Effekt auszunutzen, für den der Strom unter der freien Schicht angelegt wird, um die nächstgelegene Magnetisierung zu beeinflussen. Beim sogenannten spin-orbit torque (SOT) wird das magnetische Moment eines zur elektrischen Leitung beitragenden Elektrons auf die darüber liegende Magnetisierung übertragen. Dies geschieht entweder anhand des spin Hall effect (SHE) oder inverse spin galvanic effect (iSGE) [4]. Letzteres beschreibt eine Spinakkumulation aufgrund eines elektrischen Stromflusses, welche auch bei topologischen Isolatoren (TI) auftritt. Diese speziellen Materialsysteme besitzen leitende Oberflächenzustände, bei denen Impuls- und Spinvektor senkrecht aufeinander stehen (spin-momentum locking) und in der Probenebene liegen [5]. Hieraus resultiert eine hohe Strom-zu-Spin Umwandlungsrate, wodurch sich TIs besonders gut für SOT Experimente eignen. Unter allen TIs ist HgTe das Materialsystem, welches zuverläassig als Isolator gewachsen werden kann. Die vorliegende Arbeit befasst sich mit der Entwicklung und dem Aufbau einer mikrostrukturierten Apparatur zur Bestimmung von SOT Parametern (SOT-Struktur) in einem CdTe /$Cd_{0.68}Hg_{0.32}Te$ /HgTe /$Cd_{0.68}Hg_{0.32}Te$ Materialsystem. Es umfasst die Entwicklung einer Tunnelbarriere (ZrO_2), sowie die Untersuchung des Verhaltens ferromagnetischer Strukturen auf der Oberfläche von trockengeätztem HgTe . Die Kernaussage dieser Arbeit ist, dass das vorliegende erfolgreich realisierte SOT-device die höchsten bis dato bekannten Effizienzen in der

Ummagnetisierung von planar anisotropischen ferromagnetischen Strukturen aufweist.

Um die Hybridisierung zwischen HgTe und dem darüber liegenden FM und somit einen Zusammenbruch der Oberflächenzustände zu vermeiden, muss zwischen den beiden Materialien eine Tunnelbarriere eingefügt werden [6]. Neben der Verhinderung der Hybridisierung, sorgt die Tunnelbarriere für eine Verminderung des Leckstromes, wodurch der größte Teil des elektrischen Stroms zur Spinakkumulation beitragen kann. Zudem werden Störungen bei der Widerstandsmessung des ferromagnetischen Schichtsystems reduziert. Kapitel 3 befasst sich mit der Erforschung von Tunnelcharakteristiken von ZrO_2 auf trockengeätztem HgTe. Es werden dünne Schichten verwendet, da die Wechselwirkung zwischen Spin und Magnetisierung mit dem Abstand zueinander abnimmt. Andererseits führt eine zu dünne Isolatorschicht zu einem hohen Leckstrom, welcher die Widerstandsmessung der ferromagnetischen Schichtstruktur stark beeinflusst. Folglich wurde eine optimale Isolatordicke bestimmt, die 10 ALD Zyklen ($d \approx 1,6\,\mathrm{nm}$) entspricht und ein Widerstandsflächenprodukt von $R \cdot A \approx 3\,\mathrm{k\Omega\mu m^2}$ ergibt. Dies entspricht einem Tunnelwiderstand von $R_T \approx 20\,\mathrm{k\Omega}$ bei einer Strukturfläche von $A_T = 0.12\,\mu\mathrm{m}^2$. Es werden mehrere Proben unterschiedlicher Dicke hergestellt und auf ihre Tunnelcharakteristiken untersucht. Das Widerstandsflächenprodukt in Abhängigkeit von der Barrierendicke zeigt lineares Verhalten auf einer logarithmischen Skala. Darüber hinaus weisen alle funktionierenden Proben nicht-lineare I-V Kurven und parabolische dI/dV Verläufe auf. Der Tunnelwiderstand R_T steigt mit abnehmender Temperatur. Die genannten Eigenschaften sind typisch für Tunnelbarrieren ohne lokal stark ausgedünnte Stellen (pinholes) [7]. Am Ende von Kapitel 3 wird die Möglichkeit zur Bestimmung thermischer Eigenschaften von HgTe erörtert. Hierbei wird das Signal der zweiten Harmonischen eines AC Anregungsstromes, der unterhalb der Tunnelbarriere verläuft, gemessen, um den diffusiven Seebeck Effekt durch die geheizten Elektronen zu bestimmen. Messungen zeigen jedoch, dass das gemessene Signal zum größten Teil aus der ersten Harmonischen besteht. Mit Hilfe von Schaltkreissimulationen kann gezeigt werden, dass dieses Verhalten vor allem der Asymmetrie der Tunnelbarriere (Ein- und Ausstiegspunkt der Elektronen) geschuldet ist.

Eine ferromagnetische Schichtstruktur, bestehend aus $Ni_{80}Fe_{20}$ /Cu /$Co_{50}Fe_{50}$, dient als ein Sensor zur Erfassung von Magnetisierungsänderungen, die durch externe magnetische Felder und Spinakkumulationen hervorgerufen werden. Die erwähnte Schichtstruktur weist einen Riesenmagnetowiderstand (GMR) auf, der mit Hilfe einer Widerstandsbrücke gemessen wird. Die größte Besonderheit bei der Ablagerung einer GMR Schichtstruktur auf trockengeätztem HgTe ist die Ausbildung einer leichten Richtung (easy axis) entlang nur einer bestimmten Kristallachse ((110) oder $(1\bar{1}0)$). Der Grund für diese Anisotropie ist weiterhin unbekannt. Mögliche Ursachen wie der Einfluss des terminierenden Materials, miscut, Furchenbildung während des IBE und Wellenbildung durch Magnetronsputtern konnten ausgeschlossen werden. Es besteht die vage Vermutung, dass die Oberflächenzustände von HgTe in Verbindung mit der Ausbildung der easy axis stehen. Dies gilt es jedoch in zukünftigen Studien kritisch zu prüfen. Als Folge dieser unwerwarteten Anisotropie muss jeder neue CdTe /$Cd_{0.68}Hg_{0.32}Te$ /HgTe /$Cd_{0.68}Hg_{0.32}Te$ wafer zunächst im SQUID charakterisiert werden, um die easy axis einmalig zu bestimmen. Anhand von ferro-

magnetischen Resonanzmessungen (FMR) konnten die obigen Beobachtungen bestätigt werden. Die Schichtstrukturen (pillars) weisen eine elliptische Form auf, sodass die Formanisotropie die Bildung einer easy axis entlang einer bestimmten Richtung begünstigt. Über 8 Millionen Ellipsen werden verwendet, um ein SQUID Signal von $m > 10^{-5}$ emu zu generieren. Hierdurch werden die charakteristischen Merkmale eines durchschnittlichen nano pillars unter dem Einfluss eines externen Magnetfeldes bestimmt. Wie auch bei größeren Strukturen weist ein durchschnittlicher pillar eine stufenförmige Hysterese auf. Durch Umkehrung des Magnetfelds am Ort des Zwischenzustandes lässt sich beweisen, dass es sich um einen tatsächlichen irreversiblen stabilen anti-ferromagnetischen Zustand handelt. Dieser Zustand liegt bei beiden Magnetfeldrichtungen für $m = 0$ vor, was zeigt, dass $Ni_{80}Fe_{20}$ und $Co_{50}Fe_{50}$ anti-ferromagnetisch koppeln.

Die Geometrie der SOT-Struktur ist so gewählt, dass die strominduzierte Spinakkumulation entweder parallel oder anti-parallel zum effektiven Magnetfeld $\vec{B}_{eff} = \vec{B}_{ext} + \vec{B}_{aniso} + \vec{B}_{shape}$, welches auf den pillar wirkt. Dieser Spin wechselwirkt mit der Magnetisierung des $Ni_{80}Fe_{20}$, was eine Richtungsänderung der Magnetisierung durch ein Drehmoment $\vec{T}$ (torque) bewirkt. Im Allgemeinem lässt sich diese torque in zwei Komponenten, eine feldähnliche (field-like) torque $\vec{\tau}_{FL}$ und eine dämpfende (damping-like) torque $\vec{\tau}_{DL}$, aufspalten [4]. Im Falle von TIs hängt $\vec{T}$ zusätzlich von der z-Komponente des magnetischen Moments $\vec{m}$ ab [8]. Im hier vorliegenden Fall liegt die Magnetisierung von $Ni_{80}Fe_{20}$ in der Probenebene ($m_z = 0$), wodurch $\tau_{DL} = 0$. Folglich ergibt sich, unter der Annahme $\vec{S} \parallel \left(\vec{\hat{z}} \times \vec{j}\right)$ und $\vec{j} \parallel \vec{\hat{y}}$, als einziges spinabhängiges Magnetfeld $\vec{B}_{FL} = \tau_{FL} \cdot \vec{\hat{x}}$, welches parallel oder anti-parallel zu $\vec{B}_{eff}$ liegt. Die Bestimmung von $\vec{B}_{FL}$ erfolgt somit auf folgende Art und Weise. Zunächst wird ein hohes B_{ext} entlang der easy axis des nano pillars angelegt. Anschließend muss B_{ext} soweit reduziert werden bis der magnetische Zustand nur wenige Oe vor dem Umklappprozess bei $B_{ext,0}$ liegt. An der Stelle $\Delta B = B_{ext} - B_{ext,0} \approx 0.5\,\text{Oe}$ sollte der Zustand mit geringerem GMR für eine längere Zeitspanne ($10 - 30\,\text{min}$) erhalten bleiben, um eine Ummagnetisierung aufgrund von Schwankungen auszuschließen. Nun wird ein positiver oder negativer Strom an den unter der GMR-Struktur liegenden Kanal angelegt. Der Umklapprozess der $Ni_{80}Fe_{20}$ Magnetisierung erfolgt für nur eine der beiden Stromrichtungen, wodurch eine Beteiligung thermischer Effekte ausgeschlossen werden kann. Bei $\Delta B \neq 0$ reichen bereits Stromdichten in der Größenordnung von $j \approx 10^4\,\text{A/cm}^2$ aus, um eine Ummagnetisierung herbeizuführen. In allen Versuchen sinkt die Effizienz $\Delta B/j$ mit der Stromdichte. Zudem zeigt $\Delta B/j$ eine starke Temperaturabhängigkeit, bei der $\Delta B/j$ Werte für $T = 1.8\,\text{K}$ und $j \approx 0$ bis zu 20 mal höher sind als bei $T = 4.2\,\text{K}$. Eine solche Temperaturabhängigkeit weist stark darauf hin, dass die Ummagnetisierung nicht durch Biot-Savart Felder hervorgerufen wird. Zudem wurde das durch einen elektrischen Strom generierten Biot-Savart Feld auf vier verschiedene Weisen berechnet. Die hierbei verwendeten Modelle umfassen: einen unendlich langen im Querschnitt rechteckigen Draht, zwei unendlich ausgebreitete Ebenen, ein komplettes Volumen, sowie zwei Ebenen mit geringer Dicke. Bei jedem Modell ist die berechnete Effizienz mindestens drei mal kleiner als die Beobachtung.

Die höchsten in dieser Arbeit gemessenen Effizienzen sind bis zu 10 mal höher als in Ma-

terialsystemen, die aus Schwermetallen und FM bestehen. Im Gegensatz zu anderen Gruppen werden in dieser Arbeit direkte Messmethoden zur Ermittlung von SOT Parametern (wie B_{FL}) verwendet. Die meisten dieser Gruppen verlassen sich auf spin-transfer FMR (ST-FMR) Messungen. Dabei wird ein AC Signal zur Anregung verwendet und zeitgleich die zweite Harmonische als Antwort gemessen. Hieraus werden anhand eines theoretischen Modells SOT Parameter (wie τ_{FL} und τ_{DL}) durch Fits bestimmt. Materialsysteme, die aus TIs und magnetischen Isolatoren (MI) bestehen, weisen dagegen bis zu 10 mal höhere Effizienzen auf [9, 10]. In diesen Fällen zeigt die Magnetisierung der MI aus der Ebene heraus, was sich konzeptionell von planar anisotropische Magnetisierungen unterscheidet, welche in unseren Geometrien vorliegt. Der Vorteil von planar anisotropischen Magnetisierungen ist ihre einfache Realisierbarkeit [11]. Hierbei müssen lediglich elliptische Strukturen lithographisch implementiert werden, während bei Systemen mit senkrechter Magnetisierung eine passende Materialkombination erforscht werden muss [12]. Trotz der Tatsache, dass in unserem Fall nur τ_{FL} zum Umklappen der Magnetisierung m beiträgt, weisen unsere SOT-devices die bis dato höchsten gemessenen Effizienzen in der Klasse von in-der-Ebene magnetisierten Schichtstrukturen aller Materialsysteme auf.

References

[1] R. Desikan, C. R. Lefurgy, S. W. Keckler, D. Burger, *et al.*, *On-chip MRAM as a high-bandwidth, low-latency replacement for DRAM physical memories* (Computer Science Department, University of Texas at Austin, 2002).

[2] X. Dong, X. Wu, G. Sun, Y. Xie, H. Li, and Y. Chen, *Circuit and microarchitecture evaluation of 3d stacking magnetic ram (mram) as a universal memory replacement,* in *2008 45th ACM/IEEE Design Automation Conference* (IEEE, 2008) pp. 554–559.

[3] W. Kim, J. Jeong, Y. Kim, W. Lim, J. Kim, J. Park, H. Shin, Y. Park, K. Kim, S. Park, *et al.*, *Extended scalability of perpendicular stt-mram towards sub-20nm mtj node,* in *2011 International Electron Devices Meeting* (IEEE, 2011) pp. 24–1.

[4] A. Manchon, J. Železnỳ, I. M. Miron, T. Jungwirth, J. Sinova, A. Thiaville, K. Garello, and P. Gambardella, *Current-induced spin-orbit torques in ferromagnetic and antiferromagnetic systems,* Reviews of Modern Physics **91**, 035004 (2019).

[5] X.-L. Qi and S.-C. Zhang, *Topological insulators and superconductors,* Reviews of Modern Physics **83**, 1057 (2011).

[6] J. Zhang, J. P. Velev, X. Dang, and E. Y. Tsymbal, *Band structure and spin texture of bi 2 se 3 3 d ferromagnetic metal interface,* Physical Review B **94**, 014435 (2016).

[7] B. Jönsson-Åkerman, R. Escudero, C. Leighton, S. Kim, I. K. Schuller, and D. Rabson, *Reliability of normal-state current–voltage characteristics as an indicator of tunnel-junction barrier quality,* Applied Physics Letters **77**, 1870 (2000).

[8] P. B. Ndiaye, C. A. Akosa, M. H. Fischer, A. Vaezi, E.-A. Kim, and A. Manchon, *Dirac spin-orbit torques and charge pumping at the surface of topological insulators,* Physical Review B **96**, 014408 (2017).

[9] N. H. D. Khang, Y. Ueda, and P. N. Hai, *A conductive topological insulator with large spin hall effect for ultralow power spin–orbit torque switching,* Nature materials **17**, 808 (2018).

[10] P. Li, J. Kally, S. S.-L. Zhang, T. Pillsbury, J. Ding, G. Csaba, J. Ding, J. Jiang, Y. Liu, R. Sinclair, *et al.*, *Magnetization switching using topological surface states,* Science advances **5**, eaaw3415 (2019).

[11] S. Bhatti, R. Sbiaa, A. Hirohata, H. Ohno, S. Fukami, and S. Piramanayagam, *Spintronics based random access memory: a review,* Materials Today **20**, 530 (2017).

[12] D. Apalkov, B. Dieny, and J. Slaughter, *Magnetoresistive random access memory,* Proceedings of the IEEE **104**, 1796 (2016).

Appendices

A

Recipe for tunnel Barrier Samples

ALD Test Thermopower 3D **02.05.2018**

0 Get info:

- sample thickness
- cap size

1 Cleaving:

- cleave sample in water (petri dish + scaling paper)
- dry with N2
- microscope check (pics + scale)
- check if it fits into chip carrier (max 3x4 mm)
- remove In on the backside
- USB, 37 kHz, 100%, 5 min

I FM deposition

2 Resist:

- spin coating: ARN 4340, 6000 rpm, 20 s
- softbake: 2 min @ 80 °C
- remove edges for smaller mask sample distance
- exposure: 20 s with FM mask
- post-exp. bake: 6 min @ 80 °C
- Development: 38 s in AR 300-47
- check under microscope

3.1 Cleaning (@ RIE)

- 3 s Prog. 70 (miniclean)

IF CAP

3.2 Etching:

- IBE: 400V, -400V, 8mA, 3.5 sccm Ar, rotation at position 2.0
- etch rate: CMT: 0.7 nm/s; MT: 1.4 nm/s
- duration: until cap is removed

END

4 Diffusionbarrier ZrO (@ ALD growth):

	H2O	Precursor
Pulse	0.05	0.2
Saturate	10	10
Purge	100	100
Turbo	0	0

(Begin Process with H2O peak „Standard process“)

- Precursor: Zr
- Cycles: measurement parameter
- Temp: 30 °C
- Massflow: 10 sccm
- Thresh. H20: 0.25 mbar
- Thresh. Prec: 0.25 mbar

5 Sputter FM (@ sputter chamber):

- deposit 10 nm permalloy, 50W, 110 s
- deposit Ru 5 nm, 50 W, 55 s (anti-oxidation layer)

6 Cap on FM (ex situ UHV metallization):

- Ti: 4 nm
- Au: 40 nm

7 Lift off:

- Aceton, 10 min @ 50°
- hose with Aceton
- if not removed use USB (start at small power and frequency)
- rinse in Isopropanol
- put in petri dish with IPA
- check under microscope, if not satisfied repeat

II Mesa structure (dry etch)

8 Resist:

- spin coating: ARN 4340, 6000 rpm, 20 s
- softbake: 2 min @ 80 °C
- remove edges for smaller mask sample distance
- exposure: 20 s with Mesa mask
- post-exp. bake: 6 min @ 80 °C
- Development: 38 s in AR 300-47

9 BaF2 deposition (@ Käseglocke):

- BaF2: 100 nm
- dep. Rate: ~6 kA/s

10 Lift off:

NO WATER

- Acetone
- USB, 3 min, 37 kHz
- Isopropanol
- check under microscope, if lines → repeat Lift off

11 Etching:

- IBE: 400V, -400V, 8mA, 3.5 sccm Ar, rotation at position 2.0
- etch rate: CMT: 0.7 nm/s; MT: 1.4 nm/s
- duration: until (thickness HgTe + cap size + bottom CMT)*1.1 is etched
  check how much was etched, if not through HgTe: stop process and begin new sample

12 Stripping:

- USB in water, 5 min @ 50 °C, 37 kHz
- check under microscope (LEAVE SAMPLE IN WATER)
- USB in Aceton, 5 min @ 50 °C, 37 kHz
- put in IPA then in water

III Contacts

13 Resist:

- spin coating: ARN 4340, 6000 rpm, 20 s
- softbake: 2 min @ 80 °C
- remove edges for smaller mask sample distance
- exposure: 20 s with Contact mask
- post-exp. bake: 6 min @ 80 °C
- Development: 38 s in AR 300-47

14 Etching:

- IBE: 400V, -400V, 8mA, 3.5 sccm Ar, rotation at position 2.0
- etch rate: CMT: 0.7 nm/s; MT: 1.4 nm/s
- duration: until cap layer reaches 5-10 nm above HgTe

15 Ohmics:

- in situ @ Cluster: AuGe: 65 nm
  Au: 65 nm
- ex situ @ UHV: Ti: 6 nm with angle
  Au: till interface top CMT/MT

16 Lift off:

- Aceton
- Hotplate, 10 min @ 50 °C
- hose metal away
- Hotplate, 3 min @ 50 °C
- Isopropanol
- check under microscope
  if not satisfied repeat with USB

17 Cleaning (@RIE):

- 5 s Prog. 70 (for better SiN grip)

IV Insulator and holes in insulator

18 Insulator deposition (PECVD):

- SiN: 50 nm
- Temp: 80 °C
- recipe: MS SiN 50nm

19 Resist:

- spin coating: ARN 4340, 6000 rpm, 20 s
- softbake: 2 min @ 80 °C
- remove edges for smaller mask sample distance
- exposure: 20 s with Insulator holes mask
- post-exp. bake: 6 min @ 80 °C
- Development: 35 s in AR 300-47

20 RIE:

- cleaning: 5 s Prog. 70
- 3x Main: 37 sec Prog. 2
  3 min pump
  27 sec Prog. 70
- remove resist: 10 min Prog. 70

Check height in DEKTAK to get needed Au height for Bridge

V Bridge

21 Resist:

- spin coating: ARN 4340, 6000 rpm, 20 s
- softbake: 2 min @ 80 °C
- remove edges for smaller mask sample distance
- exposure: 20 s with Bridge mask
- post-exp. bake: 6 min @ 80 °C
- Development: 35 s in AR 300-47

22 Etching:

- IBE: 400V, -400V, 8mA, 3.5 sccm Ar, rotation at position 2.0
- etch rate: not relevant as only cleaning
- duration: < 5 s (just to clean surface Au)

23 Metal deposition UHV:

- Ti: 3 nm
- Au: thickness mesa + 50 nm (under angle)

24 Lift off:

- Aceton
- Hotplate, 10 min @ 50 °C
- hose metal away
- Hotplate, 3 min @ 50 °C
- Isopropanol
- check under microscope
  if not satisfied repeat with USB

B

Recipe for SOT-devices

Recipe for SOT-devices

1. Alignement Marks (2 sets → 1 for 204.8µm other for 81.92µm):

- PMMA 950 K 3% deposited at 5000 (1) 40 sec.
- Baking at 80°C for 10 min
- 2.5 kV EBL. WD = 10 mm- field 204.8 µm. 30 µm aperture, 90 µC/cm² dose
- Development 1 min in AR 600.56: IPA (1:1). Rinse IPA
- Miniclean 3 sec
- Ti (5nm)/Au (50 nm)
- Lift-off

2. Pillars (2.5 kV EBL):

- PMMA 950K 3% at 6000 rpm 40 sec
- 10 min baking at 80°C
- open marks, 30 kV, 550 µC/cm²
- Exposure of the ellipses. 90 µC/cm². WD = 7 mm. field 81.92 µm, aperture 10 µm
- Development 1 min in AR 600.56: IPA (1:1). Rinse IPA
- Use two sets of the marks
- miniclean
- IBE
- ALD X cycles (usually 10) of ZrO2
- sputtering NiFe, Cu, CoFe, Ta, Ru
- Lift-off 10 min in warm 50°C acetone, then 5 min 80/50 ultrasonic
- Control in IPA in the optical microscope. Repeat ultrasonic agitation if necessary
- Overnight MIBK at room temperature

3. Mesa:

- PMMA 950K 2% at 5000 rpm 40 sec
- 1 min baking at 80°
- PMMA 950K 3% at 5000 rpm 40 sec
- 10 min baking at 80°C
- open all local marks and three global marks, field of 204.8 µm, 100 µC/cm² dose for 3 kV, Aperture 30 µm, Wd 7mm. Alignment starts from outer marks, then finishes with inner marks. If there is a sacrificial structure – it is good to open also markers in the field, this will be better justification of the field for the central structure.
- Evaporate BaF2 100 nm
- Lift-off in acetone
- BaF2 mask control in optics
- miniclean
- IBE in the cluster +/-400 V for cap removal (mt 1.4nm/s, cmt 0.7nm/s)
- Overnight MIBK

4. Inner Contacts:

- 950 K PMMA 3%. 5000 rpm 40 sec
- 10 min baking at 80°C
- open marks 30 kV
- Developement 1 min
- 2.5 kV e-beam lithography. WD 7 Field 204.8. x389. Dose 90 µC/cm²
- Development 1 min in AR 600.56: IPA (1:1). Rinse IPA
- Miniclean 1 min in ICP
- 3 sec etch in cluster
- AuGe/Au (50nm/50nm)
- Lift-off.
- 2-3 hours in MIBK.

5. Outer Contacts:

- ARN 4340 6000rpm 20 sec
- bake 2 min 80°
- maskless alligner for structure, lens 10x, D = 495 mJ/cm², check virtual, no autofocus
- postbake 6 min
- development 38 sec AR 300-47
- IBE etch if necessary
- AuGe/Au. 50/50

6. Bridges:

- PMMA 950K 3%x 2 times at 5000 (1) rpm for 40 sec, 1 time at 5500 rpm
- 1 min bake 80°
- Last (the 4th) layer PMMA 950 K 4% at 6000 (1) rpm for 40 sec (Total thickness 800 nm.)
- Bake 10 min at 80 °C
- Open windows. 30 kV, 550 µC/cm²
- measure resist thickness (800 nm)
- Posts 90 x 90 nm boxes; dose 3000 µC/cm² for 30 kV. A = 10 µm, step 2.5 nm. Written in the field 81.92 µm
- Spans 4.7-5 kV, A = 20 µm, 600 µC/cm² (width 100 nm)
- pillars and bridges require good allignement, therefore smaller field (81.92 µm) is used
- Development 4 min with 3sec US agitation at end of each minute
- cross-linked supports. 250 loops x120 µC/cm².
- Miniclean
- Check the change of the thickness after miniclean. It should be 25-40 nm.
- Repeat miniclean if necessary.
- Evaporation 10 nm Ti, 420 nm Au
- Lift-off (30 min warm Aceton)
- IPA clean
- N2 carefully from the side in order to avoid breaking of bridges

Acknowledgements

As this thesis comes to an end I am delighted to take the opportunity to thank everyone who was involved in the process. First I want to express my gratitude to **Prof. Laurens W. Molenkamp** as the head of EP3. Due to his expertise and commitment to his chair he created an environment of world class labs for top scientists. Thank you for giving me the opportunity to learn from the best.

In that sense I also want to thank **Prof. Charles Gould** as my *Doktorvater*. Whenever I faced problems with setups, measurements, signal noise, grounding, instruments, lectures, ..., you always helped me out and explained the problem in the most simplified way possible. I am also thankfull for your entertaining stories about US policy and other interesting facts at universities. Thank you for being my mentor and teacher.

This thesis consists of a great portion of cleanroom work including process developement and execution. This became extraordinary pleasant due to **Dr. Tanja Borzenko**. Especially in the last years of my work you performed the electron beam lithography steps for me which made it possible to conduct the main experiments of my thesis. Besides you were always open for conversations about lithography and family. Thank you for your time and patience as a supervisor.

Every recipe in lithography contains dozens of single steps. In order to succeed in building a working device it is necessary to know the meaning of each of those process steps. This is greatly supervised by **Dr. Johannes Kleinlein**. Whenever I faced issues or needed adjustment concerning my process he offered his time to help me. Therefore thank you for your guidance and help.

Being at the topic of cleanroom work I would like to praise **Volkmar Hock** for his maintaining and entertaining skills. His presence made the yellow room brighter and safer.

Furthermore I would like to thank all my collegues for their help and good vibes. Many thanks to **Martin Baußenwein** who discussed a lot of measurement related questions and gave good advice on games. I am also grateful for the conversations with **David Mahler**, **Lukas Luncer** and **Simon Hartinger**. Special thanks to **Graciely Santos** for her kindness and frankness, it is always a pleasure to talk to you. Moreover I thank **Kajetan Fijalkowski** and **Pankaj Mandal** for some rare but great moments. Keep up the great work and never change. In particular I want to thank my collegues who shared the same office with me. **Martin Winnerlein**, **Boby Chrisol Joseph** and **Alwyn Antony** you guys made that room a better place. It was always funny and entertaining with you.

Finally I would like to thank my whole family for their support. Спасибо, Мама, ты бы

мной гордилась. Папа, спасибо за твою постоянную заботу обо мне. Твоя помощь неоценима. Спасибо Инне и Оксане, моим любимым сестрам за приятные встречи. Спасибо Эвальду и Марии, которые сотворили для меня прекрасную жену. Many thanks to my brothers in law **Jakob**, **Martin**, **Sergej** and **Oleg** for your heartiness. I also want to thank my niece **Jana** and my nephews **Andreas** and **Daniel** for many happy moments. And most importantly thousand thanks to my lovely wife **Emma** for your endurance. You are my pillar of strength and safe haven.